

NAVAL POSTGRADUATE SCHOOL

Monterey, California



DISSERTATION

INTERACTION OF LASER BEAMS WITH RELATIVISTIC ELECTRONS

by

Douglas W. Small

March 1997

Dissertation Supervisor: William B. Colson

Approved for public release; distribution is unlimited.

DTIC QUALITY INSPECTED 3

19980223 123

REPORT DOCUMENTATION PAGE			Form Approved OMB No. 0704-0188	
<small>Public reporting burden for this collection of information is estimated to average 1 hour per response, including the time for reviewing instructions, searching existing data sources, gathering and maintaining the data needed, and completing and reviewing the collection of information. Send comments regarding this burden estimate or any other aspect of this collection of information, including suggestions for reducing this burden, to Washington Headquarters Services, Directorate for Information Operations and Reports, 1215 Jefferson Davis Highway, Suite 1204, Arlington, VA 22202-4302, and to the Office of Management and Budget, Paperwork Reduction Project (0704-0188), Washington, DC 20503.</small>				
1. AGENCY USE ONLY (Leave blank)		2. REPORT DATE March 1997	3. REPORT TYPE AND DATES COVERED Doctoral Dissertation	
4. TITLE AND SUBTITLE INTERACTION OF LASER BEAMS WITH RELATIVISTIC ELECTRONS			5. FUNDING NUMBERS	
6. AUTHOR(S) Small, Douglas W.				
7. PERFORMING ORGANIZATION NAME(S) AND ADDRESS(ES) Naval Postgraduate School Monterey, CA 93943-5000			8. PERFORMING ORGANIZATION REPORT NUMBER	
9. SPONSORING/MONITORING AGENCY NAME(S) AND ADDRESS(ES)			10. SPONSORING/MONITORING AGENCY REPORT NUMBER	
11. SUPPLEMENTARY NOTES The views expressed in this thesis are those of the author and do not reflect the official policy or position of the Department of Defense or the U.S. Government.				
12a. DISTRIBUTION/AVAILABILITY STATEMENT Approved for public release; distribution is unlimited.			12b. DISTRIBUTION CODE	
13. ABSTRACT (Maximum 200 words) Motivated by the desire to put a free electron laser (FEL) weapon on a ship, the FEL and the related process of Compton backscattering are studied. The theme of the majority of this work is the interaction of the Gaussian optical mode with a beam of relativistic electrons. Classical FEL theory is reviewed in Chapter II. Simulations based on the classical theory are used in Chapter III to study a proposed 1 kW (kilowatt) infrared FEL. In Chapter IV, simulation is used to study the problem of electron beam/optical mode overlap in an ultraviolet (UV) FEL. A new concept, the FEL with a short Rayleigh length, is studied in Chapter V. The idea is tested on the UV FEL, then used to design and simulate a megawatt-class FEL for ship self-defense. An analytical calculation of the Compton backscattering of laser light is performed in Chapter VI. A quantum electrodynamics (QED) formalism is used to find the spectrum and angular distribution of photons scattered out of a Gaussian optical mode by relativistic electrons.				
14. SUBJECT TERMS free electron laser, FEL, simulation, Compton backscattering			15. NUMBER OF PAGES 113	
			16. PRICE CODE	
17. SECURITY CLASSIFICATION OF REPORT UNCLASSIFIED	18. SECURITY CLASSIFICATION OF THIS PAGE UNCLASSIFIED	19. SECURITY CLASSIFICATION OF ABSTRACT UNCLASSIFIED	20. LIMITATION OF ABSTRACT UL	

Approved for public release; distribution is unlimited.

INTERACTION OF LASER BEAMS WITH RELATIVISTIC ELECTRONS

Douglas W. Small
Lieutenant, United States Navy
B.S., Marquette University, 1988

Submitted in partial fulfillment of the
requirements for the degree of

DOCTOR OF PHILOSOPHY IN PHYSICS

from the

NAVAL POSTGRADUATE SCHOOL

March 1997

Author: _____

Douglas W. Small

Douglas W. Small

Approved by: _____

William B. Colson

William B. Colson
Professor of Physics
Dissertation Supervisor

Robert L. Armstead

Robert L. Armstead
Professor of Physics

Karl Heinz E. Woehler

Karl Heinz E. Woehler
Professor of Physics

James H. Luscombe

James H. Luscombe
Professor of Physics

Ron J. Pieper

Ron J. Pieper
Professor of Electrical Engineering

Approved by: _____

Anthony A. Atchey
Anthony A. Atchey, Chair, Department of Physics

Approved by: _____

Maurice D. Weir
Maurice D. Weir, Associate Provost for Instruction

ABSTRACT

Motivated by the desire to put a free electron laser (FEL) weapon on a ship, the FEL and the related process of Compton backscattering are studied. The theme of the majority of this work is the interaction of the Gaussian optical mode with a beam of relativistic electrons.

Classical FEL theory is reviewed in Chapter II. Simulations based on the classical theory are used in Chapter III to study a proposed 1 kW (kilowatt) infrared FEL. In Chapter IV, simulation is used to study the problem of electron beam/optical mode overlap in an ultraviolet (UV) FEL. A new concept, the FEL with a short Rayleigh length, is studied in Chapter V. The idea is tested on the UV FEL, then used to design and simulate a megawatt-class FEL for ship self-defense.

An analytical calculation of the Compton backscattering of laser light is performed in Chapter VI. A quantum electrodynamics (QED) formalism is used to find the spectrum and angular distribution of photons scattered out of a Gaussian optical mode by relativistic electrons.

TABLE OF CONTENTS

I.	INTRODUCTION	1
II.	CLASSICAL FREE ELECTRON LASER THEORY	5
	A. THE FREE ELECTRON LASER	5
	B. THE RESONANCE CONDITION	6
	C. ELECTRON DYNAMICS	10
	1. Electron Trajectories in the Undulator	10
	2. Electron Beam Quality and Emittance	14
	3. The Pendulum Equation	16
	D. THE FEL OPTICAL WAVE EQUATION	18
	E. GAIN	22
	1. The Low Gain FEL	24
	2. The High Gain FEL	29
	3. Gain Degradation Due to Electron Beam Quality	31
	F. SHORT PULSES	34
	G. FEL WITH GAUSSIAN OPTICAL MODE	35
III.	SIMULATIONS OF FIREFLY 1KW FEL	39
	A. BACKGROUND	39
	B. SIMULATIONS AND RESULTS	39
	C. CONCLUSIONS	48
IV.	TRANSVERSE EFFECTS IN UV FREE ELECTRON LASERS	49
	A. BACKGROUND	49
	B. TRANSVERSE MULTIMODE SIMULATIONS	50
	C. OPTICAL MODE SIZE EFFECT ON FEL GAIN	53

D. ELECTRON BEAM SIZE EFFECT ON FEL GAIN	56
E. CONCLUSIONS	58
V. FELS WITH SHORT RAYLEIGH LENGTH	61
A. MOTIVATION	61
B. UVFEL WITH SHORT RAYLEIGH LENGTH	62
1. Single Pass Gain	63
2. Steady State Gain	69
C. MW-CLASS FEL WITH SHORT RAYLEIGH LENGTH	71
1. MW-Class FEL Design	71
2. Simulations of the MW-Class FEL	73
D. CONCLUSIONS	76
VI. COMPTON BACKSCATTERING OF LASER LIGHT	79
A. PRELIMINARIES	79
B. VECTOR POTENTIAL FOR LASER LIGHT	81
C. DIRAC WAVEFUNCTIONS	83
D. PHOTON EMISSION	88
E. CONCLUSIONS	98
LIST OF REFERENCES	99
INITIAL DISTRIBUTION LIST	101

ACKNOWLEDGEMENT

The author wishes to acknowledge the support of this research by the Naval Postgraduate School, the High Energy Laser office at the Space and Naval Warfare Command (SPAWAR), and Thomas Jefferson National Accelerator Facility.

I want to thank the dissertation committee for their guidance in making this dissertation better and more self-contained, and especially for pointing out the places where I needed to find out what I was talking about. Special thanks are due Professor Bill Colson. He filled my brain with as much physics as it could hold, and then guided me in writing some of it down. He was continuously available for discussions on everything from electrodynamics to politics to camping.

I want to thank my wife, Donna, who prepared our family for our move to Virginia by herself so that I could finish this dissertation and graduate. She also proof-read each chapter, providing great advice on making them more readable. I could not have done this without her. I also want to thank my dad for teaching me to work hard and to do everything the right way. I hope he sees that in this work.

I. INTRODUCTION

Today's US Navy is the most powerful the world has ever known. It can position aircraft, ships, and submarines within striking distance and project its power deep within the borders of almost any country. Yet today's ships are arguably more vulnerable to attack from mines and anti-ship cruise missiles (ASCMs) than ever before, as a result of the Navy's shift from blue to brown water. Ship defense against ASCMs is mainly a problem of reaction time; that is, there is not much time (usually seconds, depending on the missile's speed and the ship's detection range) between detection of the missile and impact of the missile with the ship. In this case a self-defense weapon which travels at the speed of light would be most useful. With continuing improvements in ASCM speed, stealth, and maneuverability, the problem gets even more difficult for existing defenses. A directed energy weapon (DEW) could be the solution.

Experiments in missile destruction and atmospheric propagation have shown that a megawatt (MW) class free electron laser (FEL) is the directed energy weapon of choice for ship self defense (SSD). Megawatts are needed in order to deposit the required energy on the target in a short amount of time. More power probably would not shorten this time because thermal blooming, which results from atmospheric absorption, will degrade propagation. The FEL is needed because of its inherent tunability and designability, characteristics no other laser system can boast. The laser weapon's wavelength must operate in very narrow atmospheric absorption windows in order to propagate the beam to the target, avoiding problems like thermal blooming. The FEL has another advantage over other laser systems in that its gain medium is a vacuum.

While SSD is seen as the mission area where laser weapons can get their start, a MW-class FEL aboard a ship could be an awesome offensive weapon as well. It was demonstrated in the 1970s that it is easier for the laser weapon to destroy

crossing targets than incoming targets. It is possible that the precision and power of the FEL could also be used against aircraft and their pilots, satellites, ballistic missiles, other ships, and even personnel. Unlike the proposed Arsenal Ship, which merely packs a ship with more missiles, a shipboard directed energy weapon would truly bring about a revolution in military affairs, which would hasten the obsolescence of the missile. In this work we study the FEL and related phenomena, contributing to a field of scientific research with the goal of putting a DEW on a ship.

Several topics are presented on the interaction of laser beams with relativistic electrons; this includes the free electron laser. In the next chapter, an overview of classical FEL theory necessary for understanding the ensuing chapters is provided. We describe the components of the FEL and then find the emission wavelength using basic physical arguments. Using the Lorentz force and Maxwell's equations, we derive a set of two equations called the FEL pendulum and wave equations which describe the FEL interaction. Using these equations, we find expressions and describe the mechanisms for FEL gain. Modifications of the FEL interaction due to short optical pulses or the Gaussian optical mode are considered in the last two sections of the chapter.

Original work simulating a proposed one kilowatt (1kW) upgrade to the FIREFLY FEL at Stanford University is presented in Chapter III. This upgrade would represent a one hundred-fold increase in FEL average power over that which currently exists. This work was originally presented at the 16th International FEL Conference and published as "Simulations of the Stanford FIREFLY 1kW free electron laser" in Nuclear Instruments and Methods in Physics Research (NIM) A 358, ABS 44, (1995).

In Chapter IV is presented original research concerning optical mode transverse effects in ultraviolet free electron lasers (UVFEL). Specifically, it is the UVFEL proposed by the Laser Processing Consortium (LPC), a group based at the Thomas Jefferson National Accelerator Facility (TJNAF), that is simulated. The results were presented at the 17th International FEL Conference and published as

"Transverse effects in UV FELs" in NIM A **375**, ABS 61, (1996).

New and original work on a new concept in FEL design, the short Rayleigh length FEL, is presented in Chapter V. The concept is first tested on the LPC UVFEL. Those results were presented at the 18th International FEL Conference and will be published in 1997. We then use this concept to design and simulate a MW-class FEL oscillator suitable for ship self-defense. This design and the simulation results were presented at a workshop at TJNAF entitled "Navy MW-Class SSD FEL Concepts" which was sponsored by the Navy High Energy Laser office at the Space and Naval Warfare Command (SPAWAR).

In Chapter VI we present new and original calculations of Compton backscattering of laser light from electrons. This process has been proposed as a means of generating x-rays for many applications, including medical imaging, and γ -rays for a so-called γ - γ collider. Our calculations are the first attempt to incorporate the finite size of the laser beam into the usual scattering problem.

II. CLASSICAL FREE ELECTRON LASER THEORY

A. THE FREE ELECTRON LASER

The Free Electron Laser is a device which transforms the kinetic energy of a beam of relativistic electrons into coherent radiation (Ref. 1). A transverse, static magnetic field causes the electrons to wiggle and thereby radiate electromagnetic energy (Ref. 1). The radiation can either be stored in an optical cavity and amplified over many passes, as in the FEL oscillator, or amplified in a single pass, as in the FEL amplifier (Ref. 1). In this work, we will be concerned only with the oscillator configuration.

The major components of the FEL oscillator are the electron accelerator, undulator, and optics. The accelerator delivers a beam of relativistic electrons to the FEL with energies anywhere from a few MeV to GeV depending on the wavelength of laser light desired. There are many different types of accelerators suitable for use in an FEL, but we will only be concerned with the radio-frequency linear accelerator (RF LINAC). The RF LINAC accelerates pulses of electrons, called micropulses, using either standing or travelling waves of an electromagnetic field (Ref. 2). One micropulse can be accelerated within each wavelength of the RF field, called a "bucket." For example, if the frequency of the RF radiation is $f = 500$ MHz, buckets are separated by a distance $c/f = 60$ cm. Electron micropulses are created and inserted into the accelerator by the injector (or electron gun). In our example, if the injector also operated at 500 MHz, it would fill every RF bucket and micropulses would be separated by 60 cm. The current in the micropulse is called the peak current I , and the average current is calculated using the duty factor (the ratio of the micropulse length to the distance between buckets). If we take $I = 500$ A and a micropulse length $l_p = 0.6$ mm ($l_p/c = 2$ ps), then the duty factor in our example accelerator is 0.001. The average current is then $\bar{I} = 500 \times 0.001$ A = 0.5 A.

The undulator is a set of permanent magnets or electromagnets arranged to provide a periodic, transverse, magnetic field of wavelength λ_0 along which the electrons traverse. The polarization of the undulator's magnetic field can be either helical or linear. The world's first FEL used a helical undulator, but the linear undulator is more common now (Ref. 3). Undulators can range in length from 1m to 25m.

The mirrors of the optical cavity (in the oscillator) store the light which is then amplified over successive passes of the electrons through the undulator. Total optical cavity losses, including the outcoupled light, are quantified by the quality factor Q , so that losses per round trip of the optical pulse are $(100/Q)\%$ (Ref. 3). The optical cavity is generally centered on and several times longer than the undulator.

B. THE RESONANCE CONDITION

With a basic knowledge of the physics of the FEL interaction we can define some important parameters and find the wavelength of the emitted radiation.

Depicted in Figure 1 is the FEL interaction: the interaction of relativistic electrons with the undulator magnetic field, \vec{B}_u , and the radiated electric, \vec{E}_r , and magnetic, \vec{B}_r , fields. At the top is a schematic of an FEL showing the electron beam path through the undulator, the orientation of the undulator magnets, and the mirrors. The middle sketch is a blow-up of one wavelength λ_0 of the undulator. The undulator magnetic field \vec{B}_u oscillates in the yz-plane, causing the electrons to wiggle in the xz-plane. At the bottom of the figure is a blow-up of one half of one wavelength λ of the radiation field. A portion of the electron trajectory is drawn at an angle to the z-axis. It is the transverse component of the electron velocity, that which projects on the xy-plane, which couples to the radiation electric field, allowing energy to be transferred between them.

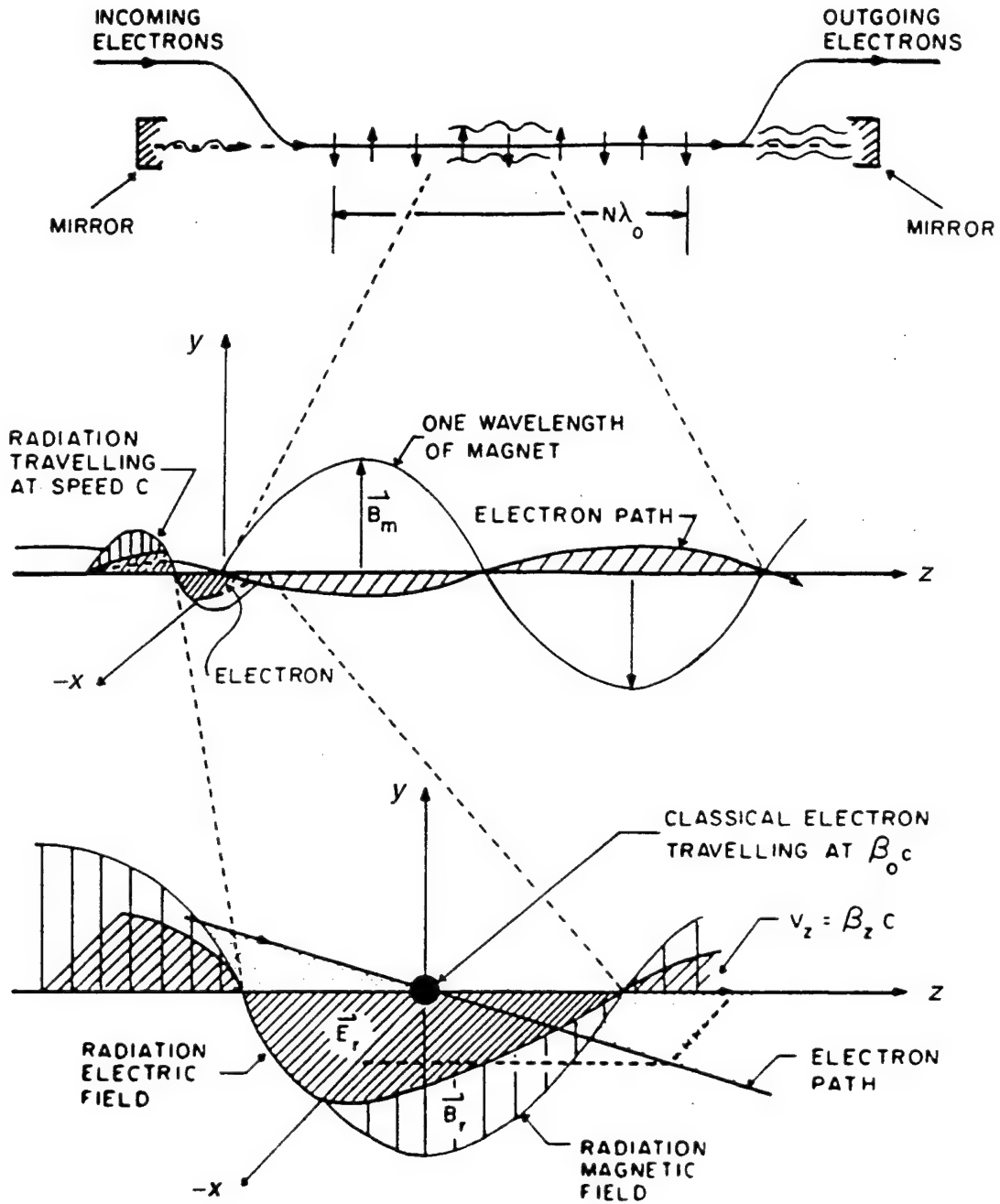


Figure 1. Relativistic electrons interacting with an undulator magnetic field, B_u , and radiated electric, E_r , and magnetic, B_r , fields (after Ref. 4).

In order for the radiation in the oscillator cavity to grow, the electrons must lose energy to the light wave on each pass through the undulator. The Lorentz force shows that this energy loss is $d\gamma/dt \propto \vec{\beta} \cdot \vec{E}_r$ where $\vec{\beta} = \vec{v}/c$, \vec{v} is the particle velocity and the relativistic factor $\gamma = (1 - \vec{\beta}^2)^{-1/2}$ (Ref. 5). Since \vec{E}_r is transverse, that is, in a plane perpendicular to the z-axis, only a transverse component of $\vec{\beta}$ couples to the cavity radiation. Driven by the undulator magnetic field, that transverse component is of the form $\beta_{\perp} \propto \text{Re}(Ke^{ik_0 z})$ where K is a constant called the "undulator parameter," $k_0 = 2\pi/\lambda_0$, and λ_0 is the undulator wavelength. The electric field is of the form $E_r \propto \text{Re}(E_0 e^{i(kz - \omega t + \phi)})$ where $k = 2\pi/\lambda$, λ is the radiation wavelength, $\omega = kc$, and ϕ is an optical phase factor. Therefore, we find that $d\gamma/dt \propto \text{Re}(KE_0 e^{i[(k+k_0)z - \omega t]} e^{i\phi})$. It is evident from these preliminary considerations that the electron "ponderomotive" phase defined as

$$\zeta = (k + k_0)z - \omega t \quad (1)$$

is fundamental to the FEL interaction. For relativistic FELs, this phase represents the position of the electron within a radiation wavelength.

The time it takes the electrons to traverse the undulator is $L/c\beta_z \approx 10^{-8}$. Rather than work with time scales on the order of 10^{-8} seconds, we introduce a dimensionless time τ , defined as

$$\tau = \frac{c\beta_z t}{L} \approx \frac{ct}{L} \quad (2)$$

where L is the undulator length and $c\beta_z = v_z \approx c$ in the relativistic limit. As the electrons traverse the undulator τ ranges from 0 to 1. We can now define the electron phase velocity as

$$v(\tau) = \frac{d\zeta(\tau)}{d\tau} = L[(k + k_0)\beta_z - k] \quad (3)$$

The phase velocity measures the rate of change of the electron's phase relationship (ζ) to the optical field.

In order that the rate of transfer of energy from the electrons to the radiation field is maximized, the wiggling electron and the electric field must be nearly resonant. Looking at Figure 1, we can explain this as follows: when the electric field is pointed in the x-direction, the electron trajectory needs to have a component in the x-direction. When the electric field phase increases by π and is pointed in the (-x)-direction, the electron trajectory must also have a component in the (-x)-direction. This will be the case if exactly one wavelength of light passes over the electron every time the electron traverses exactly one wavelength of the undulator. This is the "resonance condition." If one wavelength of light passes over the electron for every undulator period the electron traverses, the electron will maintain the same phase relationship with the light. Resonance thus implies that the phase velocity $v(\tau)$, must be zero.

Invoking the resonance condition, we set $v(\tau) = 0$ in (3) and solve for λ with the result $\lambda = \lambda_0(1 - \beta_z)/\beta_z$. From the definition of γ , we find $\gamma^{-2} = 1 - \beta_z^2 - \beta_\perp^2$. In the helical undulator (as determined later), $\beta_\perp^2 = K^2/\gamma^2$. Solving for β_z we get

$$\beta_z = 1 - \frac{1 + K^2}{2\gamma^2} + \dots \quad (4)$$

for $\gamma \gg 1$. Substituting (4) into the expression for λ above we find

$$\lambda = \lambda_0 \frac{1 + K^2}{2\gamma^2} \quad (5)$$

which is the wavelength of light emitted by the electrons in the FEL. This expression shows that we can change the wavelength by changing the electron beam energy γmc^2 or the undulator characteristics λ_0 or K .

In the preceeding discussion we defined and then discussed resonance for a single electron. In a real electron beam, there are about 10^{10} electrons in the micropulse; all of them could not possibly be exactly resonant. Although we define resonance as $v = \dot{\xi} = 0$, where $(\dot{})$ represents differentiation with respect to τ , we will find that in the low gain FEL (section E) it is desirable to operate at just above resonance $v(0) \approx v_0 = 2.6$. We can understand this by considering that about 10^6

electrons are uniformly spread over the length of an optical wavelength. If they are resonant, they maintain the same phase relationship with the light throughout the interaction even though the light is passing over them. Thus at resonance the radiation from the i^{th} electron at ζ_i will exactly cancel that from an electron at a phase $(\zeta_i - \pi)$. This cancellation will occur for each electron. To avoid this cancellation, for net radiation, the electrons must radiate together, or "bunch" on the scale of the optical wavelength. This requires that $\dot{\zeta} > 0$ and $\ddot{\zeta} > 0$. We will discuss this microscopic bunching in part three of the next section.

C. ELECTRON DYNAMICS

Electrons in the undulator interact with both the undulator field and the radiation field which has been set up in the cavity. In subsection 1, we find the electron trajectories in the undulator using the Lorentz force equation of motion. We then use these trajectories in the second subsection to deduce measures of electron beam quality. In the third subsection we assume that electron radiation has set up a classical radiation field in the optical cavity and then allow it to interact with the electrons. This will result in the pendulum equation, which describes bunching.

1. Electron Trajectories in the Undulator

A linear undulator polarized in the y-direction causes electrons to wiggle in the xz-plane. In addition, since electron beams have a small radius and angular spread (which depends on the quality of the beam from the accelerator), electrons off axis in the y-direction are in stronger fields and are therefore focussed back toward the axis. This results in so-called betatron oscillations.

The magnetic field of a linear undulator with no external focussing in the x-direction is given by

$$\vec{B} = [B_x, B_y, B_z] = B_0[0, \sin(k_0 z)\cosh(k_0 y), \cos(k_0 z)\sinh(k_0 y)] \quad (6)$$

where B_0 is the amplitude of the undulator field (Ref. 3). Consider an idealized electron which is injected into the undulator perfectly (i.e., $x(0) = \beta_x(0) = 0$) in the x -direction. The electron motion is governed by the relativistic Lorentz force equation of motion in the undulator field (Ref. 5):

$$\frac{d\vec{p}}{dt} = -e\vec{\beta} \times \vec{B} \quad (7)$$

where $e = |e|$ is the magnitude of the electron charge, and the electron's momentum is $\vec{p} = \gamma mc\vec{\beta}$, m is the electron mass, and c is the speed of light in vacuum. Note that cgs units are used. Substituting (6) into (7), noting that $d\gamma/dt = 0$ since the magnetic field can do no work on the electron, we get the set of equations

$$\dot{\beta}_x = \frac{eB_0}{\gamma mc} [\beta_z \sin(k_0 z(t)) \cosh(k_0 y(t)) - \beta_y \cos(k_0 z(t)) \sinh(k_0 y(t))] \quad (8a)$$

$$\dot{\beta}_y = \frac{eB_0}{\gamma mc} \beta_x \cos(k_0 z(t)) \sinh(k_0 y(t)) \quad (8b)$$

$$\dot{\beta}_z = -\frac{eB_0}{\gamma mc} \beta_x \sin(k_0 z(t)) \cosh(k_0 y(t)) \quad (8c)$$

where $(\dot{}) \equiv d/dt$. The right side of (8a) is an exact time derivative and can be integrated immediately with the result:

$$\beta_x = -\frac{\sqrt{2}K}{\gamma} \cos(k_0 z) \cosh(k_0 y) \quad (9a)$$

where $K = eB_0\lambda_0/2\pi mc^2$ and $\bar{B} = B_0/\sqrt{2}$ is the root-mean-square (rms) magnetic field strength. The dimensionless parameter K is the undulator parameter and is an important quantity in FEL physics, as shown in (5). The constant of integration has been set to zero indicating our assumption of perfect injection in this direction. The time dependence of the dynamical variables has been suppressed for brevity. Substituting (9a) into (8b) and (8c) we get

$$\dot{\beta}_y = -\frac{cK^2 k_0}{\gamma^2} \cos^2(k_0 z) \sinh(2k_0 y) \quad (9b)$$

$$\dot{\beta}_z = \frac{cK^2k_0}{\gamma^2} \sin(2k_0z) \cosh^2(k_0y) \quad . \quad (9c)$$

Equations (9) are coupled, nonlinear and too difficult to solve analytically. In order to investigate the xz-plane motion we will now add the restriction of perfect injection in the y-direction also. That leaves us with

$$\beta_x = -\frac{\sqrt{2}K}{\gamma} \cos(k_0z) \quad (10a)$$

$$\dot{\beta}_y(0) = y(0) = 0 \quad (10b)$$

$$\dot{\beta}_z = \frac{cK^2k_0}{\gamma^2} \sin(2k_0z) \quad . \quad (10c)$$

Now in the FEL, $K \approx 1$ and $\gamma \gg 1$, so that $K/\gamma \ll 1$ (Ref. 3). This allows us to expand equations (10) for the trajectories, keeping only terms to order $(K/\gamma)^2$. To zeroth order in (K/γ) , $z(t) = c\bar{\beta}_z t$ where $c\bar{\beta}_z$ we take to be the average electron velocity in an undulator period. Using (4), we find $c\bar{\beta}_z = c(1 - (1+K^2)/2\gamma^2 + \dots) \approx c$. Substituting $z(t) = c\bar{\beta}_z t$ into (10c) to find the next higher order contribution we get

$$z(t) = c\bar{\beta}_z t - \frac{K^2}{4k_0\gamma^2} \sin(2k_0c\bar{\beta}_z t) + \dots \quad (11)$$

which is already to order $(K/\gamma)^2$. To find $x(t)$, we will substitute the first term of (11) into (10a) since using the second would lead to higher order terms in $x(t)$. We get

$$x(t) = -\frac{\sqrt{2}K}{k_0\gamma} \sin(k_0c\bar{\beta}_z t) + \dots \quad (12)$$

where in both (11) and (12) we have set $\bar{\beta}_z = 1$ in the denominator.

We can rewrite (11) and (12) in terms of the dimensionless time τ (see (2)) as

$$x(\tau) = -\frac{K\lambda_0}{\sqrt{2}\pi\gamma} \sin(2\pi N\tau) + \dots \quad (13a)$$

$$z(\tau) = \bar{\beta}_z L \tau - \frac{K^2\lambda_0}{8\pi\gamma^2} \sin(4\pi N\tau) + \dots \quad (13b)$$

where $N = L/\lambda_0$ is the number of undulator periods. As expected, the x-component of the trajectory is the wiggling motion caused by the undulator with one oscillation per undulator period. The z-component contains the average velocity term and a term with a fast oscillation (twice per undulator period). The oscillation is superimposed on the average motion because as an electron with constant speed makes an excursion to the side, the z-component of its velocity must slow, leading to an oscillation in z-trajectory. An electron makes this excursion twice per linear undulator period, which causes the z-trajectory to oscillate twice per undulator period.

Now that we have found the trajectories in the x- and z-directions (13), we will find the motion in the y-direction. The y-trajectories are called betatron oscillations and are caused by the focussing action of the undulator magnetic field. We need to use a more realistic beam in this direction, but maintain a small enough beam such that $k_0 y \ll 1$ and $\sinh(2k_0 y) \approx 2k_0 y$. If we then re-write (9b) in terms of τ , the result is

$$\ddot{y}(\tau) = -\frac{2K^2 L^2 k_0^2}{\gamma^2} \cos^2(2\pi N \tau) y(\tau) \quad (14)$$

Since a typical betatron oscillation takes several undulator periods to complete, we can average (14) over several periods (Ref. 3). We are then left with

$$\ddot{y}(\tau) = -\frac{K^2 L^2 k_0^2}{\gamma^2} y(\tau) = -\frac{\partial V_\beta(y)}{\partial y} \quad (15)$$

which is the equation of motion for a simple harmonic oscillator. The solution, and thus the y-trajectory, is sinusoidal. The harmonic potential is $V_\beta(y) = \omega_\beta^2 y^2 / 2$ where $\omega_\beta = KLk_0/\gamma = 2\pi NK/\gamma$ is the dimensionless betatron frequency. In a typical undulator $N = 100$, $K = 1$, $\gamma = 100$, and we get $\omega_\beta = 2\pi$, or one betatron oscillation along the undulator.

We have only treated betatron motion in one direction, but there can be betatron focussing in the other direction as well. This could be provided by external focussing magnets, or by machining parabolic pole-faces on the undulator magnets

(Ref. 3). Neither the amount of focussing nor the electron beam quality have to be the same in both directions.

2. Electron Beam Quality and Emittance

By inspection of (15) and knowledge of Hamiltonian mechanics, we know the harmonic betatron oscillations have a constant of motion $H_\beta = [\omega_\beta y^2(\tau) + \dot{y}^2(\tau)]/2 = [\omega_\beta y^2(0) + \dot{y}^2(0)]/2$. It can also be shown that when an electron is injected off axis ($y(0) = y_0$) or with an initial angle ($\dot{y}(0) = L\theta_y$ where θ_y is the angle from the z-axis), its z-velocity is decreased by $\Delta\beta_z = -H_\beta/L^2$ relative to a perfectly injected electron (Ref. 3). Taking differentials of (3) we find $\Delta v \approx Lk\Delta\beta_z$ since $k \gg k_0$. Therefore, an imperfectly injected electron experiences a decrease in phase velocity given by

$$\Delta v \approx -\frac{kH_\beta}{L} = -\frac{2\pi N}{1 + K^2} (K^2 k_0^2 y_0^2 + \gamma^2 \theta_y^2) \quad (16)$$

where we have used (5).

In a real electron beam from an RF LINAC there can be $\approx 10^{10}$ electrons per micropulse, each of which has a phase velocity change away from the average given by (16). Numerically we don't simulate all 10^{10} electrons, but instead distribute many electrons in both injection position and angle. They are distributed as a Gaussian, which has the distribution function

$$f(q) = \frac{\exp(-q^2/2\sigma^2)}{\sqrt{2\pi} \sigma} \quad (17)$$

where σ is the standard deviation and q is the variable being distributed (Ref. 3). Using (16) as a guide we define the standard deviation of the angular distribution as

$$\sigma_\theta = \frac{2\pi N \gamma^2 \bar{\theta}^2}{1 + K^2} \quad (18)$$

where $\bar{\theta}$ is the root mean square (rms) initial angle from the z-axis. The standard

deviation of the position distribution, also called the dimensionless electron beam radius, is

$$\sigma_e = \sqrt{\frac{\pi}{\lambda L}} \tau_0 \quad (19)$$

where τ_0 is the rms initial distance from the z-axis (Ref. 3). The significance of the factor $\sqrt{\lambda L/\pi}$, the characteristic optical mode size, will be discussed in section G of this chapter. From (16) we see that

$$\sigma_{ve} = \frac{2\pi N K^2 k_0^2 \tau_0^2}{1 + K^2} \quad (20)$$

is the standard deviation of an exponential spread in phase velocity caused by the initial Gaussian spread in position characterized by (19). The Gaussian spread in injection angles characterized by (18) also leads to an exponential distribution in phase velocity with the same standard deviation (Ref. 3). The exponential distribution arises because the phase velocity of an electron decreases no matter what the direction of the (Gaussian distributed) initial position or angle. The distribution function for the exponential is given by

$$f(q) = \frac{\exp(q/\sigma)}{\sigma}; \quad q \leq 0 \quad (21)$$

where q is the variable being distributed, i.e., v_i , the phase velocity of the i^{th} electron (Ref. 3).

The injection angles and positions of the electrons in the beam are governed by a quantity called the "emittance," which is a measure of the quality of the electron beam. The rms emittance is defined as $\epsilon_{rms} = \pi \tau_0 \bar{\theta}$, and is a fixed quantity throughout the entire length of the undulator (Ref. 2). That is, one cannot change the radius of the electron beam without affecting its angular spread and vice versa. Solving (18) and (19) for $\bar{\theta}$ and τ_0 and substituting these into the definition of emittance yields

$$\epsilon_{rms} = \sqrt{\pi} \lambda \epsilon \quad (22)$$

where we have defined the dimensionless emittance ε as

$$\varepsilon = \sigma_e \sqrt{\sigma_\theta} \quad . \quad (23)$$

This dimensionless emittance will be used extensively in Chapters IV and V.

3. The Pendulum Equation

We now consider the interaction of the electrons with both the undulator and radiation fields. We have already found the macroscopic electron trajectories in the undulator. Our goal in this subsection is to find an expression which describes the evolution of bunching. We will use the field of a helical undulator in this section as it makes the problem mathematically easier. At the end we will state a prescription for transforming the pendulum equation to that for a linear undulator.

The magnetic field on the axis of a helical undulator is given by

$$\vec{B}_u = B_0[\cos(k_0 z), \sin(k_0 z), 0] \quad (24)$$

and the radiation field present in the cavity can be represented by

$$\vec{E}_r = E(x, y, z, t)[\cos\psi, -\sin\psi, 0] \quad (25a)$$

$$\vec{B}_r = E(x, y, z, t)[\sin\psi, \cos\psi, 0] \quad (25b)$$

where $E(x, y, z, t)$ is the wave amplitude and $\psi = kz - \omega t + \phi$ (Ref. 3).

To describe this problem of the interaction of electrons with the undulator and radiation fields, there are five coupled equations:

$$\frac{d\vec{p}}{dt} = -e(\vec{E} + \vec{\beta} \times \vec{B}) \quad (26)$$

$$\frac{d\gamma}{dt} = -\frac{e}{mc} \vec{\beta} \cdot \vec{E} \quad (27)$$

$$\gamma = \frac{1}{\sqrt{1 - \vec{\beta} \cdot \vec{\beta}}} \quad , \quad (28)$$

but only four unknowns: β_x , β_y , β_z , and γ , so we can neglect the z-component of (26).

The fields \vec{E} and \vec{B} in (26) and (27) are the sum of the radiation and undulator fields. Substituting (24) and equations (25) into the x- and y-components of (26), we get

$$\frac{d}{dt}(\gamma\vec{\beta}_\perp) = -\frac{e}{mc} \left[E(1 - \beta_z)[\cos\psi, -\sin\psi, 0] + \beta_z B_0[-\sin(k_0 z), \cos(k_0 z), 0] \right] \quad (29)$$

where we have used $\vec{p}_\perp = \gamma mc \vec{\beta}_\perp$ and $E = E(x, y, z, t)$. The right side of (29) contains two terms, the first of which is proportional to $(1 - \beta_z)$ and is surely small for relativistic electrons. We will neglect this term and keep only the dominant undulator term (i.e., that which is proportional to B_0). We can then integrate (29) and set the constant of integration to zero indicating perfect injection. The result is

$$\vec{\beta}_\perp = -\frac{K}{\gamma} [\cos(k_0 z), \sin(k_0 z), 0] \quad (30)$$

where $K = eB_0\lambda_0/2\pi mc^2$ is the undulator parameter since $\vec{B} = B_0$ in the helical undulator.

As mentioned earlier, \vec{E} is transverse and couples with only the transverse components of $\vec{\beta}$, that is, (30). Therefore substituting (30) into (27) we are left with

$$\dot{\gamma} = \frac{eEK}{\gamma mc} \cos(\zeta + \phi) \quad (31)$$

where ζ is given by (1) and ϕ is the phase of the optical field as discussed above.

As we noted earlier, (28) can be arranged as $\gamma^{-2} = 1 - \beta_1^2 - \beta_2^2$. If we substitute (30) for β_1^2 we get

$$\gamma^{-2} = \frac{1 - \beta_z^2}{1 + K^2} \quad (32)$$

which shows that a change in γ does not result in a change in β_1 , only in β_z . Taking the time derivative of both sides of (32) results in

$$\frac{\dot{\gamma}}{\gamma} = \frac{\gamma^2 \beta_z \dot{\beta}_z}{1 + K^2} \quad (33)$$

Construction of $\dot{\gamma}/\gamma$ from (31) and equating that with (33) results in

$$\ddot{\zeta} = \frac{1 + K^2}{\gamma^2} \frac{(k + k_0)c}{\beta_z} \frac{eEK}{\gamma^2 mc} \cos(\zeta + \phi) \quad (34)$$

where we have used $\dot{\beta}_z = \dot{\zeta}/(k + k_0)c$. We will now make approximations using $k \gg k_0$ and $\beta_z \approx 1$, and substitute for k using (5) to get

$$\ddot{\zeta} = \frac{2k_0 eEK}{\gamma^2 m} \cos(\zeta + \phi) \quad (35)$$

We can make (35) dimensionless by setting $d^2/dt^2 = (c/L)^2 d^2/d\tau^2$, which leaves us with

$$\ddot{\zeta} = |a| \cos(\zeta + \phi) \quad (36)$$

which is the pendulum equation. We have defined the dimensionless optical field amplitude $|a|$ as

$$|a| = \frac{4\pi NeKLE}{\gamma^2 mc^2} \quad (37)$$

The pendulum equation appropriate for the linear undulator can be found by the substitution $K \rightarrow K[J_0(\xi) - J_1(\xi)]$ in (37) (Ref. 3). Here $J_0(\xi)$ and $J_1(\xi)$ are Bessel functions of the first kind of order 0 and 1 and $\xi = K^2/2(1 + K^2)$.

Equation (36) shows that electrons with phase $-\pi/2 < (\zeta + \phi) < \pi/2$ have $\ddot{\zeta} > 0$ while those with $\pi/2 < (\zeta + \phi) < 3\pi/2$ have $\ddot{\zeta} < 0$. This difference in phase acceleration shows how electrons which are initially distributed randomly from $(\zeta + \phi) = -\pi/2$ to $(\zeta + \phi) = 3\pi/2$ are driven together, i.e., bunched, near $(\zeta + \phi) = \pi/2$ by the FEL interaction. In the next section, we will see what affect these bunched electrons have on the optical field.

D. THE FEL OPTICAL WAVE EQUATION

Knowing through the pendulum equation that the electrons will be bunched by the FEL interaction, we now find what affect those bunched electrons have on the classical radiation field. We use Maxwell's equations driven by the electron current to

determine the form of the FEL optical wave equation (Ref. 3).

Electrons in the undulator emit spontaneous radiation because they are made to accelerate. After approximately one pass, there is enough radiation in the optical cavity to take on a classical form (Ref. 3). Over the next several passes this spontaneous emission spectrum is narrowed. In many cases, the final FEL emission spectrum, or linewidth, is determined by the length of its optical pulses through the Fourier transform (Ref. 3). Short optical pulses result in broader spectra than long optical pulses. At this point in the operation of the FEL, the radiation wavelength is given by (5). Since we know that the emission spectrum of the FEL is narrow (it is a coherent light source), it must be that the amplitude and phase of the radiation field in the cavity are slowly varying in both time and space. We will invoke the slowly-varying amplitude and phase approximation in the following derivation of the FEL optical wave equation (Ref. 3).

The fields in the cavity of an FEL with a helical undulator are given by equations (25). Since the amplitude and phase are slowly varying in time, we can write the vector potential for these fields as

$$\vec{A} = \frac{E(x,y,z,t)c}{\omega} e^{i\psi} \hat{\epsilon} \quad (38)$$

where $\hat{\epsilon} = [-i, 1, 0]$ is the polarization vector and $\psi = kz - \omega t + \phi$. The potential for the physical fields is given by the real part of (38). The inhomogeneous wave equation for \vec{A} is given by

$$\left[\nabla^2 - \frac{1}{c^2} \frac{\partial^2}{\partial t^2} \right] \vec{A} = -\frac{4\pi}{c} \vec{J} \quad (39)$$

where \vec{J} is the driving current density (Ref. 5). The slowly-varying amplitude and phase approximation can be written as inequalities: $E' \ll kE$, $\phi' \ll k\phi$, $\dot{E} \ll \omega E$ and $\dot{\phi} \ll \omega\phi$ with $(\)' = \partial(\)/\partial z$ (Ref. 3). In the wave equation, this approximation has the effect of favoring first derivatives over all other terms. Substituting (38) into (39) and carrying out the z- and t- derivatives we are left with

$$\left[\nabla_{\perp}^2 + 2ik \left(\frac{\partial}{\partial z} + \frac{1}{c} \frac{\partial}{\partial t} \right) \right] E(x, y, z, t) e^{i\phi(x, y, z, t)} = -\frac{4\pi\omega}{c^2} \vec{J} \cdot \hat{\epsilon}^* e^{-i(kz - \omega t)} \quad (40)$$

where $\nabla_{\perp}^2 = \partial^2/\partial x^2 + \partial^2/\partial y^2$ and $\hat{\epsilon}^*$ is the complex conjugate of $\hat{\epsilon}$.

The driving current \vec{J} is given by

$$\vec{J}(x, y, z) = -ec \sum_i \delta(x - x_i) \delta(y - y_i) \delta(z - z_i) \vec{\beta}_i = -ec \sum_i \delta^{(3)}(\vec{r} - \vec{r}_i) \vec{\beta}_i \quad (41)$$

where $\delta(x)$ is the Dirac delta function, \vec{r} is the position vector of the field point (x, y, z) , \vec{r}_i is the position vector of the i^{th} electron, and the index i runs over all electrons in the micropulse. Substituting (30) and (41) into (40) and dividing by $2ik$ results in

$$\left[-\frac{i}{4} \frac{\lambda}{\pi} \nabla_{\perp}^2 + \left(\frac{\partial}{\partial z} + \frac{1}{c} \frac{\partial}{\partial t} \right) \right] E e^{i\phi} = -2\pi e K \sum_i \frac{e^{-i\zeta_i}}{\gamma_i} \delta^{(3)}(\vec{r} - \vec{r}_i) \quad (42)$$

where we have used (1) and $E = E(x, y, z, t)$.

We made the left side of (42) slowly varying by invoking the slowly varying amplitude and phase approximation. The right side is not slowly varying: it contains many Fourier components due to the presence of the delta functions which are each infinitely broadband. This means that while the left side describes an optical field that varies slowly, the right side can describe an optical field which varies arbitrarily fast. To smooth the right side we must replace the sum over all electrons by an average over some sample electrons. Since the fields in the cavity are slowly varying over several wavelengths by assumption, we only need to sample the electrons in one section of the micropulse one wavelength of light long and use the local charge density to weight the average. The result is

$$\left[-\frac{i}{4} \frac{\lambda}{\pi} \nabla_{\perp}^2 + \left(\frac{\partial}{\partial z} + \frac{1}{c} \frac{\partial}{\partial t} \right) \right] E e^{i\phi} = -2\pi e K \rho(z - c\beta_z t) \left\langle \frac{e^{-i\zeta}}{\gamma} \right\rangle_{(z - c\beta_z t)} \quad (43)$$

where $\rho(z - c\beta_z t)$ is the charge density of the traveling electron pulse, and $\langle \dots \rangle$ is an average over sampled electrons.

We can write (43) in a much simpler form if we change variables to $\tilde{z} = z - ct$ and use the dimensionless time τ . The coordinate \tilde{z} then follows a point on the optical pulse traveling at speed c from which the electron pulse slips back at speed $c(1 - \beta_z)$. In this coordinate system (let $z \rightarrow \tilde{z}$) we find that $L(\partial/\partial z + 1/c\partial/\partial t) = \partial/\partial \tau$. We can make (43) dimensionless by making the replacement $x, y \rightarrow \sqrt{\pi/\lambda L} x, y$ where $\sqrt{\lambda L/\pi}$ is the characteristic optical mode size. The result is

$$\left[-\frac{i}{4} \nabla_{\perp}^2 + \frac{\partial}{\partial \tau} \right] E e^{i\phi} = -2\pi e K L \rho \left\langle \frac{e^{-i\zeta}}{\gamma} \right\rangle \quad (44)$$

where we have assumed a long electron pulse so that ρ can be considered constant. Also, if the FEL efficiency is small so that changes in γ are small, (44) takes the form

$$\left[-\frac{i}{4} \nabla_{\perp}^2 + \frac{\partial}{\partial \tau} \right] a = -j \langle e^{-i\zeta} \rangle \quad (45)$$

where $a = |a| e^{i\phi}$, $|a|$ is given by (37), and the dimensionless current density j is

$$j = \frac{8N(e\pi K L)^2 \rho}{\gamma^3 m c^2} \quad (46)$$

To get the wave equation for an FEL with a linear undulator, we make the same substitution as before, $K \rightarrow K(J_0(\xi) - J_1(\xi))$, in both (37) and (46) (Ref. 3).

Now we will consider the physics contained in (45). First, we see that the growth of the field amplitude $\partial|a|/\partial\tau$ depends on both the current j and the wavefront curvature through the diffraction operator ∇_{\perp}^2 . This unnecessarily complicates our discussion, so we will assume for the moment that the light is constructed of plane waves so that $E(x, y, z, t) \rightarrow E(z, t)$ and $\nabla_{\perp}^2 a \rightarrow 0$. Then (45) takes the simple form

$$\dot{a} = -j \langle e^{-i\zeta} \rangle \quad (47)$$

We see that if $j = 0$, then $\dot{a} = 0$ and the field does not grow. Also, if there is no bunching, the electrons are randomly distributed throughout each wavelength of light, $\langle \exp(-i\zeta) \rangle = 0$ and again the field does not grow. Equating the real and imaginary parts of (47) leads to

$$\frac{\partial |a|}{\partial \tau} = -j \langle \cos(\zeta + \phi) \rangle \quad (48a)$$

$$|a| \frac{\partial \phi}{\partial \tau} = j \langle \sin(\zeta + \phi) \rangle \quad (48b)$$

which shows that the field amplitude $|a|$ grows when the electrons are bunched near $(\zeta + \phi) = \pi$ whereas the phase ϕ is driven when bunching is near $(\zeta + \phi) = \pi/2$.

The wave equation (45) and the pendulum equation (36), when coupled, allow the field and the electron phase space positions to evolve self-consistently. The pendulum equation describes the bunching of electrons in the presence of the undulator and radiation fields, while the wave equation shows how much the radiating bunch changes the optical field. The two equations form a feedback loop which under the right starting conditions leads to gain, our next topic.

E. GAIN

Now that we know how the electrons affect the optical field and vice versa we can translate this interaction to gain. FELs can be separated into two regions: low current/low gain defined by $j \ll 1$ and high current/high gain defined by $j \gg 1$ (Ref. 3). As it turns out, the low gain behavior we will analyze has a broader range of applicability, up to at least $j \approx 1$. An FEL with $j = 100$ will exhibit high gain characteristics. The difference between the low and high gain regions is in the growth rate of the optical field a (see (47)). We will find that the gain mechanisms in these two regions are different and therefore warrant a distinction between the two.

Gain for either high or low current is defined as

$$G = \frac{|a|^2 - a_0^2}{a_0^2} = \frac{\text{Energy Lost by Electrons}}{\text{Optical Field Energy}}, \quad (49)$$

where the last equality arises from conservation of energy. Here a_0 is the optical field strength seen by the electrons upon entering the undulator. Using (3), (4), and (5) it is

not difficult to show that the change in electron phase velocity due to a change in energy $\Delta\gamma/\gamma$ or wavelength emitted $\Delta\lambda/\lambda$ is

$$\Delta v = 4\pi N \frac{\Delta\gamma}{\gamma} , \quad (50a)$$

or

$$\Delta v = 2\pi N \frac{\Delta\lambda}{\lambda} , \quad (50b)$$

so that the energy lost by one electron can be expressed as

$$\Delta E = \frac{(v_0 - v)}{4\pi N} \gamma m c^2 \quad (51)$$

where $E = \gamma m c^2$ is the electron energy. The number of electrons in a volume of the optical mode dV is $\rho F dV$, where the filling factor F is the ratio of the cross sectional areas of the electron beam and optical mode. The optical energy contained in that same volume dV is $E^2 dV / 4\pi$ (Ref. 5). After some algebra we can write (49), letting $j \rightarrow jF$, as

$$G = \frac{2j}{a_0^2} \langle v_0 - v \rangle \quad (52)$$

which is valid for both low and high current. An average over the phase velocities v_i in the sampled portion of the electron beam is indicated by $\langle \dots \rangle$.

In the two subsections which follow we will discuss gain in the low current and high current FELs, respectively. We will find expressions for the single pass gain in both cases as a function of τ . In FEL design, low gain usually implies an oscillator configuration while high gain (e.g. $j = 10^4$) implies an amplifier in which electrons execute only one pass before the light is outcoupled. In this case, the dimensionless power $P = |a|^2$ evolves as $P = (1 + G)P_0$ and a large G ensures $P \gg P_0$. After n passes in the oscillator $P_n = (1 + G)^n P_0$ so although G is small, over many passes the light is amplified until $P_n \gg P_0$.

In the following analysis the wave equation is in the form (47). In section G we will discuss the effects of diffraction on the FEL interaction.

1. The Low Gain FEL

In exact analogy with a simple pendulum, the tool used to analyze the slow electron dynamics (bunching) in the FEL is their (ζ, v) phase space, one 2π section of which is one wavelength of light long.

In the low gain FEL, $j \ll 1$ implies through (47) that changes in the field are small. Multiplying both sides of (36) by $\dot{\zeta}$ and rearranging terms leads to

$$\frac{d}{d\tau} \left[\frac{v^2}{2} - |a| \sin(\zeta + \phi) \right] = 0 \quad (53)$$

and we recall that $v = \dot{\zeta}$. This has a simple solution

$$v(\zeta) = \pm \left[2H_0 + 2|a| \sin(\zeta + \phi) \right]^{1/2} \quad (54)$$

where $H_0 = v_0^2/2 - |a| \sin(\zeta_0 + \phi)$ is a constant of the motion for each electron starting at (ζ_0, v_0) and determines which phase space path $v(\zeta)$ it will traverse. These paths are plotted in Figure 2. For electrons starting on resonance $v_0 = 0$, (54) predicts fixed points at $(\zeta_0 + \phi) = \pi/2$ and $3\pi/2$. Analysis shows that the fixed point at $\pi/2$ is stable and surrounded nearby in phase space by harmonic orbits (Ref. 6). The fixed point at $3\pi/2$ is unstable and defines the path characterized by $H_0 = |a|$, called the separatrix, which is

$$v_s = \pm \sqrt{2|a|} \left[1 + \sin(\zeta + \phi) \right]^{1/2} . \quad (55)$$

The separatrix separates phase space into regions of closed and open orbits and has a peak to peak height of $4\sqrt{|a|}$ (Ref. 6). It is plotted in bold in Figure 2.

In Figure 3 we have distributed 20 resonant (i.e., $v_0 = 0$) electrons uniformly through phase space and show their evolution as $\tau : 0 \rightarrow 1$. At $\tau = 0$, the electron position is gray and steadily darkens as $\tau \rightarrow 1$. The phase space simulation solves the

wave and pendulum equations numerically with $j = 1$ and initial field amplitude $a_0 = 3$.

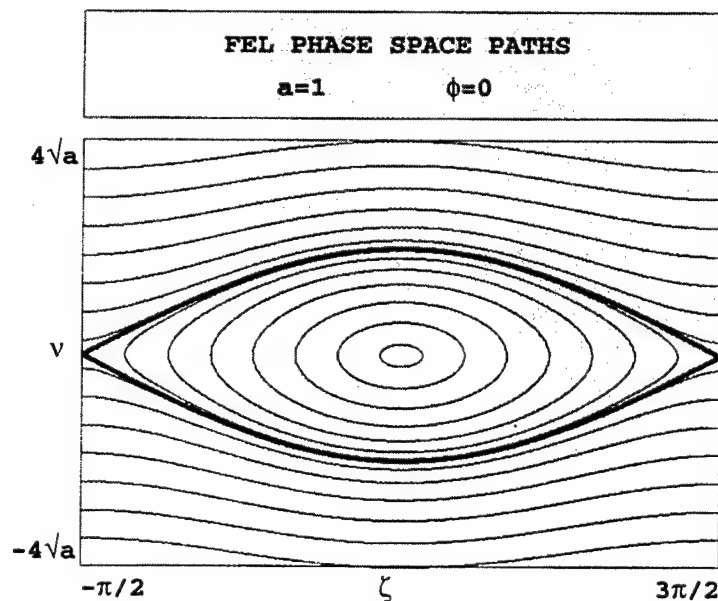


Figure 2. The phase space paths $v(\zeta)$ traversed by the electrons. The separatrix is drawn bold.

Since the electrons are resonant, they start and remain inside the separatrix on closed orbits. One can clearly see in Figure 3 that the electrons become bunched at $\zeta = \pi/2$, as predicted at the end of section C. Even though the electrons are bunched, however, gain is nearly zero because the electrons are bunched at the wrong phase for field amplitude growth. We can see in the figure that as many electrons move up in phase space and gain energy from the light wave (see (50a)) as move down in phase space and lose energy to the light wave. Something must be done to upset this balance in order to get a net gain.

It is interesting to note that Figure 3 shows a very small amount of gain. This is due to the slight phase shift given by (48b) which causes the bunch to move just

slightly toward $(\zeta + \phi) = \pi$.

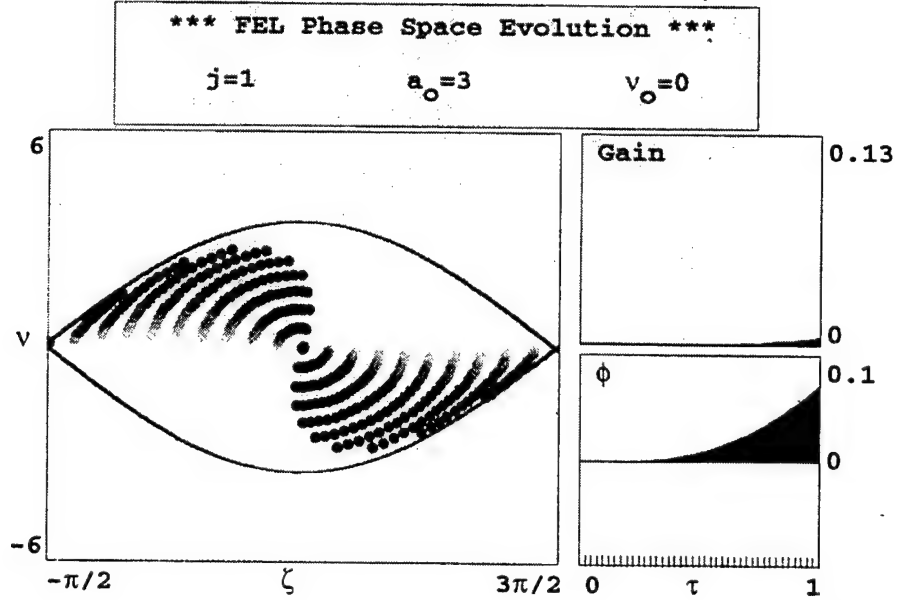


Figure 3. Phase space simulation of low gain FEL with electrons starting on resonance. Gain is negligible.

To get an analytic solution for the gain in a low current FEL, expand (36) in weak fields $|a| = a_0 \ll \pi$ with the result

$$v(\tau) = v_0 + \frac{a_0}{v_0} \left[\sin(\zeta_0 + v_0 \tau) - \sin(\zeta_0) \right] + \quad (56)$$

$$\frac{a_0^2}{v_0^3} \left[-\frac{1}{4} \left[\cos(2\zeta_0 + 2v_0 \tau) - \cos(2\zeta_0) \right] + \cos(v_0 \tau) - 1 - v_0 \tau \sin(\zeta_0) \cos(\zeta_0 + v_0 \tau) \right] + \dots ,$$

where $a_0 = |a(0)|$ and $\phi(0) = 0$ (Ref. 3). When we perform the average in (52) only the term proportional to a_0^2 in (56) survives and the result is

$$G(\tau) = j \left[\frac{2 - 2\cos(v_0 \tau) - v_0 \tau \sin(v_0 \tau)}{v_0^3} \right] . \quad (57)$$

We see that the gain at the end of the undulator ($\tau = 1$) depends only on the initial phase velocity and current density when the system is in weak optical fields.

In Figure 4 is the result of a simulation which solves the pendulum and wave equations numerically for many different initial phase velocities and plots the final gain $G(\tau = 1)$ and phase shift $\phi(\tau = 1)$ versus v_0 . The v_0 axis can be viewed as either a function of electron energy or emitted wavelength through equations (50). In the figure, v_0 ranges from -12 to 12, $j = 1$, and $a_0 = 0.001 \ll \pi$. The gain spectrum is anti-symmetric in agreement with (57) and has a maximum of $G = 0.13$ at $v_0 = 2.6$. The phase curve shows that the shift is maximum for resonant electrons, as discussed above, and is quite small where the gain is large.

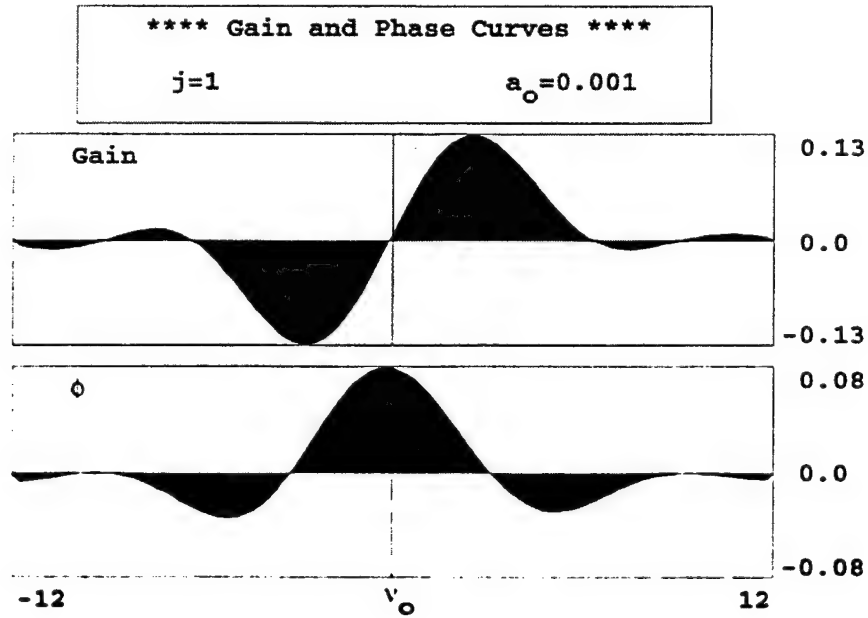


Figure 4. Gain and phase spectra for low gain FEL.
Gain is maximum at $v_0 = 2.6$.

We have in Figure 5 another phase space simulation using the same parameters as in Figure 3 except that $v_0 = 2.6$ in order to maximize gain. In this case only about half of the electrons are trapped in the separatrix while the other half are situated on open orbits. A clear bunch of electrons can be seen at $\zeta = \pi$ which affords maximum gain with a small phase shift ϕ . Compared with Figure 3, more electrons lost energy to the light wave than absorbed energy from the light wave. It is also true that if the electrons started at $v_0 = -2.6$ the result would be maximum absorption as more electrons would be absorbing energy than losing energy. This behavior could have been predicted from studying Figure 2: since all electrons travel nearly the same distance along their orbit (from (36)), starting them higher in phase space (i.e., $v_0 > 0$) results in electrons with $\zeta_0 \leq \pi/2$ traveling more or less parallel to the ζ axis, while those with $\zeta_0 \geq \pi/2$ travel down, losing energy.

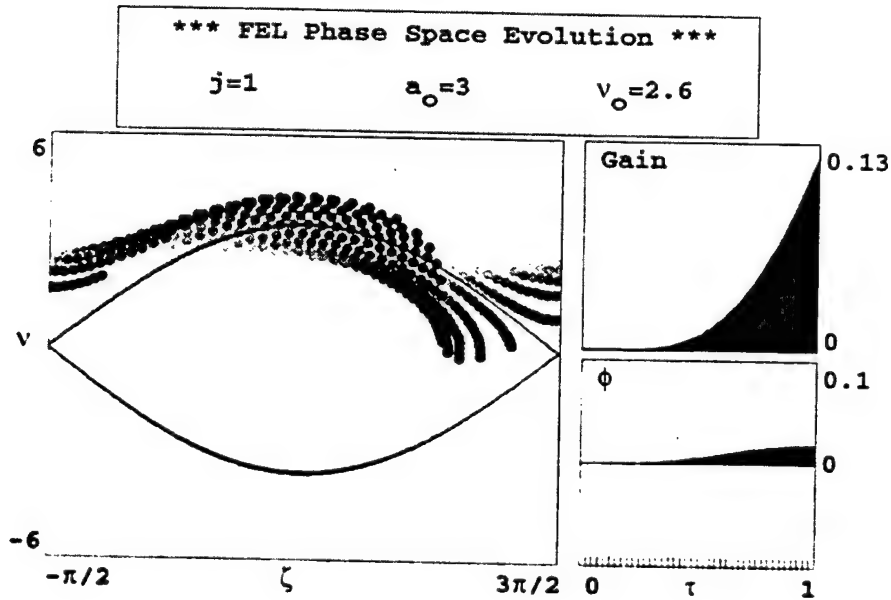


Figure 5. Phase space simulation of low gain FEL with electrons starting at $v_0 = 2.6$ for nearly maximum gain of $G = 0.12$ with $a_0 = 3$.

2. The High Gain FEL

In the high gain FEL, $j \gg 1$ and changes in the optical field are not small. Energy conservation cannot be used to determine the gain in this case because there is a substantial change in both the optical field amplitude and phase. It is still possible to obtain an analytic expression for the gain in weak optical fields; we merely state the result:

$$G(\tau) = \frac{1}{9} \exp\left[\left(\frac{1}{2}j\right)^{1/3} \sqrt{3}\tau\right] \quad (58)$$

where v_0 is set to zero (Ref. 3). Unlike the low gain FEL (57), here the gain is exponential in τ . We can ascertain the dependence on v_0 by using the same gain and phase simulation used in Figure 4. Shown in Figure 6 is that simulation with $j = 100$ and $a_0 = 0.001 \ll \pi$.

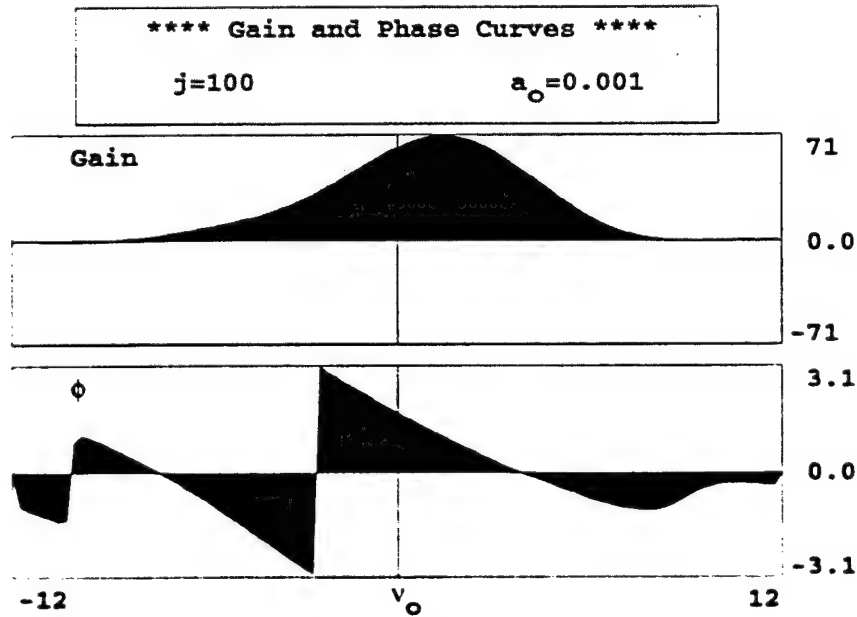


Figure 6. Gain and phase spectra for high gain FEL. Gain is maximum at $v_0 = 1.4$, but is still substantial at $v_0 = 0$ where the phase shift $\phi \approx \pi/2$.

The maximum gain is $G = 71$ at $v_0 = 1.4$, closer to resonance and much higher than in the low gain case (Figure 4). Note that the phase shift at maximum gain is quite large. The gain spectrum is nearly symmetric, and substantial gain exists at resonance where the phase shift $\phi \approx \pi/2$.

To understand the mechanism for high gain, a phase space simulation using $j = 100$, $a_0 = 1$, and $v_0 = 0$ is shown in Figure 7. The electrons which start at resonance drive the optical phase ϕ , represented in phase space by the shifting separatrix, and attempt to bunch at $\zeta = \pi/2$ as discussed earlier when considering Figure 3.

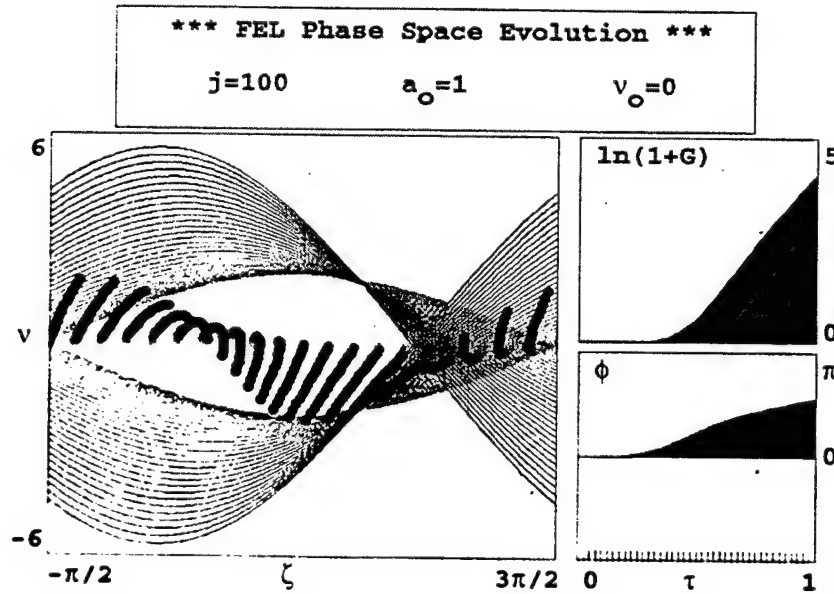


Figure 7. Phase space simulation of high gain FEL with electrons starting at resonance. Final gain $G = 62 = e^4$ and the phase shift $\phi \approx \pi/2$. The separatrix is shown growing with the field strength $|a|$ and shifting left as the phase ϕ grows.

It is the phase shift $\phi \approx \pi/2$ which allows gain as the relative electron bunch phase $(\zeta + \phi) \approx \pi$ drives the optical field amplitude. This leads to exponential gain (linear on the logarithmic plot of Figure 7) as predicted by (58).

To summarize, when $j \ll 1$ we must start the electrons at $v_0 > 0$ in order that they bunch near $(\zeta + \phi) = \pi$ and gain results. For an FEL with $j \gg 1$, electrons at $v_0 \approx 0$ drive the optical phase with the high current until the bunch is situated near $(\zeta + \phi) = \pi$. In the case of low gain, the optical phase shift is unimportant and small; in the case of high gain it is a crucial aspect of the interaction.

3. Gain Degradation Due to Electron Beam Quality

In section C.2 of this chapter, we discussed transverse electron beam quality and deduced two measures, σ_θ and σ_{v_θ} , from the emittance. The longitudinal beam quality has a measure

$$\sigma_G = 4\pi N \frac{\overline{\Delta\gamma}}{\gamma} \quad (59)$$

which is the standard deviation of a Gaussian spread in energy (see (17)), and $\overline{\Delta\gamma}mc^2$ is the rms energy difference from the resonant energy (Ref. 3).

Consider the low gain spectrum in Figure 3 again. The full width of the main positive gain portion at half the maximum is approximately π and the distance from maximum gain to maximum absorption is approximately 2π . Therefore, if the spread in phase velocities of the electron beam $\Delta v = \pi$, we should expect serious gain degradation as many electrons will be injected into the undulator with phase velocity corresponding to less than maximum or even to negative gain. Inspection of (50a) and (16) shows that Δv has contributions from σ_θ , σ_{v_θ} , and σ_G .

In Figure 8 is a phase space simulation using the same parameters as those used in Figure 5 except that a small energy spread $\sigma_G = 1$ has been included. Only the final phase space positions of the electrons have been plotted. The electrons are

spread through phase space and bunching has been degraded. Gain has been reduced to $G = 0.10$.

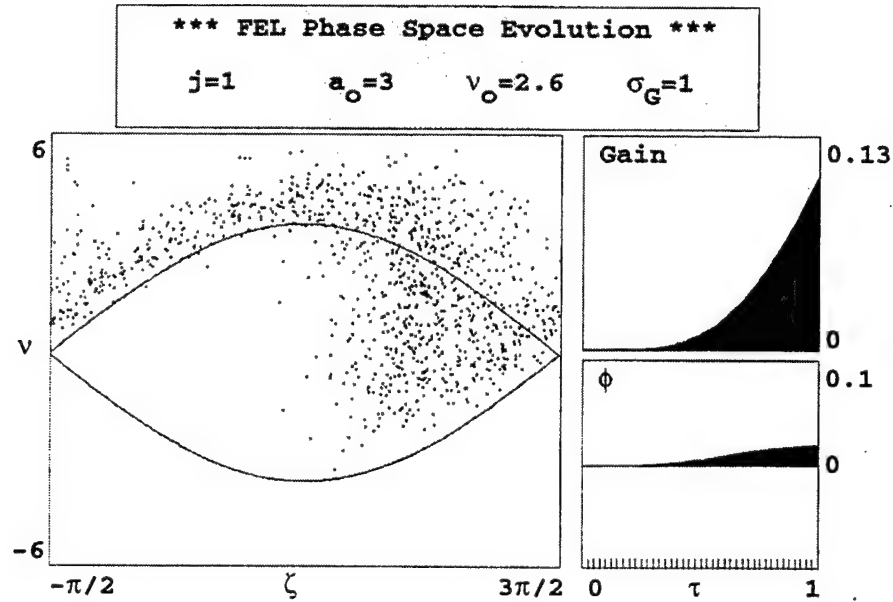


Figure 8. Phase space simulation of low gain FEL with energy spread $\sigma_G = 1$. Gain is reduced to $G = 0.10$. Compare with Figure 5.

In the high gain spectrum of Figure 6 we note that the gain spectrum bandwidth for $j = 100$ is approximately 2π . In general, this width is proportional to $j^{1/6}$ in the high gain region (Ref. 3). Since there are no regions of absorption and the spectrum is about twice as wide as that of the low gain example, we would expect the high gain FEL to be more resistant to beam quality effects. However, when increasing the undulator length, beam quality measures σ_G , (59), σ_θ , (18), and σ_{v_e} , (20) increase proportional to N . This means that the quality of the electron beam is magnified by a long undulator. Since $j \propto \hat{I}N^3$, where \hat{I} is the peak current, high gain is most easily

and often obtained by using a long undulator. In addition, higher peak current \hat{I} from the accelerator leads to poorer beam quality, so that either way the designer tries to maximize gain the problem with beam quality gets worse. When trying to get all one's light amplification in a single pass, little gain degradation can be tolerated. Indeed this may become one of the major drawbacks of using an FEL amplifier as a high power weapon.

In Figure 9 is a phase space simulation using the same parameters as those used in Figure 7 except in this case $\sigma_G = 1$. Only the final separatrix and electron phase space positions have been plotted. The electrons are spread throughout phase space and bunching has been degraded. Gain has been reduced from $G = 62$ to $G = 50$.

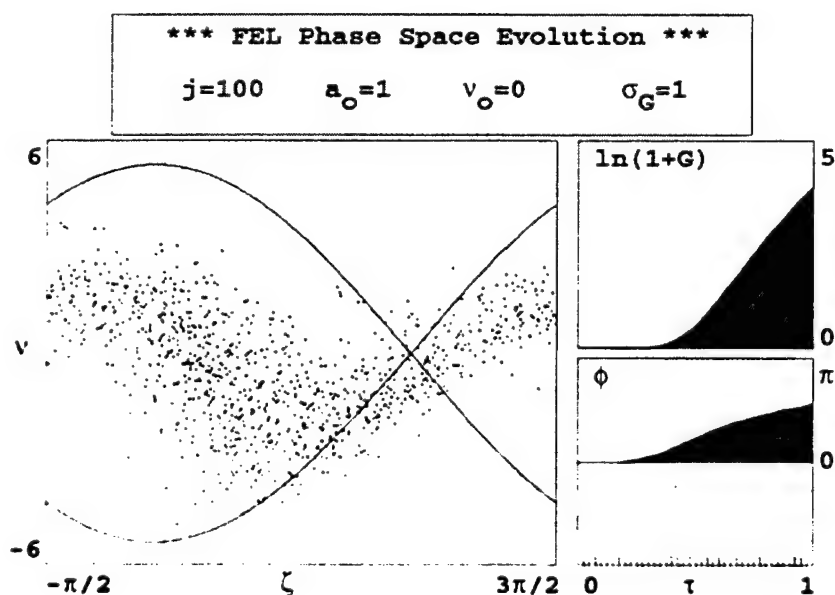


Figure 9. Phase space simulation of high gain FEL with energy spread $\sigma_G = 1$. Gain is reduced to $G = 50$. Compare with Figure 7, where $G = 62$.

In both Figures 8 and 9 we have only included the energy spread σ_G contribution to beam quality. Clearly the degradation would be even worse if we also included the effects of emittance.

F. SHORT PULSES

It was mentioned during our derivation of the wave equation that the electrons slip back relative to the light pulse at speed $c(1 - \beta_z)$. From the definition of resonance, we know that the distance between the leading edges of the electron and light pulses at $\tau = 1$ is $N\lambda$. This distance is called the "slippage length." If the electron pulse length is on the order of the slippage length, the pulse is considered short (Ref. 3). In this case we cannot make the long pulse assumption in (44) because each section of the light pulse sees the charge density changing as the electron pulse slips past.

In an optical resonator of length S , it takes time $2S/c$ for the optical pulse to make one round trip. Let the desynchronism d be the distance between the light and electron pulses at $\tau = 0$ on each pass (Ref. 3). We normalize d and the electron pulse length $\sigma_z = l_e/(N\lambda)$ to the slippage length. At exact synchronism, unbunched electrons slip back past the light pulse as $\tau : 0 \rightarrow 1$, bunching occurs, but only the rear of the light pulse gets amplified. On successive passes the delay in bunching becomes longer and the amplification moves further back on the light pulse. Since only the rear of the light pulse is being amplified while the losses (as determined by the resonator quality factor Q) are the same at all points in the pulse, its centroid moves at a speed slower than c . This is called "lethargy," and ultimately will lead the pulse out of the region of gain (that is, it won't overlap the electron pulse) and the pulse amplitude will vanish (Ref. 3).

To compensate for the effects of lethargy a small amount of desynchronism must be added. This is accomplished by reducing the path length S that the light

pulse must travel by adjusting the length of the optical cavity. In this case, $d = -\Delta S/(N\lambda)$ (Ref. 3).

Simulations of an FEL using picosecond electron pulses will be discussed in Chapter III. There we will explore the effects of desynchronism on the power evolution.

G. FEL WITH GAUSSIAN OPTICAL MODE

In section E on gain we discussed the interaction of the electron beam with light approximated by plane waves. An optical cavity bounded by spherical mirrors supports Hermite-Gaussian (and other) modes, which are solutions of (45) instead of (47) and accurately describe the laser beam inside and outside the cavity (Ref. 7). The optical beam can be constructed from any number of these modes, but the one most desired in a weapons laser for its propagation characteristics is called the fundamental Gaussian mode, or just Gaussian mode.

The usual Gaussian mode as given in Ref. 7 can be written in terms of our FEL dimensionless parameters. The result is

$$a_G = \frac{a_0}{w(\tau)} e^{-r^2/w^2 z_0} e^{i\phi_G(\tau)} \quad (60)$$

where

$$\phi_G(\tau) = -\tan^{-1} \left[\frac{\tau - \tau_w}{z_0} \right] + \frac{r^2(\tau - \tau_w)}{z_0^2 + (\tau - \tau_w)^2} \quad (61)$$

is the phase shift of the Gaussian mode relative to that of a plane wave,

$$w^2(\tau) = 1 + \left[\frac{\tau - \tau_w}{z_0} \right]^2 \quad (62)$$

is the square of the mode radius, which is normalized to the mode waist radius w_0^2 , and

$$z_0 = w_0^2 \quad (63)$$

is the dimensionless Rayleigh length (Ref. 3). The mode waist position is τ_w . Radial dimensions are normalized to $\sqrt{L\lambda/\pi}$, the characteristic mode size. We see in (62) that z_0 is the distance over which the mode area doubles. In a symmetric optical cavity with spherical mirrors a distance S apart and radii of curvature R , the dimensionless Rayleigh length is given by $z_0 = (2SR - S^2)^{1/2}/2L$ where L is again the undulator length (Ref. 7). The Rayleigh length z_0 and the waist position τ_w completely characterize the Gaussian mode in the optical cavity.

The amplitude of the Gaussian mode $|a|$ is a maximum at $\tau = \tau_w$ where $w^2(\tau) = 1$. It decreases away from the waist in both directions and is a minimum at both $\tau = 0$ and $\tau = 1$ (if $\tau_w = 0.5$). At any time τ , the amplitude decreases in the radial direction as a Gaussian, hence the name. The phase of the Gaussian mode ϕ_G (61) contains two terms. The first term provides a phase shift, called the Guoy phase shift, relative to the plane wave, and switches sign at the waist (Ref. 7). The second term in (61) decreases the phase shift for positions off-axis which creates the wavefront curvature necessary for focussing the beam at the waist.

In the electron phase space, the term $a_0/w(\tau)$ causes the height of the separatrix to increase as $\tau : 0 \rightarrow \tau_w$ and then decrease as $\tau : \tau_w \rightarrow 1$. The effect is proportional to $w^{-1/2}(\tau)$ (from our knowledge of the separatrix height) and complicates the phase space paths. The phase of the Gaussian mode (61) is continuously shifted as $\tau : 0 \rightarrow 1$. The shift has the sign opposite to that caused by the FEL interaction in (48b). It is therefore represented in phase space by the separatrix shifting to the right as $\tau : 0 \rightarrow 1$. Looking at Figure 2 again, we can predict that the electrons will have to start at a phase velocity $v_0' > 2.6$ in order to compensate for the shift and still bunch at the correct phase for gain. (Compare this to the case of the high gain FEL where the phase velocity had to be lowered in order to bunch at the correct phase.)

In order to observe the effects of the Gaussian mode on the FEL interaction, assume $z_0 \gg 1$, nearly plane waves, and expand (61) and (62) to first order in $(1/z_0)$. The phase becomes $\phi_G \approx -(\tau - \tau_w)/z_0$, and $w(\tau) \approx 1$. The pendulum equation (36) in the presence of the Gaussian mode is $\ddot{\zeta} = |a_G| \cos(\zeta + \phi_G)$ which for $z_0 \gg 1$ becomes

$$\ddot{\zeta} \approx a_0 e^{-r^2/z_0} \cos \left[\zeta_0 + \frac{\tau_w}{z_0} + \left[v_0 - \frac{1}{z_0} \right] \tau \right] \quad (64)$$

when expanded in weak fields to first order in a_0 (Ref. 3). Comparing (64) with (36) we see three distinct differences. First, the amplitude of the phase acceleration $\ddot{\zeta}$ decreases for electrons off axis because they see a weaker field strength $|a| \rightarrow a_0 \exp(-r^2/z_0)$. Second, there is a shift in the initial phase ζ_0 of all electrons in the amount τ_w/z_0 . This is inconsequential since the electrons are initially distributed uniformly throughout phase space. The last difference is in the phase velocity, which is decreased by $\Delta v = 1/z_0$. This leads to a wavelength change of $\Delta\lambda/\lambda = 1/(2\pi N z_0)$ from (50b). This also requires an increase in the initial phase velocity for maximum gain to $v_0^{\max} = 2.6 + 1/z_0$ in the low gain FEL. This effect is caused by the optical phase shift (61) and is shown in Figure 10. The figure is the result of a simulation similar to that in Figures 4 and 6 except that the finite size of the optical mode is included. Here the Rayleigh length $z_0 = 5$ and maximum gain is found at $v_0 = 2.9 \approx (2.6 + 1/5)$.

The presence of the Gaussian optical mode produces measurable effects in the performance of the FEL. This is the theme of the bulk of this work, including the final chapter on Compton backscattering where we calculate the photon emission rate for electrons in the Gaussian field of a laser.

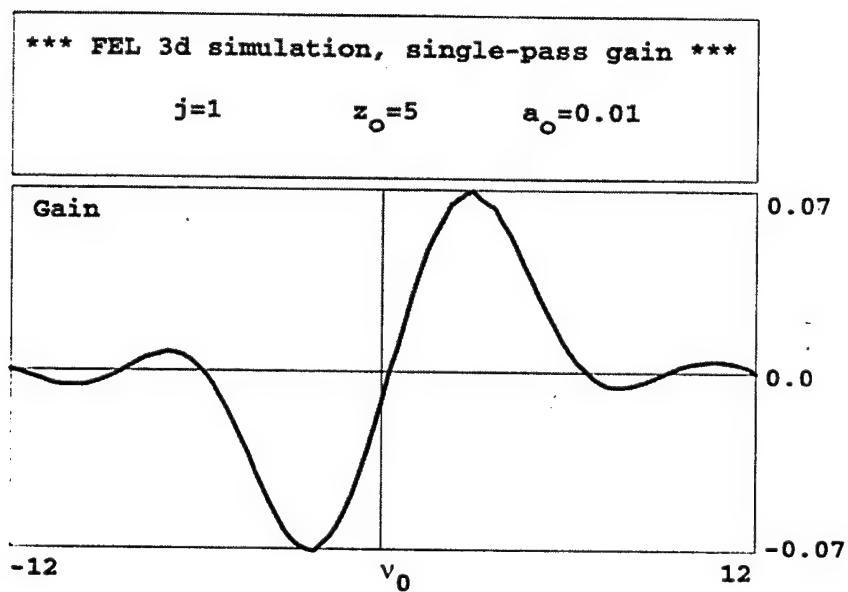


Figure 10. Gain spectrum for low gain FEL with Rayleigh length $z_0 = 5$. Maximum gain is achieved at $v_0 = 2.9$, shifted from $v_0 = 2.6$ by the Gaussian mode.

III. SIMULATIONS OF FIREFLY 1KW FEL

A. BACKGROUND

The FIREFLY (Far Infrared FEL) 1kW FEL at Stanford University was proposed in 1994 as an upgrade to the existing Infrared FEL at Stanford University (Ref. 8). With four new 10 MeV accelerator structures and a 5 MeV electron injector, an electron beam with energy 45 MeV could be generated. The electron injector operating at 11.8 MHz would produce an average current of $\bar{I} = 1$ ma, and the average power in the electron beam would be $\bar{P}_e = \bar{I}V = 45$ kW. A good measure of the maximum efficiency of an FEL, i.e., how much energy one can extract, is the gain spectrum bandwidth. Considering Figure 4 and (50b), we find that $\Delta\gamma/\gamma \approx 1/(2N)$. If we assume that we can extract the full $\Delta\gamma/\gamma = 1/(2N)$ from the beam with $N = 25$, then the average power out of the cavity would be $\bar{P} = \bar{P}_e/(2N) = 900$ W. This average power would be almost 100 times greater than the world's most powerful FEL, and it was estimated this could be done for only one million dollars with existing technology.

The proposed FEL and two variants with lower electron beam energies of 25 MeV and 10 MeV were simulated. All other parameters were kept the same and are listed in Table 1.

B. SIMULATIONS AND RESULTS

Because all three FELs simulated have emission wavelengths λ in the far infrared, the characteristic mode size $\sqrt{L\lambda}\pi$ is large enough that diffraction (i.e., the Gaussian mode) should not dominate the interaction. The slippage length $N\lambda$, compared to the electron pulse length, is also large, so the effects of short optical pulses must be addressed. (Some basic consideration of short pulse effects was done in section F of Chapter II.) To study short pulse effects, simulations following longitudinal multimodes were used. These simulations divide the optical pulse into a

number of fixed longitudinal field sites, or bins, $a(z)$ (Ref. 3). The simulations are called "longitudinal multimode" because dividing the optical pulse into longitudinal sites $a \rightarrow a(z)$ is equivalent to $a \rightarrow a(k_z)$ in Fourier space; the number of sites z is equivalent to a number of modes k_z .

	I	II	III
Beam Energy	45 MeV	25 MeV	10 MeV
Peak Current	40 A	40 A	40 A
Micropulse Length	2.1 ps	2.1 ps	2.1 ps
Undulator Type	Linear	Linear	Linear
K	1.1	1.1	1.1
N	25	25	25
λ_0	6.0 cm	6.0 cm	6.0 cm
λ	8.4 μm	26.6 μm	156.7 μm
j	1.7	2.9	7.2
σ_z	3.2	1.0	0.2

Table 1. Parameters for FIREFLY 1kW FEL (column I) and two variants (columns II and III) used in simulations.

The slower moving electrons slip back past the optical pulse to sites $z - \tau$ and interact with a number of field sites corresponding to the slippage distance $N\lambda$ (recall that z is normalized to the slippage distance). Conversely, each field site $a(z)$ interacts with a length $N\lambda$ along the electron micropulse as the micropulse slips back. We generalize the pendulum (36) and wave (47) equations to include the slippage:

$$\zeta_{z+\tau}^{\circ} = |a_z| \cos(\zeta_{z+\tau} + \phi_z) \quad (65)$$

$$\dot{a}_z^{\circ} = -j_{z+\tau} \langle e^{-i\zeta_{z+\tau}} \rangle_{z+\tau} \quad (66)$$

As $\tau : 0 \rightarrow 1$ in increments of $\Delta\tau$ in the simulation, (65) and (66) show how the field changes at site z are caused by the electron dynamics at the micropulse site $z + s \Delta\tau$, where $s = 0, 1, 2, \dots, N_t$ is an integer and $N_t = 1/\Delta\tau$ is the total number of time steps, and vice versa.

Contained in Figure 11 is the output from a simulation of the 1 kW machine, whose parameters are listed in column I of Table 1. The dimensionless current density is $j = 1.7$, the micropulse length is $\sigma_z = 3.2$, cavity losses are determined by $Q = 100$, and the desynchronism $d = 0.03$ is large (see Chapter II section F for definition of d).

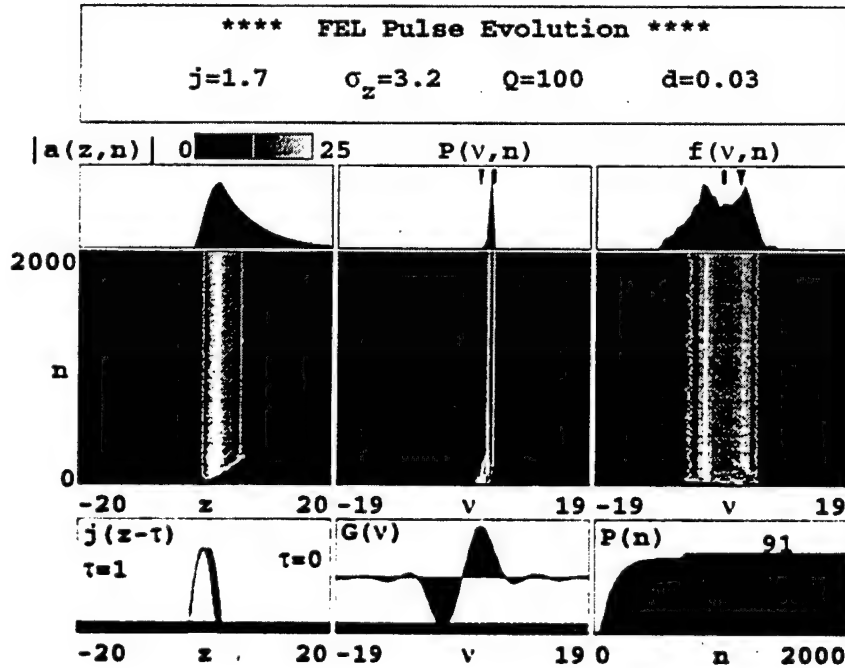


Figure 11. Longitudinal multimode simulation of FIREFLY.

The parabolic electron pulse is drawn in the lower left window at $\tau = 0$ and at $\tau = 1$ to illustrate slippage. Above the electron pulse is plotted the optical field amplitude $|a(z,n)|$ at each pass n . The scale ranges from zero in black to the maximum in white; a contour line is drawn at the median field amplitude. Above the field evolution is plotted the final optical field amplitude $|a(z,n = 2000)|$ in black. At the bottom center is drawn the gain spectrum (57). Above this is the optical power spectrum evolution $P(v,n)$, with the final power spectrum $P(v,n = 2000)$ drawn on top in black. The power spectrum $P(v,n)$ is the Fourier transform of the square of the optical field $|a(z,n)|^2$ at each pass n . The phase velocity v in the power spectrum is used in the sense of (50b); that is, it represents the wavelength λ so that $P(v,n)$ shows the linewidth of the radiation. The total power evolution $P(n)$ is plotted at lower right in the figure. Above this is plotted the electron phase velocity distribution $f(v,n)$. The distribution $f(v,n)$ is a projection of the final electron phase space positions (ζ,v) onto the v -axis at each pass n . As such, v in this plot is to be understood in the sense of (50a); that is, it represents the electron energy γmc^2 so that $f(v,n)$ is interpreted as an energy spread.

Having described all the plots in Figure 11, we now interpret their features. The large desynchronism has caused the optical pulse $|a(z,n)|$ to be artificially long by advancing the front edge of the pulse ahead of the electrons. The electron pulse amplifies only the trailing edge of the optical pulse on each pass. This leads to reduced coupling; the peak field strength is only $|a| = 25$. As evidenced by the power spectrum $P(v,n)$, the long, smooth optical pulse leads to a narrow linewidth. The electron phase velocity distribution $f(v,n)$ does not evolve any further after the first few hundred passes. At saturation, the electrons reach the bottom of the separatrix in phase space (Ref. 3). This means that the electron distribution $f(v,n)$ should have a width of about $4\sqrt{|a|} \approx 18$ at saturation, the peak-to-peak height of the separatrix at $|a| \approx 20$, the final field amplitude. In the figure, the width of $f(v,n)$ is about 18, showing good agreement. The power $P(n)$ at each pass n is obtained by integrating

over the optical pulse $|a(z,n)|^2$. The power evolution $P(n)$ plotted at lower right shows that a steady state is reached after approximately $n = 700$ passes where $P(n) = 91$.

Plotted in Figure 12 are the results of several simulations like that above. The steady state dimensionless power is plotted versus the desynchronism.

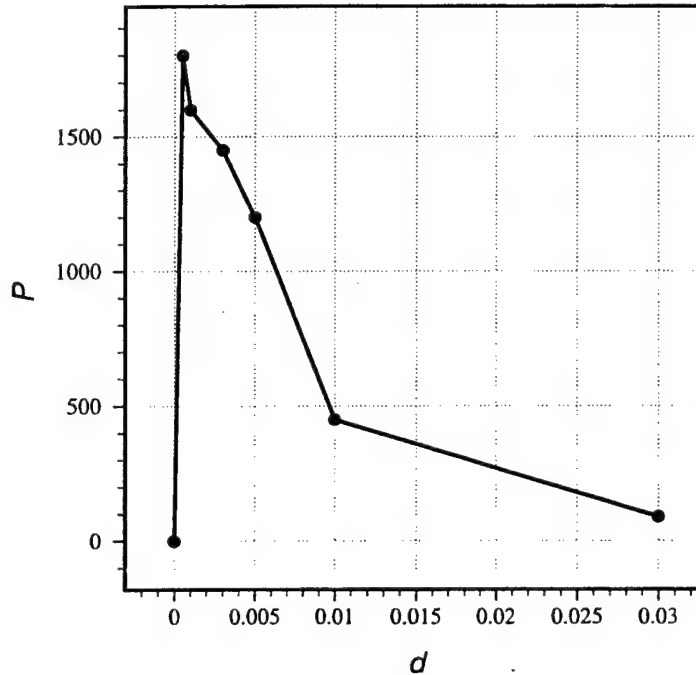


Figure 12. Plot of outcoupled dimensionless power versus desynchronism for FIREFLY.

The maximum on the curve at $d = 0.0005$ corresponds to an actual output average power $\bar{P} = 900$ W, the desired output, but requires the injector to operate at 23.6 MHz, or double the rate discussed earlier. Evidently the short pulses lead to reduced coupling between the electrons and optical field, lowering FEL efficiency. Doubling the operating frequency of the electron injector was proposed in Ref. 8 as a follow-on to the 1 kW upgrade for the purpose of attaining 2 kW average power. Note that the

maximum in Figure 12 is rather sharp. Since the slightest change in d can produce a large change in the output, the FEL is less stable when operated in this region (Ref. 3).

The FIREFLY variant listed in column II of Table 1 has a shorter dimensionless electron pulse length σ_z than that in Figure 11. The output of a simulation with $j = 2.9$, $\sigma_z = 1$, $Q = 100$, and $d = 0.005$ is shown in Figure 13. The features of the plots show the occurrence of the trapped-particle instability (Ref. 3).

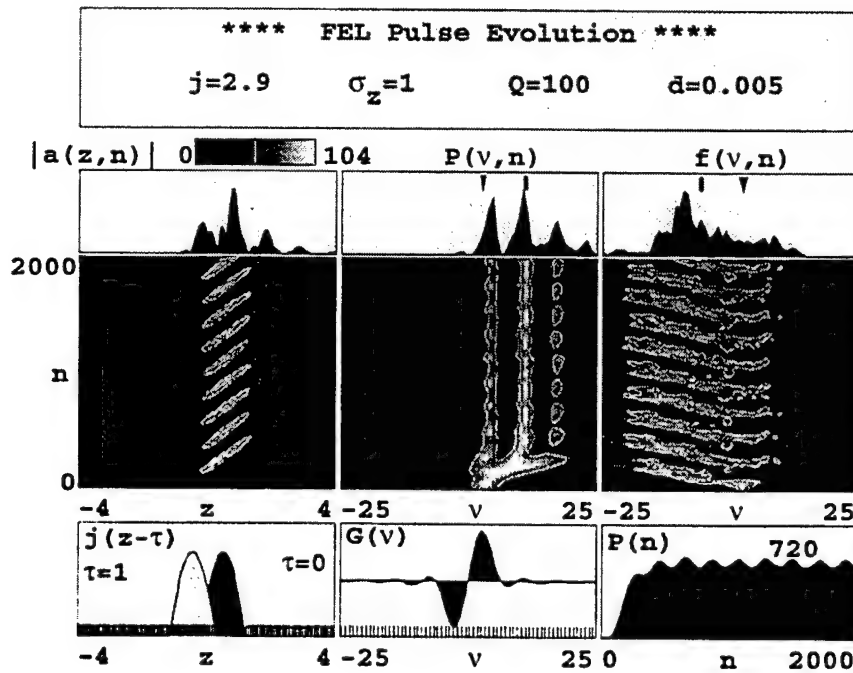


Figure 13. Longitudinal multimode simulation for the variant of FIREFLY listed in column II of Table 1.

This instability occurs when the field amplitude $|a|$ becomes so strong that electrons in phase space traverse their entire path (see Figure 2) during a single pass through the undulator, executing a synchrotron oscillation with frequency $\nu_s = \sqrt{|a|} \approx 2\pi$ (Ref. 3). In real space, this oscillation represents motion superimposed on the electron

trajectory and leads to emission into sidebands $\nu_0 \pm \nu_s$ (Ref. 3). As these sidebands grow, the FEL power will increase and the fields will get stronger, causing more electrons to execute synchrotron oscillations, etc. At least four sidebands can be seen in the power spectrum $P(\nu, n)$ in Figure 13. These sidebands modulate the optical pulse envelope $|a(z, n)|$ as shown, and the increased field strength causes the wide electron distribution $f(\nu, n)$. In this case, the instability has imposed a periodic structure on the optical field envelope $|a(z, n)|$ and the power spectrum $P(\nu, n)$ which results in oscillations in the total power $P(n)$ over many passes n .

Figure 14 plots the dimensionless power versus desynchronism from several simulations like that of Figure 13.

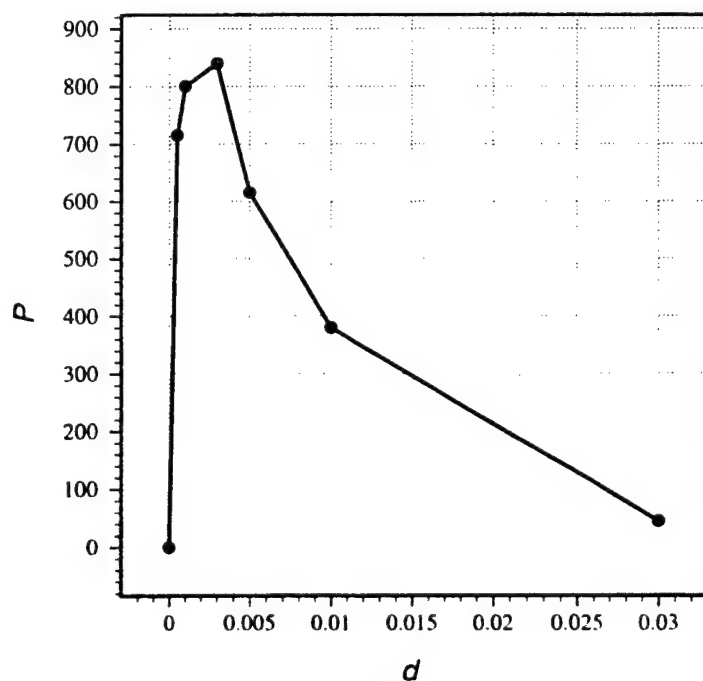


Figure 14. Plot of dimensionless outcoupled power versus desynchronism for variant of FIREFLY listed in column II of Table 1.

We see from the plot that Figure 12 with $d = 0.005$ lies in the transition region in the desynchronism curve, where the fields are strong enough to cause the trapped-particle instability, but where operation of the FEL is relatively stable. The peak in this curve at $d = 0.003$ corresponds to an outcoupled average power of $\bar{P} = 140$ W.

To further illustrate the effects of slippage, the example listed in column III represents FIREFLY operating at a much longer wavelength $\lambda = 156.7$ μm . The slippage length is therefore long and leads to a small value of $\sigma_z = 0.2$. Figure 15 contains the result of a simulation using $j = 7.2$, $\sigma_z = 0.2$, $Q = 100$, and the very small value of $d = 0.0005$.

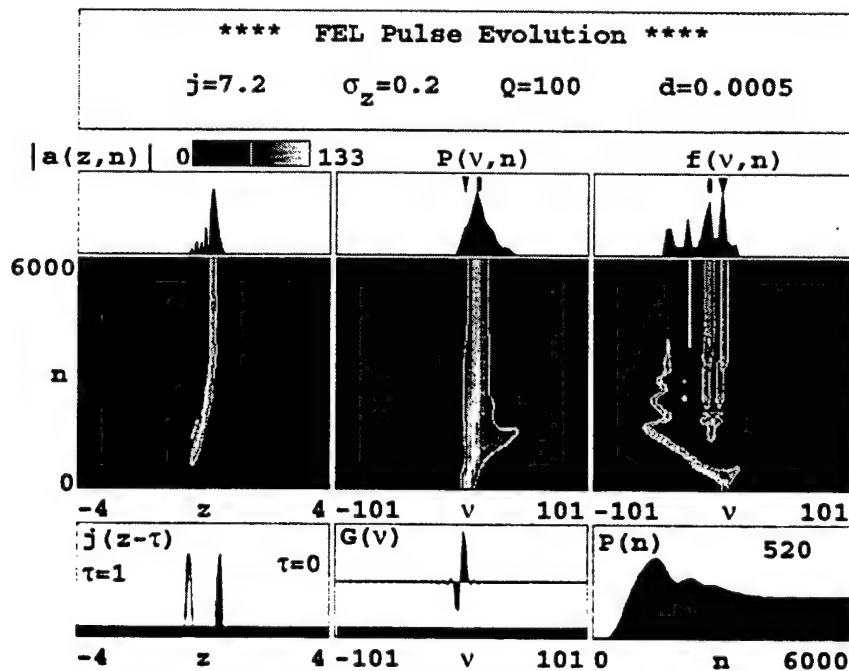


Figure 15. Longitudinal multimode simulation for variant of FIREFLY listed in column III of Table 1.

The small desynchronism means that, unlike in Figure 11, the light pulse $|a(z,n)|$ has not been artificially lengthened. The optical pulse reaches steady state with a length

comparable to the electron pulse length shown in the plot at lower left. The fields are strong and the trapped-particle instability again leads to structure in the optical pulse. We should note here that the spikes to the left of the main optical pulse are only about one wavelength of light in length. Because this would violate the slowly-varying amplitude assumption in the wave equation (47), these may be meaningless. The short, modulated optical pulse results in a broad power spectrum $P(v,n)$ (note the scale in v compared with that in Figure 13). The strong fields also result in a broad electron distribution. Maximum power $P(n) = 900$ is achieved at $n \approx 1500$ passes, but steady-state $P(n) = 520$ isn't reached until $n \approx 4000$ passes which is predicted to take about 0.3 ms in FIREFLY.

Figure 16 plots power versus desynchronism for column III of Table 1.

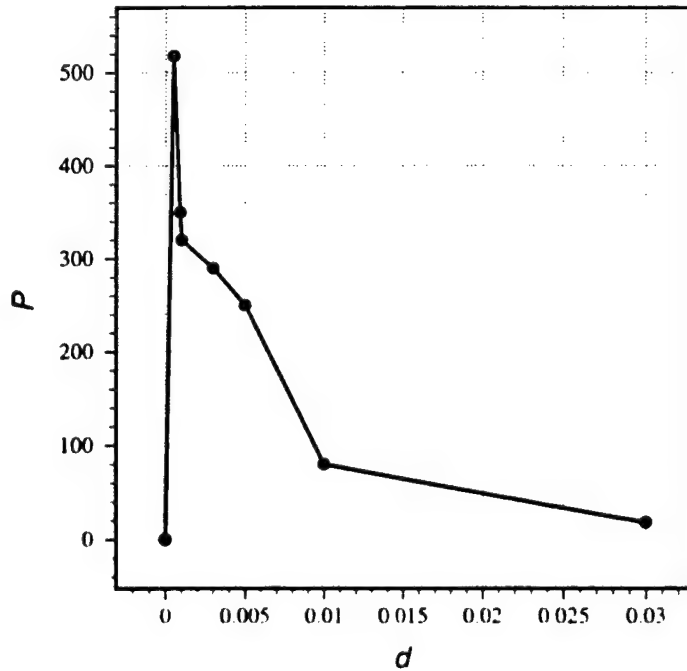


Figure 16. Plot of outcoupled dimensionless power versus desynchronism for variant of FIREFLY listed in column III of Table 1.

We note that $d = 0.0005$, that used in Figure 15, is the location of the peak in this curve and corresponds to an average power of $\bar{P} = 17$ W.

C. CONCLUSIONS

The operational characteristics of far infrared wavelength FELs driven by short, picosecond electron micropulses will be determined by short pulse effects. The desynchronism coupled with the cavity Q will affect the length and structure of the optical pulse. This in turn determines the width and structure of the power spectrum.

Based on our simulations of the 1 kW FEL, as depicted in Figures 11 and 12, the goal of 1 kW average power can be achieved, but at double the electron injector duty cycle first proposed. More simulations should be done to substantiate this possibility. Doubling the injector duty cycle was proposed in Ref. 8, but as a follow-on to the 1 kW proposal as a means of achieving 2 kW. We also note that the trapped-particle instability will probably occur.

IV. TRANSVERSE EFFECTS IN UV FREE ELECTRON LASERS

A. BACKGROUND

In an ultraviolet free electron laser (UVFEL), the characteristic optical mode size $\sqrt{L\lambda/\pi}$ tends to be small because of the short optical wavelength λ . For example, if $\lambda = 200$ nm and $L = 3$ m, $\sqrt{L\lambda/\pi} = 0.4$ mm. This is also approximately the size of the electron beam. For the ultraviolet FEL, the effects of the spatial extent of the electron beam as compared to the optical mode are of concern.

The UVFEL under consideration in this chapter is that proposed by the Laser Processing Consortium (LPC) at Thomas Jefferson National Accelerator Facility (TJNAF) in Newport News, Virginia (Ref. 9). The LPC is a group of industry and university scientists and engineers interested in an efficient, reliable, coherent UV light source for processing materials. On the order of 100 kW of UV light is needed to process commercial products ranging from nylon to steel. The parameters for the UVFEL proposed in Ref. 9 are listed in Table 2.

Beam Energy	200 MeV
Peak Current	270 A
Micropulse Length	0.25 ps
Undulator Type	Linear
K	0.95
N	72
λ_0	3.3 cm
λ	204 nm

Table 2. Parameters for the LPC proposed UVFEL.

In this chapter we analyze the LPC UVFEL using transverse multimode simulations. These simulations are described in section B. We use these simulations in section C to study the effects of the optical mode size on FEL gain. In section D we study the effects of electron beam focussing on FEL gain.

B. TRANSVERSE MULTIMODE SIMULATIONS

In Chapter III we extended the pendulum and wave equations in the z-direction in order to properly simulate longitudinal multimodes by dividing the optical pulse into z sites. To simulate transverse multimodes, we make the same transition in the x- and y-directions. The optical field is extended to sites in x and y so that $a \rightarrow a(x,y)$. Generalizing the wave equation (45) and the pendulum equation (36) gives (Ref. 3):

$$\left[-\frac{i}{4} \nabla_{\perp}^2 + \frac{\partial}{\partial \tau} \right] a(x,y,\tau) = -\langle j \exp(-i\zeta(x,y,\tau)) \rangle_{(x,y,\tau)} \quad (67)$$

$$\zeta(x,y,\tau) = \left| a(x,y,\tau) \right| \cos \left[\zeta(x,y,\tau) + \phi(x,y,\tau) \right] \quad (68)$$

The transverse dimensions are normalized to the characteristic mode size $\sqrt{\lambda L / \pi}$. The set of equations (67) and (68) are fully self-consistent in three dimensions (x,y,τ) .

For the UVFEL represented in Table 2, we calculate an electron pulse length slightly greater than five slippage distances $\sigma_z = 5.1$. Therefore, it can be assumed that slippage will not be an important consideration, so that we may follow only one representative longitudinal site as in (67) and (68).

In section G of Chapter II, we discussed the fundamental Gaussian mode but mentioned that in general any number of Hermite-Gaussian transverse modes are present. In order to model the evolution of the FEL from weak fields through saturation, these higher-order modes are included as the FEL interaction amplifies and distorts the optical mode. Both the optical field amplitude and phase can be altered (Ref. 3). An example of this is shown in Figure 17.

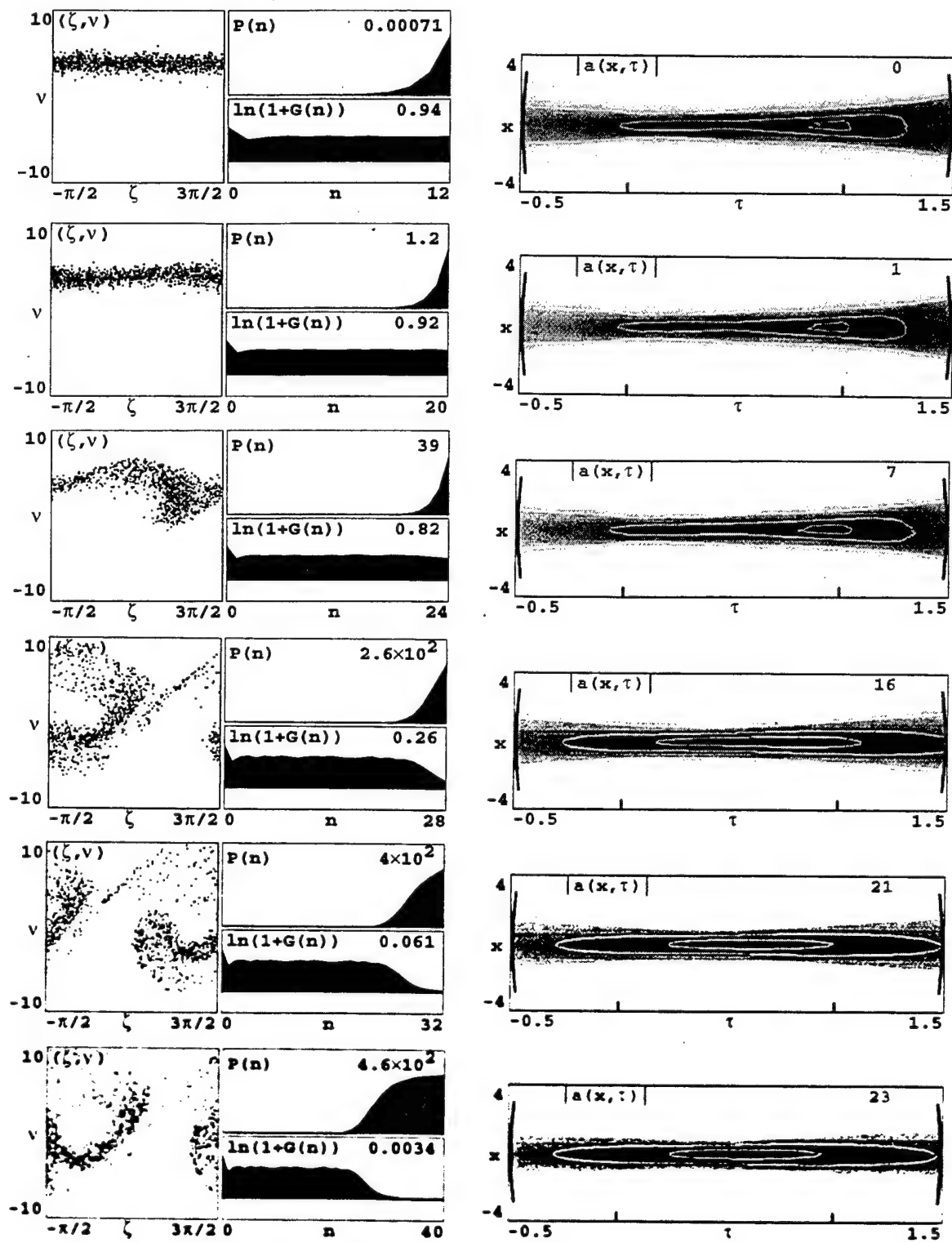


Figure 17. Optical multimode evolution from weak fields through saturation.

Figure 17 shows the evolution of the FEL from weak fields $a_0 = 0.0001$ through saturation using $j = 20$ and a small energy spread $\sigma_G = 0.5$. The Rayleigh length for the cavity is $z_0 = 0.5$. The top set of plots show the FEL oscillator after $n = 12$ passes. The electron phase space plot shows no noticeable bunching and the final gain $G = 0.94$ is in steady state (i.e., $G(n)$ constant) with power increasing exponentially. At right is shown the optical field amplitude between the mirrors $|a(x, \tau)|$. The mode is clearly distorted from a fundamental Gaussian mode with the peak field (in black) located at $\tau = 1$ where single pass gain is the maximum. Moving down the set of figures, the electron phase space begins to exhibit bunching at $n = 24$. The bunch descends along the v -axis, indicating energy loss, and near saturation at $n = 28$ it starts to ascend taking energy back from the optical field. At saturation ($n = 40$), the electron bunch is clearly moving up in phase space at $\tau = 1$. The motion of the electron bunch through phase space, caused by the strengthening fields, is attended by a drop in final gain $G(\tau=1)$ as the electrons are absorbing light at the end of the undulator. This means that on each pass, $G(\tau)$ peaks at $\tau < 1$ along the undulator and the peak field moves back along the undulator. Scanning down the page through the plots of $|a(x, \tau)|$, we see the peak field strength moving back along the undulator. At saturation, the peak gain per pass is nearly at the middle of the undulator and the final gain is reduced to $G = 0.0034$. The optical field $|a(x, \tau)|$ resembles the fundamental Gaussian mode at saturation where the gain is low.

The evolution of the distorted optical mode to the Gaussian requires the use of the transverse multimode simulations described above. Multiple transverse modes are included in the simulation to construct the distorted optical fields of Figure 17 for the same reason it takes a large number of sine waves to synthesize a square pulse in Fourier analysis.

C. OPTICAL MODE SIZE EFFECT ON FEL GAIN

It has been shown that the Rayleigh length which optimizes gain for a filament electron beam (i.e., $\sigma_e \approx 0$) is $z_0 = 1/\sqrt{12} \approx 0.3$ (Refs. 3, 10). This is the Rayleigh length which maximizes the average filling factor \bar{F} (averaged along the undulator length) by minimizing the volume occupied by the Gaussian optical mode around the electron beam. Reference 10 also discusses gain in a Gaussian mode for non-zero electron beam radius, but again using arguments based on the filling factor. The conclusion, not surprisingly, is that maximum gain is achieved when the Rayleigh length is chosen such that the electron beam fits inside the optical mode (recall $z_0 = w_0^2$). But in the case of the UVFEL, it may be necessary to have an electron beam bigger than the optical mode because of the small mode size $\sqrt{\lambda L/\pi}$. In that case, one cannot quantify gain in terms of the filling factor, which may be greater than one. The three dimensional simulations described in the previous section are used to find the influence of the Rayleigh length on FEL gain.

Figure 18 shows the result of a three-dimensional, transverse multimode simulation of the UVFEL parameters listed in Table 2. The corresponding dimensionless parameters are current density $j = 30$ with F is no longer included in j , $v_0 = 4.5$ is the optimum initial phase velocity, the Rayleigh length is $z_0 = 0.3$, $a_0 = 0.001$ is the initial optical field amplitude, the cavity loss is $Q = 5$, $\sigma_e = 0.45$ is the dimensionless electron beam radius, $\sigma_\theta = 0.9$ is the angular spread, the energy spread is $\sigma_G = 1.3$, and $\omega_p = 1.0$ is the betatron frequency. The dimensionless emittance $\epsilon = 0.43$ corresponds to an actual normalized emittance $\epsilon_N = 11\pi$ mm-mrad ($\epsilon_N = \gamma \epsilon_{rms}$). The plot at top left shows the evolution of the optical field amplitude at the end of the undulator with each pass $|a(x,n)|$. To the right is plotted the final optical field amplitude at the right-hand mirror $|a(x,y)|$. The optical field between the mirrors $|a(x,\tau)|$ at $y = 0$ is plotted in the center; the tick marks at $\tau = 0$ and $\tau = 1$ show the beginning and end of the undulator. Overlaid on this plot are the positions of a

random sample of the electrons used in the simulation. In this figure, $\sigma_e/w_0 = 0.8$ and the electrons near the edges of the Gaussian mode see weaker optical fields and thus a degraded interaction (see (60)).

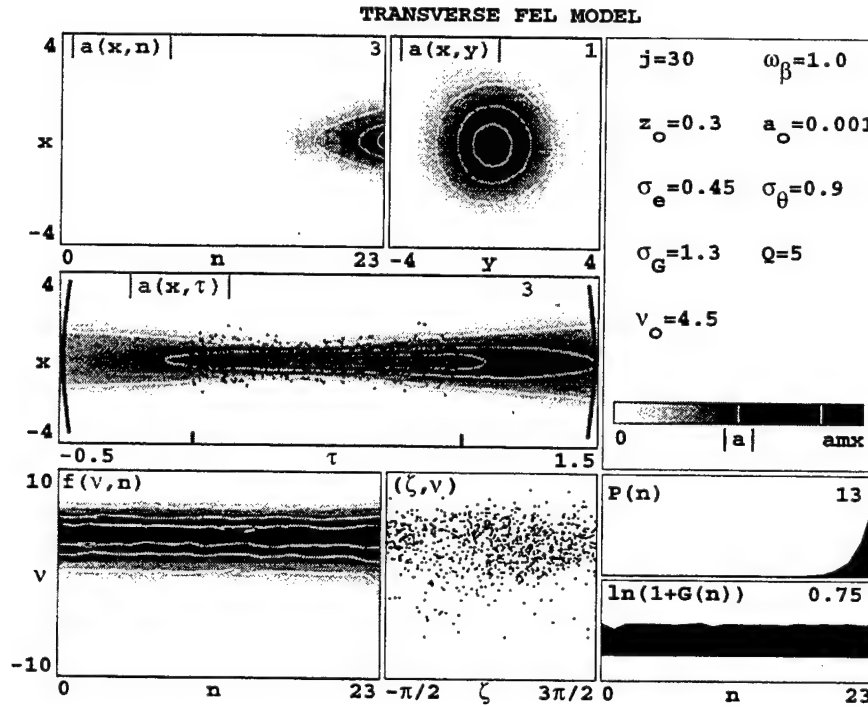


Figure 18. Transverse multimode simulation of UVFEL. Gain is degraded due to large electron beam radius/optical mode waist radius ratio $\sigma_e/w_0 = 0.8$.

The plots along bottom show the electron phase velocity distribution at each pass $f(v,n)$, the final phase space positions (ζ, v) of a sample of electrons, and the power $P(n)$ and gain $\ln(1+G(n))$ evolutions. The gain $G(n)$ is plotted at the end of the undulator $G(\tau=1)$ after each pass n . These plots show FEL gain in steady state (i.e., $G(n)$ approximately constant) with final gain $G = 0.75$ and power increasing exponentially. Electrons in phase space are spread out due to σ_G and σ_θ so that bunching can barely be seen at $\zeta \approx \pi$ even though the limit of weak fields $|a| \approx \pi$ has been reached.

The results of many simulations like that in Figure 18 were used to plot gain normalized to the maximum one-dimensional gain, $G_0 = 0.135j\bar{F}$, where $\bar{F} = \pi\sigma_\theta^2/(z_0 + 1/12z_0)$ is the average filling factor, versus Rayleigh length (Refs. 3, 10). The result is plotted in Figure 19.

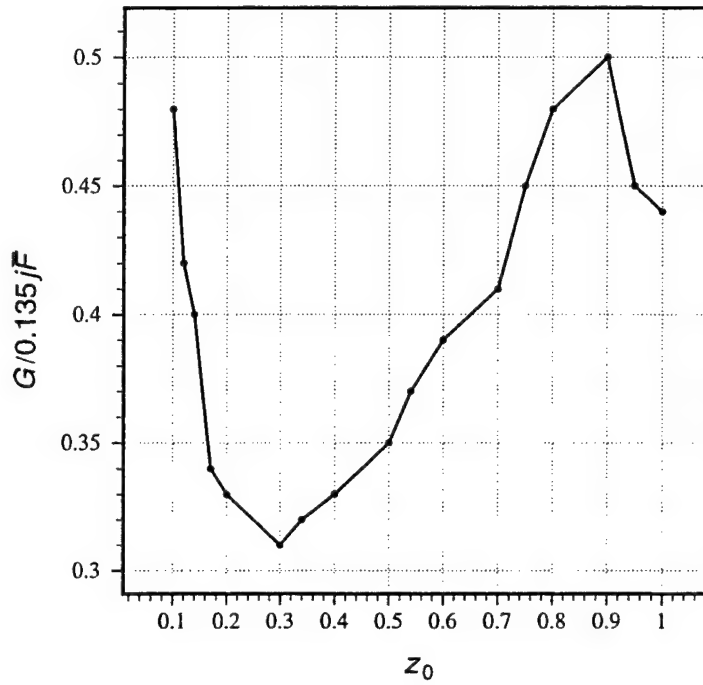


Figure 19. Plot of normalized gain versus Rayleigh length for UVFEL. Normalized gain is minimum where optical mode volume is minimum $z_0 = 0.3$.

The first feature to note in the figure is that for the UVFEL, $z_0 = 0.3$ corresponds to the minimum normalized gain because the optical mode volume is minimized. The optical mode volume must be large enough to envelope the electron beam. Decreasing the Rayleigh length below $z_0 = 0.3$ causes the mode to expand quickly away from the mode waist. This makes the mode large at the ends of the undulator, enveloping the electron beam, and increases normalized gain. Increasing the Rayleigh length from

$z_0 = 0.3$ makes the optical mode larger everywhere and increases gain until the mode gets so large, $z_0 \approx 0.9$ in this case, that electrons see weaker fields everywhere and gain is reduced. For a larger electron beam, the optimum value of z_0 for normalized gain would be larger than $z_0 \approx 0.9$.

D. ELECTRON BEAM SIZE EFFECT ON FEL GAIN

Now, given that the Rayleigh length of the optical cavity has been chosen, how is FEL gain affected by the choice of electron beam radius? Since $\omega_\beta = 1.0$ for this UVFEL, the electron's betatron trajectories are nearly straight lines, allowing them to be focussed at the undulator center using external magnets. Keeping emittance $\varepsilon = \sigma_e \sqrt{\sigma_\theta}$ fixed, decreasing the electron beam radius at the waist increases the angular spread and degrades the interaction, so there must be a limit to how small one can focus the electron beam. In all simulations, the Rayleigh length is held fixed at $z_0 = 0.5$.

Figure 20 contains the output of a simulation of the UVFEL electron beam with $\varepsilon = 0.43$. In this example, we have reduced the electron beam radius to $\sigma_e = 0.3$, which increases angular spread to $\sigma_\theta = 2.1$. We also were required to increase the current density to $j = 68$ in order to keep peak current constant. The optimum initial phase velocity is $v_0 = 4.3$ and all other parameters are the same as those in Figure 18. The phase space plot (ζ, v) is dominated by the (exponential) angular spread which indicates σ_e has been made too small. In the plot of $|a(x, \tau)|$ in the center, one can see the electrons focussed to $\sigma_e = 0.3$ at the center of the undulator, but the large angular spread carries many electrons outside the optical mode at $\tau = 0$ and $\tau = 1$. This leads to gain degradation.

Figure 21 plots the normalized gain versus electron beam radius for three different emittances: (a) $\varepsilon = 0.28$, (b) $\varepsilon = 0.43$, and (c) $\varepsilon = 0.6$. (The simulation in Figure 20 is from curve (b).) We see in the curves that decreasing the electron beam

radius from $\sigma_e = 1.0$ increases gain as more electrons are enveloped in the optical mode. The beam radius can be made too small, however, causing gain to decrease because of the increasing angular spread.

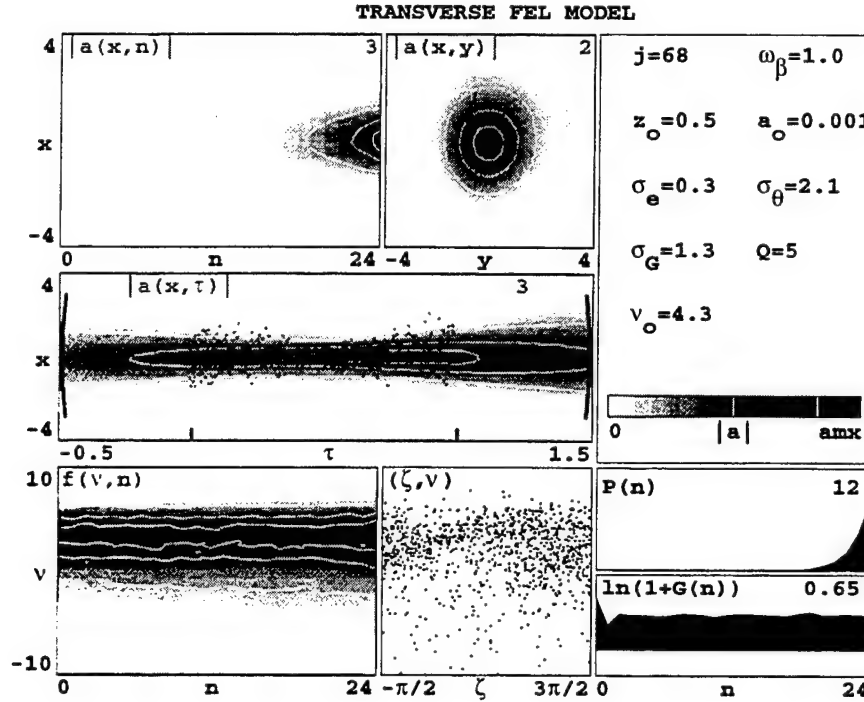


Figure 20. Transverse multimode simulation of UVFEL. Electron beam focussed at $\tau = 0.5$ but angular spread causes beam to expand outside optical mode at $\tau = 0$ and 1.

The optimum electron beam radius, and the peak gain at that radius, depend strongly on the beam emittance. With better emittance, curve (a) in Figure 21, the optimum electron beam radius is small, $\sigma_e \approx 0.3$, and peak gain is increased to $G/G_0 \approx 66\%$. Increasing emittance causes the optimum σ_e to grow larger and the maximum to become more broad until (curve (c)) the maximum gain is only weakly dependent on σ_e due to the large angular spread at any radius. This maximum gain is reduced to

$G/G_0 \approx 10\%$ at $\sigma_e \approx 0.6$. The expected emittance in the LPC UVFEL is $\varepsilon = 0.43$, curve (b). We find that the optimum electron beam radius is $\sigma_e = 0.4$, slightly smaller than that proposed.

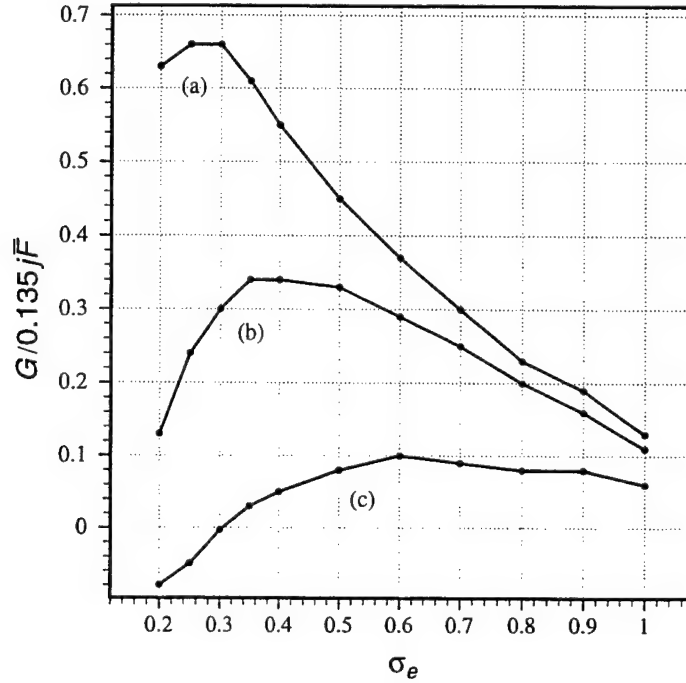


Figure 21. Plots of normalized gain versus electron beam radius for three different beam emittances: (a) $\varepsilon = 0.28$, (b) $\varepsilon = 0.43$, and (c) $\varepsilon = 0.6$.

E. CONCLUSIONS

The small characteristic mode size of the short wavelength UVFEL makes the electron beam/optical mode overlap a crucial consideration. Making the optical mode larger by either decreasing or increasing the Rayleigh length from $z_0 = 0.3$ results in increased normalized gain for a given electron beam radius. This is an important result for UVFELs. It shows that it is not necessary to have the electron beam enveloped by the optical mode throughout their interaction. With Rayleigh length fixed,

focussing the electron beam to a smaller radius will increase gain until the angular spread, which must increase as the electron beam radius is decreased, degrades the interaction and gain is reduced. With improvements in emittance, the optimum electron beam radius is smaller and the peak FEL steady-state gain is significantly increased. We find the optimum electron beam radius for the LPC UVFEL is $\sigma_e = 0.4$.

V. FELS WITH SHORT RAYLEIGH LENGTH

A. MOTIVATION

The problem of high power density on optical cavity mirrors is shared by both UVFELs and high average power FELs, the former due to its short wavelength and therefore a small diffraction rate, the latter due to extremely high (≈ 100 MW) intracavity average power. This problem could be solved by designing a long optical cavity with $z_0 \approx 0.3$, allowing space for diffraction to make the beam spot on the mirrors large. Another way to make a large spot is to use a cavity with a short ($z_0 < 0.3$) Rayleigh length. When the FEL has limited space for the optical cavity (on a ship, for example), the second method of mirror protection is particularly attractive.

As an example of the effect of the Rayleigh length on mirror power density, consider a 1 MW FEL at $\lambda = 1 \mu\text{m}$ and $Q = 5$. Simple calculations based on (60)-(63) show that the mirror power density in a 20 m long cavity with $z_0 = 0.2$ is about 1500 kW/cm^2 , which is quite large. However, if we reduce the Rayleigh length to $z_0 = 0.02$ and shorten the cavity length to 10 m, the mirror power density is reduced to about 600 kW/cm^2 . That is, we can reduce the power density on the mirrors by more than a factor of two and cut the cavity length in half by reducing the Rayleigh length by a factor of ten.

Reducing the Rayleigh length is accomplished by making the mirrors larger and their radii of curvature smaller (recall $z_0 = (2SR - S^2)^{1/2}/2L$), allowing the light to cover a large mirror while focussed to a small waist at the center of the cavity. The stability criteria for a symmetric optical cavity, $0 \leq (1 - S/R)(1 - S/R) \leq 1$, reduces to $z_0^2 \geq 0$ (Ref. 7). Therefore, as long as there is a Rayleigh length (i.e., $z_0 > 0$), the optical cavity will be stable.

In section G of Chapter II, we discussed the physics of the FEL interaction in the Gaussian optical mode. We discussed how the optical field amplitude $|a_G|$ is

greatest at $\tau = \tau_w$, which causes the phase space separatrix height to increase as $\tau : 0 \rightarrow \tau_w$ then decrease as $\tau : \tau_w \rightarrow 1$. This effect, which is proportional to $w^{-1/2}(\tau)$, complicates the phase space paths and will be exacerbated by a small Rayleigh length. The short Rayleigh length implies a small mode waist where the optical field amplitude will be much larger than at the ends of the undulator. We also saw how the phase of the Gaussian mode caused the separatrix to shift to the right as $\tau : 0 \rightarrow 1$. This requires the initial phase velocity for maximum gain to be increased from $v_0 = 2.6$, the value found when using the plane wave approximation. For $z_0 = 0.1$, the phase shift for on-axis electrons is $\Delta\phi = \phi(\tau=1) - \phi(\tau=0) = 0.9\pi$, and is smaller for off-axis electrons. With a small Rayleigh length, the wavefront curvature has to be larger in order that the light be focussed to a small waist and rapidly expand to cover the mirror.

Operating the FEL with a short Rayleigh length is not the optimum design. The previous paragraph showed how the interaction of the electrons and the light changes with Rayleigh length. This concept has never been studied before now, precisely because the design is not optimum. In this chapter we will show the consequences of using a short Rayleigh length. Since we will analyze the case $z_0 < 1$, we cannot expand (60) in $1/(z_0)$ as we did in Chapter II, but must use simulation instead. We will analyze the UVFEL of Chapter IV first, both the single pass gain $G(\tau)$ and the gain evolution $G(n)$ over several passes when in steady state. Next we present a MW-class FEL design based on the short Rayleigh length concept and simulations of same.

B. UVFEL WITH SHORT RAYLEIGH LENGTH

We first test the short Rayleigh length FEL concept by simulating the LPC UVFEL, which has parameters listed in Table 2.

1. Single Pass Gain

We study the single pass gain $G(\tau)$ in the UVFEL using transverse multimode simulations like those discussed in the previous chapter. In this case, however, since only one pass is simulated, cavity mirrors do not enter. The optical field is initialized as a Gaussian mode and can only evolve by mode distortion caused by the electron beam within the single pass. Contrast this with the multiple pass simulations presented in the previous chapter in which the optical field, entrained by the mirrors, evolves self-consistently over many passes.

Plotted in Figure 22 is the single pass gain evolution $G(\tau)$ along the undulator for four different electron beam radii: (a) $\sigma_e = 0.2$, (b) $\sigma_e = 0.45$, (c) $\sigma_e = 0.9$, and (d) $\sigma_e = 1.6$.

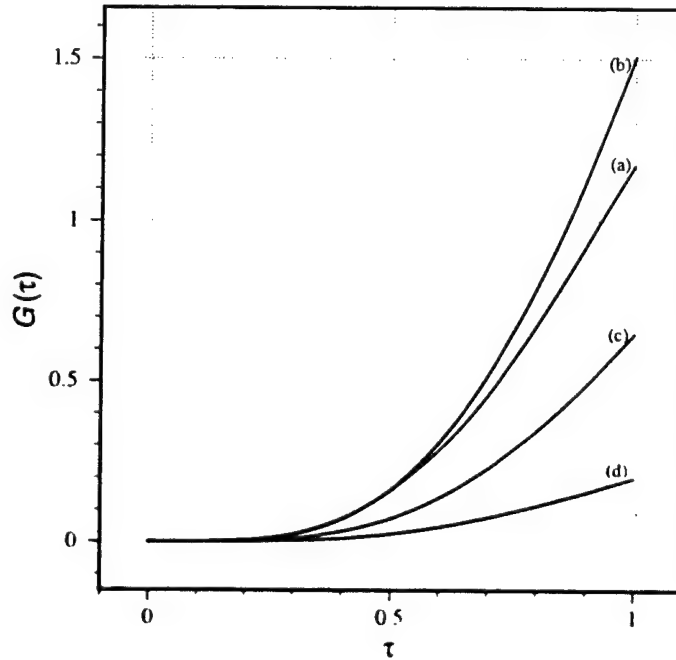


Figure 22. Gain along the undulator $G(\tau)$ for electron beams with radius (a) $\sigma_e = 0.2$, (b) $\sigma_e = 0.45$, (c) $\sigma_e = 0.9$, and (d) $\sigma_e = 1.6$. Rayleigh length is $z_0 = 0.3$, mode waist radius is $w_0 = 0.5$.

The Rayleigh length is $z_0 = 0.3$ giving a mode waist radius of $w_0 = 0.5$ (see (63)). The expected LPC UVFEL electron beam emittance $\varepsilon = 0.43$ is again. Electron beams (a) and (b) have radii smaller than the mode waist radius (i.e., $\sigma_e < w_0$) so that they are enveloped by the light for the duration of their interaction. The radii of electron beams (c) and (d) are greater than the mode waist radius. Because of this, their final gain $G(\tau=1)$ is reduced compared with beams (a) and (b). Also note that because of the large angular spread $\sigma_\theta = 4.6$ for electron beam (a), the final gain is smaller than that for beam (b). We saw in section D of the last chapter that electron beam (b) with $\sigma_e = 0.45$ and $\sigma_\theta = 0.9$ was nearly optimum for $z_0 = 0.5$ (optimum was $\sigma_e = 0.4$).

The most encouraging aspect of the plots in Figure 22 is that although the final gain differs among the four electron beams, all show nearly exponential gain (see (58)) throughout the length of the undulator. This point is better illuminated by Figure 23. In this figure we normalized the curves $G(\tau)$ from Figure 22 to their respective final gains $G(\tau=1)$ in order to compare the structure of the curves more closely. Figure 23 shows convincingly that all four of the electron beams simulated resulted in similar gain evolution throughout the length of the undulator, even those ((c) and (d)) with $\sigma_e > w_0$. We see that the gain evolution starts in all four beams after a small delay of $\tau \approx 0.2$, which is just the time it takes for the electron bunch to form (Ref. 3).

In Figure 24 we have plotted $G(\tau)$ for the same four electron beam radii, but with the Rayleigh length reduced to $z_0 = 0.1$. This means $w_0 = 0.3$ and only electron beam (a) with $\sigma_e = 0.2$ fits inside the optical mode throughout their interaction. For this reason, beam (a) has the highest final gain. Electron beam (b) has final gain reduced by nearly a factor of two over that in Figure 22 because it no longer fits inside the optical mode at the waist. Beams (c) and (d) also have final gain reduced, but only beam (d) has final gain less than 10%. This figure shows that in a single pass, where the electron beam cannot couple to higher order modes, it is more important to have the electron beam enveloped by the light than to have a small angular spread.

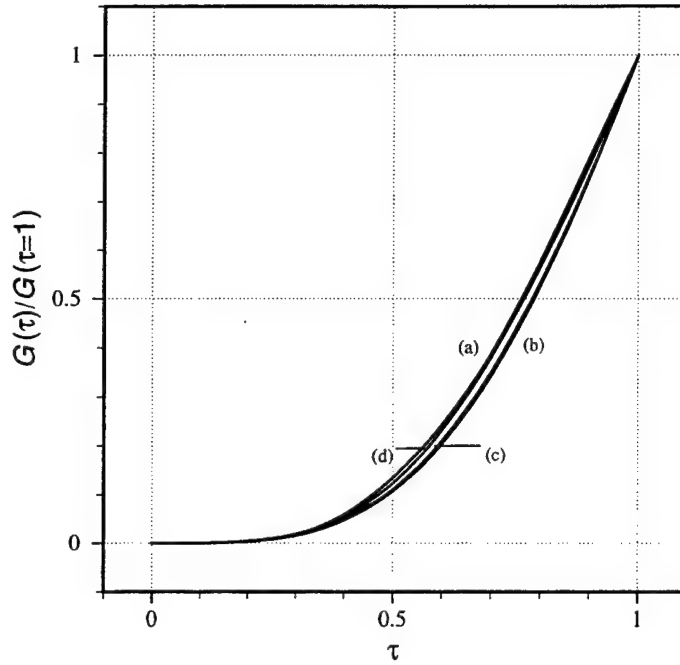


Figure 23. Normalized gain along the undulator $G(\tau)/G(\tau=1)$ for electron beams with radii (a) $\sigma_e = 0.2$, (b) $\sigma_e = 0.45$, (c) $\sigma_e = 0.9$, and (d) $\sigma_e = 1.6$. Rayleigh length and mode waist radius same as in Figure 22.

For Figure 25, the Rayleigh length was further shortened to $z_0 = 0.02$. In this case $w_0 = 0.14$ and none of the four electron beams fit inside the optical mode at the waist. The final gain for electron beams (a) and (b) is less than half their value at $z_0 = 0.1$ in Figure 24. However, there is still gain at this very short Rayleigh length, provided the electron beam is small enough. We see that $\sigma_e = 0.9$ or 1.6 , curves (c) and (d), are clearly too large. The final gain $G(\tau) > 20\%$ for the two smallest electron beams.

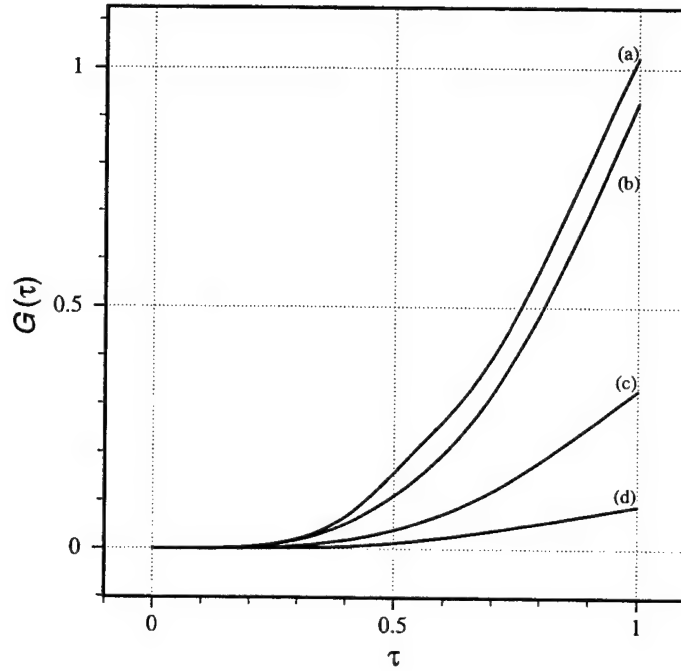


Figure 24. Gain along the undulator $G(\tau)$ for electron beams with radius (a) $\sigma_e = 0.2$, (b) $\sigma_e = 0.45$, (c) $\sigma_e = 0.9$, and (d) $\sigma_e = 1.6$. Rayleigh length is $z_0 = 0.1$, mode waist radius is $w_0 = 0.3$.

In order to better compare the evolution of gain $G(\tau)$ in Figure 25, the curves are normalized to their respective final values, as in Figure 23. The result is plotted in Figure 26. The effect of the short Rayleigh length is clear: single pass gain increases greatest where the fields $|a|$ are strongest, at the beam waist $\tau = 0.5$. The short Rayleigh length causes the fields at $\tau = 0.5$ to be much stronger than at any other position. This can be seen in electron beams (a), with $\sigma_e = 0.2$, and (d), with $\sigma_e = 1.6$. Electron beam (a) is focussed at $\tau = 0.5$; it was designed to take advantage of the field strength at the center by concentrating electron beam current there.

Electron beam (d) has a radius eight times that of beam (a). It is so large that gain is poor throughout the interaction at this Rayleigh length. What little final gain exists, however, was enhanced at $\tau \approx 0.5$ where optical fields are strongest. Indeed, we see in Figure 26 that there was net absorption for beam (d) until the field strength started to increase at $\tau \approx 0.4$. Also evident in the figure is that electron beams (b) and (c) have radii which allow gain to be distributed more uniformly. That is, they are larger than beam (a) so gain does not increase as much in the center of the undulator, but are smaller than beam (d) so that gain increases more at the ends of the undulator.

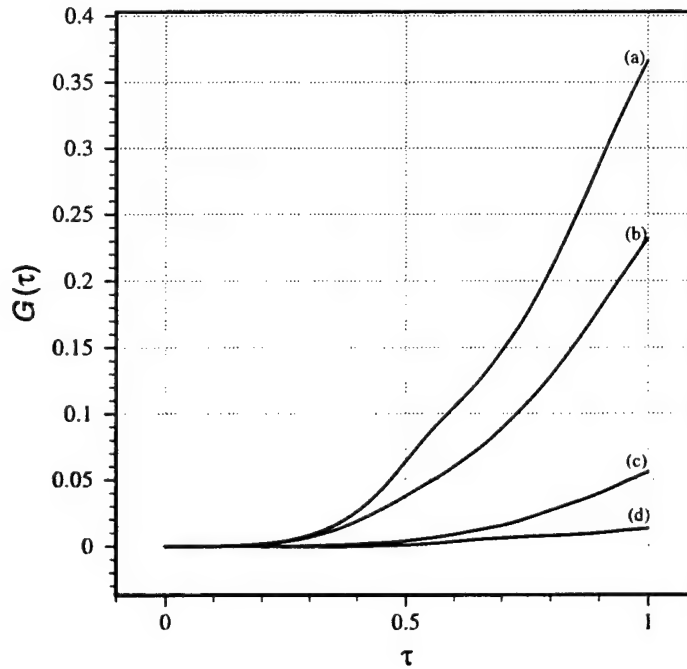


Figure 25. Gain along the undulator $G(\tau)$ for electron beams with radius (a) $\sigma_e = 0.2$, (b) $\sigma_e = 0.45$, (c) $\sigma_e = 0.9$, and (d) $\sigma_e = 1.6$. Rayleigh length is $z_0 = 0.02$, mode waist radius is $w_0 = 0.14$.

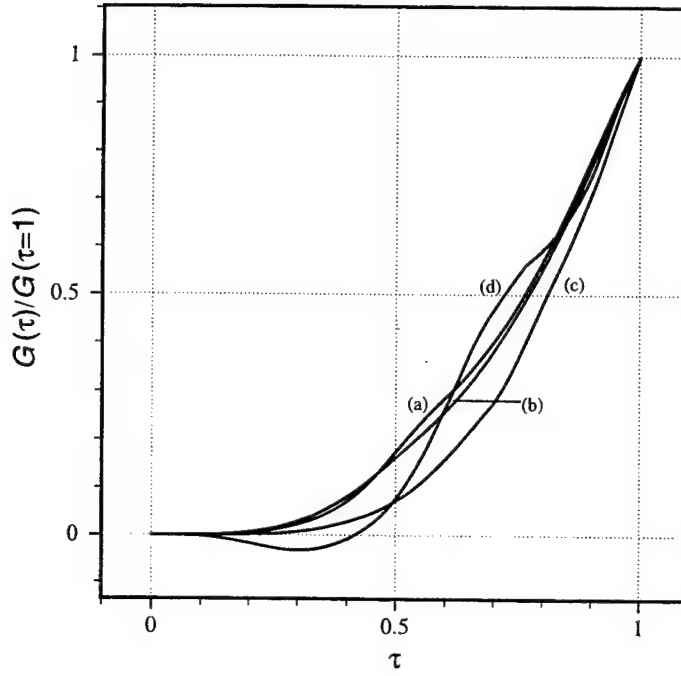


Figure 26. Normalized gain along the undulator $G(\tau)/G(\tau=1)$ for electron beams with radius (a) $\sigma_e = 0.2$, (b) $\sigma_e = 0.45$, (c) $\sigma_e = 0.9$, and (d) $\sigma_e = 1.6$. Rayleigh length and mode waist radius same as in Figure 25.

To summarize, we have found that using a very short Rayleigh length degrades gain. However, gain is still significant for the LPC UVFEL at a Rayleigh length as short as $z_0 = 0.02$. For $\sigma_e = 0.2$, the final gain is $G = 37\%$, while for $\sigma_e = 0.45$, the final gain is $G = 23\%$. The gain is only seriously degraded for electron beams with $\sigma_e = 0.9$ and $\sigma_e = 1.6$, which have radii two and four times greater than optimum, respectively. We also found that the most important region for the interaction is the center of the optical mode where the fields are strongest, even if the electron beam is much larger than the mode waist. This makes sense because it is the field amplitude

$|a|$ which drives bunching in the pendulum equation (36).

When this research was started, however, it was thought that the interaction may "turn off" at the center of the undulator, meaning that section of undulator could be replaced by a drift space, making an optical klystron, which would improve gain. The optical klystron consists of two undulator sections with a drift space at the center (Ref. 3). The first section, called the modulator, starts the electron bunching process. The drift space lets the electron momenta continue bunching in the absence of the undulator field. The second undulator section, called the radiator, causes the bunched electrons to radiate coherently. Instead of a drift space, the same effect can be obtained in a shorter distance with a dispersive section, which is just a magnet that bends the electron beam out of and back into the beam path. Slower electrons bend through a smaller radius than the more energetic electrons. Since the faster electrons travel a greater distance through the dispersive section than the slower electrons, they are bunched upon exiting. It was found, however, that we do not need to resort to exotic klystron undulator designs to get the desired gain.

2. Steady State Gain

Having studied how the gain $G(\tau)$ evolves within a single pass, we will now simulate several passes and follow the gain evolution $G(n)$. Recall that $G(n)$ follows the final gain G at $\tau = 1$ after each pass n . We use the transverse multimode, multiple pass simulations used in the previous chapter (see, for example, Figure 20) where the optical mode evolves self-consistently in the optical cavity over many passes.

The electron beams (a), (b), and (c) from the previous figures were simulated. The simulations start from weak fields $a_0 = 0.01$ and evolve until the limit of weak fields $|a| = \pi$ is reached. At this point the final gain is in steady-state, by which we mean that single pass gain $G(\tau=1)$ has nearly the same value over several passes and $G(n)$ is nearly constant. It is this steady-state value of the gain evolution $G(n)$

that is plotted versus the Rayleigh length z_0 in Figure 27.

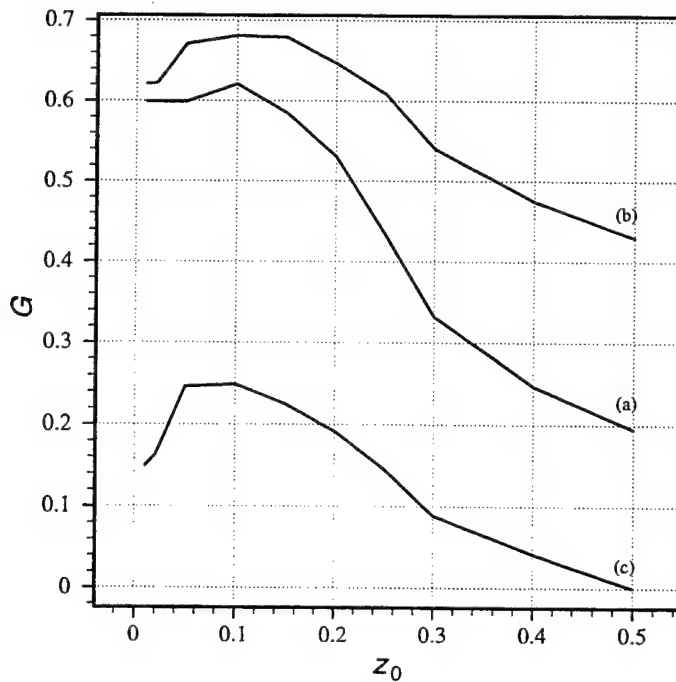


Figure 27. Steady-state gain G versus Rayleigh length for electron beams with radius (a) $\sigma_e = 0.2$, (b) $\sigma_e = 0.45$, and (c) $\sigma_e = 0.9$. We find $G \geq 60\%$ at $z_0 = 0.01$ for beams (a) and (b).

In Figure 27, we see that the nearly optimum electron beam, (b), has the highest steady-state gain at all Rayleigh lengths explored. This is in contrast with the single pass studies in which electron beam (a) had highest final gain for $z_0 < 0.3$. This electron beam is evidently more efficient in coupling to higher order modes than any of the other beams explored. Perhaps this is because of the better balance between its beam radius $\sigma_e = 0.45$ and angular spread $\sigma_\theta = 0.9$ in their contribution to the electron phase velocity spread (i.e., it is better "matched" (Ref. 3)). The maximum gain for all three of the beams occurs at Rayleigh length $z_0 = 0.1$. The most important

feature to note in the figure shows the goal of this chapter: steady-state gain is substantial even at $z_0 = 0.01$. For electron beams (a) and (b) we have $G(n) \geq 60\%$, while that for beam (c), twice the optimum radius, is still a respectable 12%.

Our conclusion is that the FEL with a short Rayleigh length may be able to operate above threshold with respectable gain while spreading the optical mode at the mirrors. The trade-off is slightly lower gain for a much shorter optical cavity with reduced power loading at the mirrors.

C. MW-CLASS FEL WITH SHORT RAYLEIGH LENGTH

Encouraged by success in modelling the UVFEL with a short Rayleigh length, the concept was used to design a MW-class FEL.

1. MW-Class FEL Design

Our goal in designing a MW-class FEL is to derive a set of parameters which will provide sufficient gain within an optical cavity of length 10 m. This length was chosen because it fits within the beam of a modern naval cruiser or destroyer.

FEL gain, discussed in section E of Chapter II, is dependent upon the dimensionless current density j (see (57) and (58)). Maximizing gain therefore requires that we maximize j . Recall that the definition of the current density in the linear undulator is

$$j = \frac{8N(e\pi K(J_0(\xi) - J_1(\xi))L)^2 \rho}{\gamma^3 mc^2} \quad (69)$$

where $\xi = K^2/(2(1 + K^2))$. Since $N = L/\lambda_0$ we can re-write (69) as

$$j = 8\pi^2 \frac{e^2}{mc^2} \left[\frac{K^2(J_0(\xi) - J_1(\xi))^2 L^3}{\lambda_0} \right] \frac{\rho}{\gamma^3} \quad (70)$$

where we have separated the parts of j according to their source. Following the fundamental constants is the undulator contribution $K^2(JJ)^2 L^3/\lambda_0$ where we have

shortened the Bessel function term in (70) to JJ . Since $K \approx 1$ in an FEL, which also fixes the Bessel terms, we are left with L and λ_0 as designable undulator parameters (Ref. 3). The electron beam contribution is ρ/γ^3 . The charge density ρ depends on the peak current \hat{I} through

$$\rho = \frac{Q}{\pi e c r_e^2 (l_e/c)} \quad (71)$$

where $Q = \hat{I} \times (l_e/c)$ is the charge per micropulse (not the cavity quality factor), r_e is the electron beam radius, and l_e is the length of the micropulse. The electron beam energy γmc^2 determines γ . Therefore we can write

$$j \propto \frac{L^3}{\lambda_0} \frac{\hat{I}}{r_e^2} \frac{1}{\gamma^3} \quad (72)$$

Recall that the emission wavelength is given by

$$\lambda = \lambda_0 \frac{(1 + K^2)}{2\gamma^2} \quad (73)$$

With $K = 1$ this becomes $\lambda = \lambda_0/\gamma^2$. This means that if we fix the wavelength λ , then λ_0 and γ are not independent. Therefore, the remaining free parameters are L , \hat{I} , r_e , λ_0 , and λ .

Our philosophy in choosing a design was to use a short undulator and use peak current to maximize j . The reasons for this are twofold. First, we are using an optical cavity 10 m long with a short Rayleigh length. The undulator has to be short in order to fit around the optical mode at the center yet not "scrape" any of the light, which would damage the magnets. Second, a short undulator means the FEL will be less susceptible to electron beam quality. This is because the gain spectrum bandwidth, which is proportional to $1/(2N)$, increases for decreasing undulator length $L = N\lambda_0$. This was discussed in section E of Chapter II and is important to the design, because as we demand more current from the accelerator we expect the beam quality to suffer.

Accordingly, we chose an undulator length $L = 1$ m. The undulator wavelength was taken to be $\lambda_0 = 4$ cm, which means $N = 25$ periods. Since the wavelength $\lambda \approx 1$ μm is fixed by the ship self-defense application, the electron beam energy is $\gamma mc^2 = \sqrt{\lambda_0/\lambda} mc^2 \approx 100$ MeV. For the remaining parameters we chose $\hat{I} = 600$ A, $r_e = 0.3$ mm, and $I_e/c = 3$ ps. This results in a total charge per micropulse $Q = \hat{I} \times (I_e/c) = 1.8$ nC. If every RF bucket of an $f = 500$ MHz accelerating field is filled by the electron injector, the duty factor is $(I_e/c) \times f = 0.0015$. The average current is then $T = 0.0015 \times \hat{I} = 0.9$ A. This results in an average electron beam power of $\bar{P}_e = T V = 0.9 \text{ A} \times 100 \times 10^6 \text{ V} = 90$ MW. An efficiency of 1.1% will be needed to extract 1 MW from this beam. These design parameters resulted in $j = 12$. All parameters are summarized in Table 3.

For electron beam quality we anticipate a trade-off between high peak current and electron beam quality. We assumed an energy spread $\Delta\gamma/\gamma = 0.5\%$ and a normalized emittance $\epsilon_N = 20\pi$ mm-mrad. These choices resulted in $\sigma_G = 1.5$ and $\epsilon = 0.27$. The dimensionless electron beam radius is $\sigma_e = 0.5$ so that the angular spread must be $\sigma_\theta = 0.3$. Noting that N is included in the numerator of (18) and (56), we see that the small values for σ_G , σ_θ , and ϵ reflect our choice of a short undulator. The beam quality parameters are also summarized in Table 3.

2. Simulations of the MW-Class FEL

Now that we have derived our parameters for the MW-class FEL, we use simulations to make sure it works. Transverse multimode, multiple pass simulations using the parameters in Table 3 were used to obtain the steady-state gain at different Rayleigh lengths. An example of these simulations at $z_0 = 0.1$ is shown in Figure 28. Steady state gain is $G(n) = 26\%$, plotted at lower right, and power $P(n)$ is increasing approximately exponentially. The optical field evolves over 20 passes yet is still weak ($|a| \ll \pi$). Bunching is not evident in the phase space plot at lower center.

Beam Energy	100 MeV
Peak Current	600 A
Average Current (@500 MHz)	0.9 A
Micropulse Length	3.0 ps
Charge per Micropulse	1.8 nC
Electron Beam Radius	0.3 mm
ϵ_N	20π mm-mrad
$\Delta\gamma/\gamma$	0.5%
Undulator Type	Linear
K	1.0
N	25
λ_0	4.0 cm
λ	$1.03 \mu\text{m}$
j	12
σ_θ	0.5
σ_θ	0.3
ϵ	0.27
σ_G	1.5

Table 3. Design parameters for a MW-class FEL suitable for ship self defense.

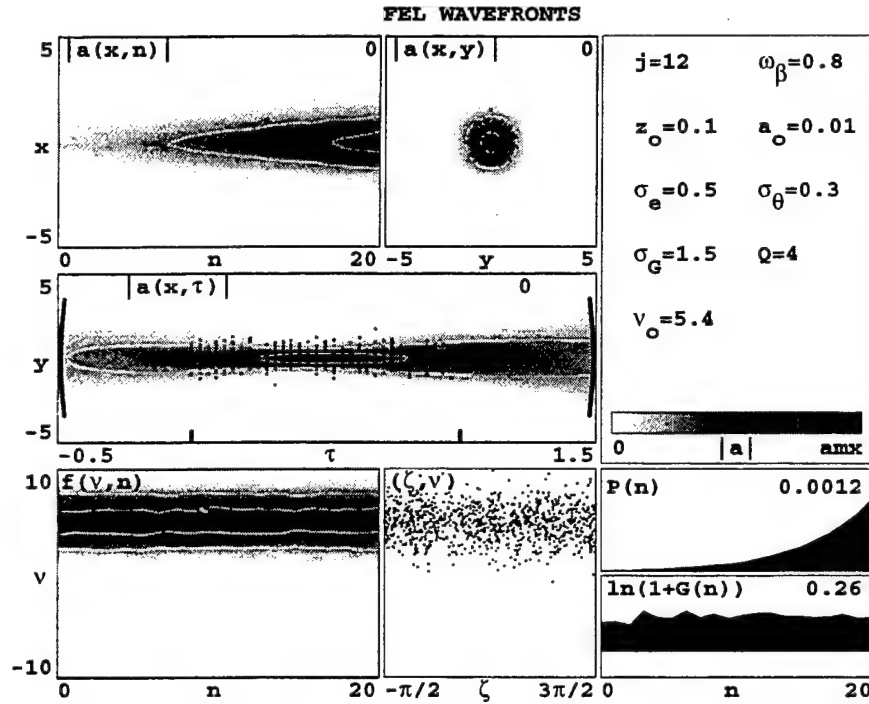


Figure 28. Transverse multimode simulation of MW-class FEL. Gain evolution $G(n)$ is in steady state.

The electron positions overlaid on the plot of the optical field amplitude between the mirrors $|a(x, \tau)|$ show that the electron beam does not expand nor focus as $\tau : 0 \rightarrow 1$. This is because the angular spread $\sigma_\theta = 0.3$ is relatively small.

Many simulations such as that in Figure 28 were used to find the effect of the Rayleigh length on steady-state gain. The result is plotted in Figure 29. As in our previous analysis of the UVFEL, maximum gain $G \approx 23\%$ for this FEL occurs at $z_0 = 0.1$ (see Figure 28). Even at the short Rayleigh length $z_0 = 0.01$, the steady-state gain $G = 18\%$ is sufficiently large that simulations indicate the design will work.

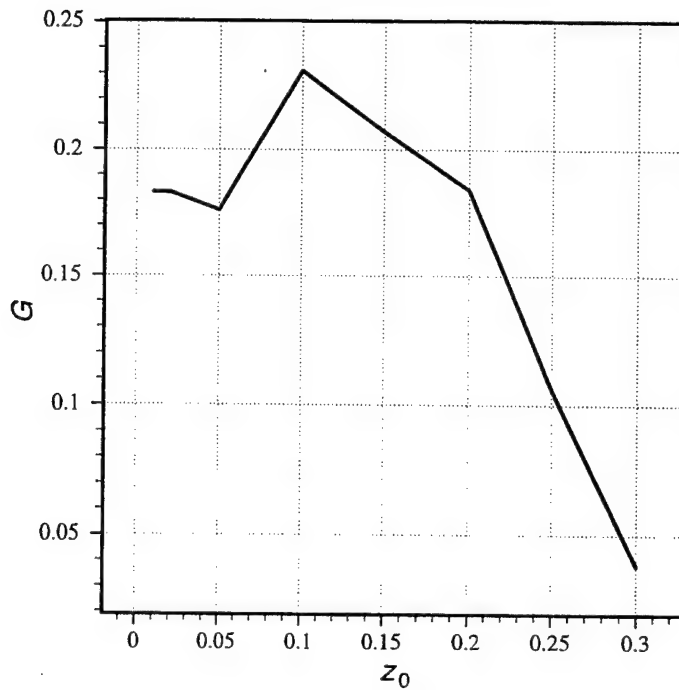


Figure 29. Steady-state gain G versus Rayleigh length z_0 for MW-class FEL. Peak gain $G \approx 23\%$ occurs at $z_0 = 0.1$. At $z_0 = 0.01$, gain is $G \approx 18\%$.

D. CONCLUSIONS

Using the LPC UVFEL parameters we showed that the concept of the short Rayleigh length FEL was viable. This had never been researched before. Based on those results, parameters for a MW-class FEL for ship self-defense were derived. This FEL design was simulated and steady-state gain was found to be $G \approx 18\%$ at $z_0 = 0.01$. It was presented at the workshop entitled "Navy MW-Class SSD FEL Concepts" at TJNAF in Newport News, Virginia, which was sponsored by the Navy High Energy Laser office at SPAWAR. It is one of only two designs that survived the

workshop.

To improve on our design, the electron beam radius should be optimized. At $\sigma_e = 0.5$, we have a small $\sigma_\theta = 0.3$ which suggests it would be advantageous to focus the electron beam further. Research should also determine what affect the Rayleigh length has on FEL efficiency. At short Rayleigh lengths, many electrons are outside the optical mode at the waist and do not participate in the interaction. Efficiency might be degraded. This is the trade-off made in choosing a short Rayleigh length over more traditional FEL designs. As we noted above, we must extract 1.1% of the electron beam energy in order to obtain 1 MW average power. Methods of improving efficiency should also be studied.

The design philosophy of using a shorter optical cavity and undulator requires high peak and average current. It shifts the technology burden from the mirrors to the accelerator, where improvements in high average current generation and acceleration must be made. Another area of accelerator physics that needs much further research is in electron beam transport. For our laser to work on a ship, we have determined that we must use an energy recovery architecture similar to that proposed for the LPC UVFEL in order to increase overall system efficiency, among other reasons (Ref. 9). This reduces the power consumption of the FEL by recirculating the electron beam through the accelerator, where it is decelerated, giving up its energy to the RF accelerator field. Recirculation requires the bending of a high current, high energy electron beam through two 180 degree bends, but, at the time of this writing, there is some question as to whether or not that is even possible.

VI. COMPTON BACKSCATTERING OF LASER LIGHT

A. PRELIMINARIES

We turn our attention now to the scattering of laser light from a high energy electron beam. The electron beam scatters high energy photons out of an incoming laser field. The process is similar to the FEL in that the incoming laser pulse can be thought of as an electromagnetic undulator, but with extremely small wavelength. The process has been described classically and with relativistic quantum mechanics, assuming a plane wave approximation for the laser field (Refs. 11, 12, 13). Recently, a correction to the plane wave approximation was attempted, using quantum electrodynamics (QED) (Ref. 14). Derlet et. al. treated the interaction of free electrons with rays of laser photons focused by a lens to the interaction region (Ref. 14). The calculation presented in this chapter is the first attempt to correct the plane wave approximation to the laser beam by treating it as a diffracting beam. That is, we assume the incoming laser beam is a fundamental Gaussian mode.

In the next section, we calculate the vector potential for the Gaussian optical mode. We approximate the Gaussian mode for long Rayleigh length in a manner similar to the analysis in section G of Chapter II. In section C, we calculate electron wavefunctions in the field represented by our vector potential. We use those wavefunctions in section D to find the distribution and rate of photon emission. This will be the first time this calculation has been done without the plane wave approximation to the laser field.

The notation used in this chapter is that of Sakurai (Ref. 15). We represent a four-vector as, for example, b_μ with $\mu = 1,2,3,4$ where

$$b_\mu = (b_1, b_2, b_3, b_4) = (\vec{b}, ib_0) \quad (74)$$

where b_1 , b_2 , and b_3 are real, corresponding to the x-, y-, and z-components of the three-vector \vec{b} , and $b_4 = ib_0$ is imaginary. We use a summation convention so that

the scalar product of two four vectors b_μ and c_μ is

$$b_\mu c_\mu = \sum_{j=1}^3 b_j c_j + b_4 c_4 = \vec{b} \cdot \vec{c} - b_0 c_0 \quad . \quad (75)$$

We will frequently shorten the notation for a scalar product from $b_\mu c_\mu$ to $b \cdot c$ for brevity. In our summation convention, Greek indices such as μ, ν , etc. run from 1 to 4 and Roman indices like i, j, k , etc. run from 1 to 3. We define the coordinate vector as

$$x_\mu = (\vec{x}, ict) \quad , \quad (76)$$

where $\vec{x} = x_1 \hat{x} + x_2 \hat{y} + x_3 \hat{z}$. The momentum four-vector is

$$p_\mu = (\vec{p}, iE/c) \quad , \quad (77)$$

where \vec{p} and E are the particle momentum and total energy, respectively. The wavevector of a photon is

$$k_\mu = (\vec{k}, i\omega/c) \quad , \quad (78)$$

where $|\vec{k}| = 2\pi/\lambda = \omega/c$ for a free photon. Variables are not made dimensionless as in the previous chapters.

We use Heaviside-Lorentz units throughout this chapter. The fields and potentials in this system are related to those in Gaussian units by the factor $1/\sqrt{4\pi}$ (Ref. 15). We will take the electron charge e to be negative $e = -|e|$.

A typical experiment, and the one we will use in order to obtain order-of-magnitude estimates to certain terms, is the proposed "laser synchrotron source" (LSS) at the Naval Research Laboratory (NRL) (Ref. 11). They have proposed using a 41 MeV electron beam with micropulse length $l_e/c = 1$ ps. The incident laser is a tabletop-terawatt (T^3) device with wavelength $\lambda = 1 \mu\text{m}$. The laser peak power is 10 TW in a 2 ps pulse, which means the energy per pulse is 20 J. The Rayleigh length is $z_0 = 7.9$ mm and the mode waist radius is $w_0 = 50 \mu\text{m}$. The energy of the emitted photons is expected to be 30 keV (x-rays). We can then calculate some typical values

for useful combinations of parameters: $eA_0/mc^2 \approx 0.4$, $\hbar\Omega/mc^2 \approx 0.06$, and $\hbar\omega/mc^2 \approx 2 \times 10^{-6}$. We define A_0 as the amplitude of the vector potential, m is the electron rest-mass, c is the speed of light in vacuum, \hbar is Planck's constant divided by 2π , Ω is the frequency of the emitted photon, and ω is the frequency of the incident laser. Note that the combination eA_0/mc^2 is analogous to the undulator parameter K in the FEL.

B. VECTOR POTENTIAL FOR LASER LIGHT

The fundamental Gaussian mode for some freely propagating scalar field U can be written:

$$U = \frac{U_0}{w(z)} e^{-\left[\frac{x^2+y^2}{w^2(z)}\right]} e^{-i(kz - \omega t + \phi)} \quad (79)$$

where U_0 is the amplitude in the center of the beam waist (Ref. 7). The mode radius is

$$w^2(z) = w_0^2 \left[1 + \left(\frac{z}{z_0} \right)^2 \right] \quad (80)$$

where w_0 is the radius of the mode waist. The mode waist radius and Rayleigh length are related by

$$z_0 = \frac{\pi w_0^2}{\lambda} \quad (81)$$

The optical phase ϕ is

$$\phi = -\tan^{-1} \left(\frac{z}{z_0} \right) + k \frac{x^2 + y^2}{2R(z)} \quad (82)$$

where $R(z) = z + z_0^2/z$ is the wavefront radius of curvature. The origin $z = 0$ is located at the mode waist.

Since our goal is to obtain a correction to the plane wave approximation for our scattering problem, we will find the form of (79) when it nearly represents a plane wave, or $z_0 \gg z$. For this case, it makes sense to expand (79) in the small parameter $(1/z_0)$ in a manner similar to the WKB approximation (Ref. 16). That is, we will expand both the amplitude and phase of (79) in $(1/z_0)$ and approximate them by keeping terms only to first order in $(1/z_0)$.

Upon expanding the amplitude we find that

$$\frac{U_0}{w(z)} e^{-\left[\frac{x^2+y^2}{w^2(z)}\right]} = \frac{U_0}{w_0} \left[1 - \frac{1}{z_0} \frac{k(x^2+y^2)}{2} \right] + O\left[\frac{1}{z_0}\right]^2 \quad (83)$$

Likewise we find for the phase

$$\phi = -\frac{z}{z_0} + O\left[\frac{1}{z_0}\right]^2 \quad (84)$$

Therefore the WKB approximation for the Gaussian mode is

$$U \approx \frac{U_0}{w_0} \left[1 - \frac{1}{z_0} \frac{k(x^2+y^2)}{2} \right] e^{-i[(k - 1/z_0)z - \omega t]} \quad (85)$$

To lowest order in $(1/z_0)$ we see that the Gaussian mode is nearly a plane wave. The only differences between (85) and a plane wave are a phase shift from $k \rightarrow k - 1/z_0$ and an amplitude correction which decreases the amplitude for electrons off-axis. To an electron in the Gaussian mode, the phase shift appears as a shift in the laser wavelength $\lambda \rightarrow \lambda/(1 - 1/kz_0) \approx \lambda(1 + 1/kz_0)$. Therefore we can anticipate that the presence of the Gaussian mode should result in a shift in wavelength of the emitted radiation as well.

For our calculation, we will take (85) to be our vector potential. Since this potential is real we will use the real part of (85) and write

$$\vec{A} = A_0 \hat{a} \left[1 - \frac{1}{z_0} \frac{k(x^2+y^2)}{2} \right] \cos\left[(k - 1/z_0)z - \omega t\right] \quad (86)$$

where A_0 , with w_0 absorbed, is the on-axis magnitude of \vec{A} and \hat{a} is the polarization unit vector. If the laser light is linearly polarized in the x-direction, as we will assume in this chapter, then $\hat{a} = (1,0,0)$. We will only consider on-axis (i.e., $x^2 + y^2 = 0$) electrons, so that we can write (86) as a four-vector as

$$A_\mu(x) = (\vec{A}(x), iA_0) = A_0 a_\mu \cos(K_v x_v) \quad (87)$$

where $a_\mu = (\hat{a}, 0)$ and

$$K_v = k_v - \delta_v = \left[0, 0, k - \frac{1}{z_0}, i\frac{\omega}{c} \right] \quad (88)$$

is the modified propagation vector. The vector $\delta_v = (0, 0, 1/z_0, 0)$ represents the phase shift discussed above. We note that $A_\mu(x)$ satisfies the Lorentz condition $\partial A_\mu / \partial x_\mu = K_\mu A_\mu = 0$ and, since in the gauge we have chosen $A_0 = 0$, the transversality condition $\nabla \cdot \vec{A} = \vec{K} \cdot \vec{A} = 0$ is also satisfied (Ref. 15).

C. DIRAC WAVEFUNCTIONS

The wavefunctions for an electron in a plane wave electromagnetic field were found in 1935 by D. M. Volkov (Ref. 17). We will follow nearly the same technique, but using our vector potential (87) for the Gaussian mode.

The Dirac equation for an electron in an electromagnetic field characterized by $A_\mu(x)$ is given by

$$\left[\gamma_v \frac{\partial}{\partial x_v} - \frac{ie}{\hbar c} \gamma_v A_v + \frac{mc}{\hbar} \right] \psi = 0 \quad (89)$$

where the 4×4 matrices γ_v are called the "gamma matrices" (Ref. 15). They are defined by the requirement that they satisfy

$$\{\gamma_\mu, \gamma_\nu\} = \gamma_\mu \gamma_\nu + \gamma_\nu \gamma_\mu = \delta_{\mu\nu} \quad (90)$$

where $\{ , \}$ is called the anti-commutator, and $\delta_{\mu\nu} = 1$ if $\mu = \nu$, 0 otherwise, is the

Kronecker delta (Ref. 15). In our notation, the gamma matrices are

$$\gamma_k = \begin{bmatrix} 0 & -i\sigma_k \\ i\sigma_k & 0 \end{bmatrix}, \gamma_4 = \begin{bmatrix} I & 0 \\ 0 & -I \end{bmatrix}, \quad (91)$$

where I is the 2×2 identity matrix and the σ_k are the Pauli spin matrices given by

$$\sigma_1 = \begin{bmatrix} 0 & 1 \\ 1 & 0 \end{bmatrix}, \sigma_2 = \begin{bmatrix} 0 & -i \\ i & 0 \end{bmatrix}, \sigma_3 = \begin{bmatrix} 1 & 0 \\ 0 & -1 \end{bmatrix}. \quad (92)$$

For example, we write γ_3 using σ_3 as

$$\gamma_3 = \begin{bmatrix} 0 & 0 & -i & 0 \\ 0 & 0 & 0 & i \\ i & 0 & 0 & 0 \\ 0 & -i & 0 & 0 \end{bmatrix}. \quad (93)$$

We also note here that the gamma matrices are Hermitian $\gamma_\mu^\dagger = \gamma_\mu$ (Ref. 15). The wavefunction in (89) is a four component object called a Dirac spinor (Ref. 15). Thus (89) is actually four coupled, first-order, differential equations for ψ .

We can obtain the quadratic form of (89) by multiplying on the left by the operator

$$\tilde{D} = \left[\gamma_\mu \frac{\partial}{\partial x_\mu} - \frac{ie}{\hbar c} \gamma_\mu A_\mu - \frac{mc}{\hbar} \right] \quad (94)$$

with the result

$$\left[\frac{\partial}{\partial x_\mu} \frac{\partial}{\partial x_\mu} - \frac{2ie}{\hbar c} A_\mu \frac{\partial}{\partial x_\mu} - \frac{ie}{\hbar c} \gamma_\mu \gamma_\nu \left(\frac{\partial A_\nu}{\partial x_\mu} \right) - \frac{e^2}{\hbar^2 c^2} A_\mu A_\mu - \frac{mc^2}{\hbar^2} \right] \psi = 0. \quad (95)$$

Substituting (87) for A_ν we find that

$$\frac{\partial A_\nu}{\partial x_\mu} = K_\mu A_\nu' \quad (96)$$

where

$$A_\nu' = -A_0 a_\nu \sin(K_\sigma x_\sigma). \quad (97)$$

We can then rewrite (95) as

$$\left[\frac{\partial}{\partial x_\mu} \frac{\partial}{\partial x_\mu} - \frac{2ie}{\hbar c} A_\mu \frac{\partial}{\partial x_\mu} - \frac{ie}{\hbar c} (\gamma \cdot K)(\gamma \cdot A') - \frac{e^2}{\hbar^2 c^2} A^2 - \frac{mc^2}{\hbar^2} \right] \psi = 0 \quad (98)$$

where we have used $\gamma \cdot K = \gamma_\mu K_\mu$, etc.

Following Volkov, we seek a solution to (98) of the form

$$\psi = e^{i \frac{p \cdot x}{\hbar}} \phi(k \cdot x) \quad (99)$$

where $\phi(k \cdot x)$ is a Dirac spinor. We subject our solution to the initial condition $\psi \rightarrow u^{(s)}(\vec{p}) \exp(ip \cdot x / \hbar)$ as $x \rightarrow -\infty$ for an electron coming into the interaction region. We recognize $u^{(s)}(\vec{p})$ as the free electron spinor, $s = 1, 2$ is the electron spin index and \vec{p} is the electron momentum (Ref. 15). The initial condition means physically that prior to entering the interaction region the electron is free. Substituting (99) into (98), we find that $\phi(k \cdot x)$ must satisfy

$$\frac{2i}{\hbar} p \cdot k \phi'(\xi) + \left[\frac{2e}{\hbar^2 c} A \cdot p - \frac{ie}{\hbar c} (\gamma \cdot K)(\gamma \cdot A') - \frac{e^2}{\hbar^2 c^2} A^2 \right] \phi(\xi) = 0 \quad (100)$$

where $\xi = k \cdot x$, $\phi' = \partial \phi / \partial \xi$, and we have used $k^2 = 0$. This first-order differential equation has the solution

$$\phi(\xi) = \exp \left[\frac{e}{2c} \int_{-\infty}^{\xi} \frac{(\gamma \cdot K)(\gamma \cdot A')}{p \cdot k} d\xi' + \frac{ie}{\hbar c} \int_{-\infty}^{\xi} \left[\frac{A \cdot p}{p \cdot k} - \frac{e}{2c} \frac{A^2}{p \cdot k} \right] d\xi' \right] u \quad (101)$$

where u is a Dirac spinor. Invoking the initial condition, we find that $\phi \rightarrow u$ as $\xi \rightarrow -\infty$ so that $\psi \rightarrow u \exp(ip \cdot x / \hbar)$. Therefore, we will take u to be the free electron spinor $u = \sqrt{mc^2/EV} u^{(s)}(\vec{p})$ where V is the normalization volume and E is the total energy (Ref. 15). The wavefunction for the incoming electron is

$$\begin{aligned} \psi_{in} = & \exp \left[\frac{e}{2c} \int_{-\infty}^{\xi} \frac{(\gamma \cdot K)(\gamma \cdot A')}{p \cdot k} d\xi' + \frac{ie}{\hbar c} \int_{-\infty}^{\xi} \left[\frac{A \cdot p}{p \cdot k} - \frac{e}{2c} \frac{A^2}{p \cdot k} \right] d\xi' \right] \\ & \times \left[\frac{mc^2}{EV} \right]^{1/2} u^{(s)}(\vec{p}) e^{i \frac{p \cdot x}{\hbar}} . \end{aligned} \quad (102)$$

We can show that this wavefunction satisfies the Dirac equation (89), as it must, in addition to being a solution to (95) (Ref. 12). Let D represent the Dirac equation operator such that the Dirac equation is $D\psi = 0$. Then $\tilde{D}D\psi = 0$ represents (95). (Recall that \tilde{D} was defined in (94).) Let $\chi = D\psi_{in}$ where ψ_{in} is given by (102). Now since ψ_{in} reduces to the free electron spinor, which satisfies the Dirac equation, as $x \rightarrow -\infty$, we know that $\chi \rightarrow 0$ as $x \rightarrow -\infty$. Since $\tilde{D}D\psi_{in} = \tilde{D}\chi = 0$ and $\chi \rightarrow 0$ as $x_0 \rightarrow -\infty$, we must have $\chi = 0$ identically. Therefore, $D\psi_{in} = 0$ and ψ_{in} satisfies the Dirac equation (89).

To find the wavefunction for the outgoing electron, we must solve (95) subject to $\psi \rightarrow u^{(s')}(\vec{p}') \exp(ip' \cdot x / \hbar)$ as $x_0 \rightarrow \infty$. The result is

$$\begin{aligned} \psi_{out} = \exp \left[-\frac{e}{2c} \int_{\xi}^{\infty} \frac{(\gamma \cdot K)(\gamma \cdot A')}{p' \cdot k} d\xi' - \frac{ie}{\hbar c} \int_{\xi}^{\infty} \left[\frac{A \cdot p'}{p' \cdot k} - \frac{e}{2c} \frac{A^2}{p' \cdot k} \right] d\xi' \right] \\ \times \left[\frac{mc^2}{EV} \right]^{1/2} u^{(s')}(\vec{p}') e^{i \frac{p' \cdot x}{\hbar}} \end{aligned} \quad (103)$$

where the outgoing electron is specified by spin index s' , momentum p' , and energy E .

We now turn to the task of evaluating the integrals buried inside the wavefunctions (102) and (103). The vector potential in the integrals of (102) and (103) is a function of $K \cdot x = k \cdot x - \delta \cdot x$ while the variable of integration is $k \cdot x$. Let $\chi = K \cdot x = \xi - \delta \cdot x$ and perform a change of variables to χ . We find

$$d\xi = \left[1 + \frac{\partial}{\partial \chi} (\delta \cdot x) \right] d\chi = \left[1 + \frac{1}{kz_0} + O\left(\frac{1}{z_0}\right)^2 \right] d\chi \quad (104)$$

and we approximate the differential $d\xi$ with the first two terms. Making the change of variables in (102) we write

$$\begin{aligned} \psi_{in} = \exp \left[\left(1 + \frac{1}{kz_0} \right) \left[\frac{e}{2c} \int_{-\infty}^{\chi+\delta \cdot x} \frac{(\gamma \cdot K)(\gamma \cdot A'(\chi'))}{p \cdot k} d\chi' \right. \right. \\ \left. \left. + \frac{ie}{\hbar c} \int_{-\infty}^{\chi+\delta \cdot x} \left[\frac{A(\chi') \cdot p}{p \cdot k} - \frac{e}{2c} \frac{A^2(\chi')}{p \cdot k} \right] d\chi' \right] \right] \left(\frac{mc^2}{EV} \right)^{1/2} u^{(s)}(\vec{p}) e^{i \frac{p \cdot x}{\hbar}} . \end{aligned} \quad (105)$$

The correction term $(1 + 1/kz_0)$ which we discussed in the last section appears explicitly in the electron wavefunction. Substituting the vector potential (87) into (105) and performing the integrations we arrive at

$$\begin{aligned} \psi_{in} = \exp \left\{ \left(1 + \frac{1}{kz_0} \right) \left[\frac{e}{2c} \left(\frac{(\gamma \cdot K)(\gamma \cdot a)}{p \cdot k} \right) \cos(k \cdot x) \right. \right. \\ \left. \left. + \frac{ie}{\hbar c} \left[A_0 \left(\frac{a \cdot p}{p \cdot k} \right) \sin(k \cdot x) - \frac{eA_0^2}{2c} \left(\frac{1}{p \cdot k} \right) \left(\frac{k \cdot x}{2} + \frac{\sin(2k \cdot x)}{4} \right) \right] \right] \right\} \\ \times \left(\frac{mc^2}{EV} \right)^{1/2} u^{(s)}(\vec{p}) e^{i \frac{p \cdot x}{\hbar}} \end{aligned} \quad (106)$$

where we have dropped divergent sine terms in the phase of the wavefunction. The divergence of these terms is not physical, arising because our vector potential describes a laser beam undamped at $-\infty$ while we require that the fields associated with A_μ vanish at $-\infty$. Likewise, we perform the change of variables (104) and the integration in (103) with the result

$$\begin{aligned}
\psi_{out} = \exp & \left\{ \left[1 + \frac{1}{kz_0} \right] \left[\left[\frac{e}{2c} \right] \left[\frac{(\gamma \cdot K)(\gamma \cdot a)}{p' \cdot k} \right] \cos(k \cdot x) \right. \right. \\
& + \left. \frac{ie}{\hbar c} \left[A_0 \left[\frac{a \cdot p'}{p' \cdot k} \right] \sin(k \cdot x) - \frac{eA_0^2}{2c} \left[\frac{1}{p' \cdot k} \right] \left[\frac{k \cdot x}{2} + \frac{\sin(2k \cdot x)}{4} \right] \right] \right\} \\
& \times \left[\frac{mc^2}{EV} \right]^{1/2} u^{(s')}(\vec{p}') e^{i \frac{p' \cdot x}{\hbar}}
\end{aligned} \tag{107}$$

for the outgoing electron.

We now have the wavefunctions for the electron entering the interaction region (106) and for the electron leaving the interaction region (107). The difference between these wavefunctions and the Volkov wavefunctions is in the factor $(1 + 1/(kz_0))$ in the exponential and the presence of the modified propagation vector K_μ instead of k_μ (Refs. 12, 13, 17). As we expected, by choosing a Gaussian mode which differed only slightly from the plane wave (i.e., $z_0 \gg z$), our wavefunctions differ only slightly from the Volkov wavefunctions. We now use these wavefunctions to find the effect of the Gaussian mode on photon emission.

D. PHOTON EMISSION

For the calculation of the differential transition rate in this section we will use "natural units" $\hbar = c = 1$. This aids the calculation in that we will not have to keep track of all of these fundamental constants. We will write our results at the end of the section with these constants included so that real numbers may be calculated.

The amplitude for an electron transition from ψ_{in} to ψ_{out} with the emission of a photon is

$$M = -\int j_\mu A_\mu^{(int)} d^4x \tag{108}$$

where the integral is over all space and time (Ref. 15). The interaction vector potential $A_\mu^{(int)}$ for the emission of a single photon is

$$A_\mu^{(int)} = \sqrt{\frac{1}{2\Omega V}} \epsilon_\mu^{(r)} e^{-i(l \cdot x)} \quad (109)$$

where l_μ is the emitted photon propagation vector and $\epsilon_\mu^{(r)}$, $r = 1, 2$, is its polarization vector (Ref. 15). These are given by

$$l_\mu = (\vec{l}, i\Omega) \quad (110)$$

where Ω is the frequency of the emitted photon and

$$\epsilon_\mu^{(r)} = (\hat{\epsilon}_\mu^{(r)}, 0) \quad (111)$$

is chosen such that $(\hat{\epsilon}^{(1)}, \hat{\epsilon}^{(2)}, \vec{l}/|\vec{l}|)$ form a right-handed coordinate system in three dimensional space (Ref. 15). The interaction of the electrons with this unquantized vector potential (109) for photon emission is rigorously equivalent to their interaction with the quantized electromagnetic field (Ref. 15). The transition current j_μ is

$$j_\mu(x) = ie \bar{\Psi}_{out} \gamma_\mu \Psi_{in} \quad (112)$$

where γ_μ is given by (91) and $\bar{\Psi} = \Psi^\dagger \gamma_4$ is the adjoint spinor (Ref. 15). Substituting (109) into (108) we can write the transition amplitude as

$$M = -\sqrt{\frac{1}{2\Omega V}} \int j_\mu(x) \epsilon_\mu^{(r)} e^{-i(l \cdot x)} d^4x \quad (113)$$

To find the transition current $j_\mu(x)$ we substitute the wavefunctions (106) and the adjoint of (107) (recall $\hbar = c = 1$) into (112) with the result

$$j_\mu(x) = ie\sqrt{\frac{m}{EV}}\sqrt{\frac{m}{EV}}e^{i(p-p')\cdot x} \quad (114)$$

$$\begin{aligned} & \times \left\{ \bar{u}^{(s')}(\vec{p}') \exp \left[\frac{eA_0}{2} \left(1 + \frac{1}{kz_0} \right) \left(\frac{\gamma \cdot a \gamma \cdot K}{p' \cdot k} \right) \cos k \cdot x \right] \gamma_\mu \right. \\ & \times \exp \left[\frac{eA_0}{2} \left(1 + \frac{1}{kz_0} \right) \left(\frac{\gamma \cdot K \gamma \cdot a}{p \cdot k} \right) \cos k \cdot x \right] u^{(s)}(\vec{p}) \left. \right\} \\ & \times \exp \left[i\alpha \sin k \cdot x - i\beta(2k \cdot x + \sin 2k \cdot x) \right] \end{aligned}$$

where we have defined

$$\alpha = eA_0 \left[1 + \frac{1}{kz_0} \right] \left[\frac{a \cdot p}{p \cdot k} - \frac{a \cdot p'}{p' \cdot k} \right] \quad (115)$$

and

$$\beta = \frac{e^2 A_0^2}{8} \left[1 + \frac{1}{kz_0} \right] \left[\frac{1}{p \cdot k} - \frac{1}{p' \cdot k} \right] . \quad (116)$$

We will now simplify and make some approximations to (114). Using the property of gamma matrices that

$$(\gamma \cdot b)(\gamma \cdot b) = b^2 , \quad (117)$$

which is a special case of

$$(\gamma \cdot b)(\gamma \cdot c) = b \cdot c - (\gamma \cdot c)(\gamma \cdot b) , \quad (118)$$

we can expand the real exponentials in (114). The expansion yields

$$\exp\left[\frac{eA_0}{2}\left(1 + \frac{1}{kz_0}\right)\frac{(\gamma \cdot a)(\gamma \cdot K)}{p' \cdot k} \cos k \cdot z\right] =$$

$$1 + \frac{eA_0}{2}\left(1 + \frac{1}{kz_0}\right)\frac{(\gamma \cdot a)(\gamma \cdot K)}{p' \cdot k} \cos k \cdot x$$
(119)

where we have ignored terms of higher-order in $(1/z_0)$ and those proportional to $(eA_0/(2p'))^2(1/kz_0) \approx 10^{-10}$ and higher. We used the NRL parameters discussed in section A to calculate these estimates. We can simplify (114) by writing the complex exponential involving α and β in terms of Bessel functions using the generating function

$$e^{ix \sin \theta} = \sum_{m=-\infty}^{\infty} e^{im\theta} J_m(x) \quad (120)$$

where m is an integer (Ref. 18). We find

$$\exp[i\alpha \sin k \cdot x - i\beta \sin 2k \cdot x] = \sum_{m=-\infty}^{\infty} \sum_{n=-\infty}^{\infty} e^{i(m-2n)k \cdot x} J_m(\alpha) J_n(\beta) \quad (121)$$

$$= \sum_{q=-\infty}^{\infty} e^{i2qk \cdot x} \sum_{n=-\infty}^{\infty} J_{2(q+n)}(\alpha) J_n(\beta)$$

$$= \sum_{q=-\infty}^{\infty} e^{i2qk \cdot x} G_0(q, \alpha, \beta)$$

where $G_0(q, \alpha, \beta) = \sum_{n=-\infty}^{\infty} J_{2(q+n)}(\alpha) J_n(\beta)$. This term (121) leads to emission into harmonics where q is the harmonic number. We then incorporate these simplifications and re-write (114) as

$$j_\mu(x) = ie \sqrt{\frac{m}{EV}} \sqrt{\frac{m}{EV}} \sum_{q=-\infty}^{\infty} G_0(q, \alpha, \beta) e^{i(p-p'+2(q-\beta)k) \cdot x} \quad (122)$$

$$\times u^{(s)}(p') \left[1 + \frac{eA_0}{2} \left(1 + \frac{1}{kz_0} \right) \frac{\gamma \cdot a \gamma \cdot K}{p' \cdot k} \cos k \cdot x \right] \gamma_\mu$$

$$\times \left[1 + \frac{eA_0}{2} \left(1 + \frac{1}{kz_0} \right) \frac{\gamma \cdot K \gamma \cdot a}{p \cdot k} \cos k \cdot x \right] u^{(s)}(p) .$$

Substituting (122) into (113) to get the transition amplitude we find that we can write

$$M = M_0 + M_1 + M_2 \quad (123)$$

where

$$M_0 = -ie \sqrt{\frac{\hbar}{2\Omega V}} \sqrt{\frac{m}{EV}} \sqrt{\frac{m}{EV}} \sum_{q=-\infty}^{\infty} \int d^4x e^{-i(l-p+p'-2(q-\beta)k) \cdot x} \times u^{(s')}(\vec{p}') \gamma \cdot \epsilon^{(r)} u^{(s)}(\vec{p}) G_0(q, \alpha, \beta) \quad (124)$$

and

$$M_1 = -ie \sqrt{\frac{1}{2\Omega V}} \sqrt{\frac{m}{EV}} \sqrt{\frac{m}{EV}} \sum_{q=-\infty}^{\infty} \int d^4x e^{-i(l-p+p'-2(q-\beta)k) \cdot x} \times \frac{eA_0}{2} \left[1 + \frac{1}{kz_0} \right] u^{(s')}(\vec{p}') \left[\frac{\gamma \cdot a \gamma \cdot K \gamma \cdot \epsilon^{(r)}}{p' \cdot k} + \frac{\gamma \cdot \epsilon^{(r)} \gamma \cdot K \gamma \cdot a}{p \cdot k} \right] u^{(s)}(\vec{p}) \times G_0(q, \alpha, \beta) \cos k \cdot x \quad (125)$$

and $M_2 \propto (eA_0/m)^2 (\omega/m) \approx 10^{-7}$ can be neglected in comparison with M_0 . For the transition probability, we need to find $|M|^2 = |M_0|^2 + M_0^\dagger M_1 + M_0 M_1^\dagger + |M_1|^2$. The term $|M_1|^2 \propto (eA_0/m)^2 (\omega/m)^2 \approx 10^{-13}$ and can be safely ignored in comparison with $|M_0|^2$. Also, the cross-terms like $M_0^\dagger M_1 \propto (eA_0/m) (\omega/m) \approx 10^{-6}$, so that ignoring these terms when calculating $|M|^2$ will introduce an error of one part in 10^6 . Therefore we will use $|M|^2 \approx |M_0|^2$. Carrying out the trivial integration in (124) we find

$$|M_q|^2 = e^2 (2\pi)^8 \frac{1}{2\Omega V} \frac{m}{EV} \frac{m}{EV} |\delta^{(4)}(l-p+p'-2(q-\beta)k)|^2 \times |u^{(s')}(\vec{p}') \gamma \cdot \epsilon^{(r)} u^{(s)}(\vec{p})|^2 G_0^2(q, \alpha, \beta) \quad (126)$$

for the specific harmonic number q . We note that in order for the energy-momentum conservation relationship inside the δ -function to be true, q must be a positive integer.

The total transition probability is then $\sum_{q=1}^{\infty} |M_q|^2$. We write the square of the delta function as

$$|\delta^{(4)}(l-p+p'-2(q-\beta)k)|^2 = \frac{VT}{(2\pi)^4} \delta^{(4)}(l-p+p'-(q-2\beta)k) \quad (127)$$

where V and T are the interaction volume and time (Ref. 15).

The transition rate per unit time $|M_q|^2/T$ into a group of final electron and photon states is

$$dW_q = \frac{|M_q|^2}{T} \left[\frac{V d^3|\vec{p}'|}{(2\pi)^3} \right] \left[\frac{V d^3|\vec{l}|}{(2\pi)^3} \right] \quad (128)$$

where the two differential factors are the density of final states for the outgoing electron and emitted photon and integration over \vec{p}' and \vec{l} is implied (Ref. 19). Substituting (126) into (128) we find

$$dW_q = \frac{e^2}{(2\pi)^2} \frac{1}{2\Omega} \frac{m}{E} \frac{m}{E'} \delta^{(4)}(l-p+p'-(q-2\beta)k) |U^{(s')}(\vec{p}') \gamma \cdot \epsilon^{(r)} U^{(s)}(\vec{p})|^2 \quad (129)$$

$$\times G_0^2(q, \alpha, \beta) d^3|\vec{p}'| d^3|\vec{l}|$$

and we see that the dependence on V and T disappears, as it should. Performing the integrations we are left with

$$\frac{dW_q}{d\Sigma} = \frac{e^2}{(2\pi)^2} \frac{\Omega}{2} \frac{m}{E} \frac{m}{E'} \left[\frac{\partial}{\partial \Omega} (\Omega + E' + 2\beta\omega) \right]^{-1} |U^{(s')}(\vec{p}') \gamma \cdot \epsilon^{(r)} U^{(s)}(\vec{p})|^2 \quad (130)$$

$$\times G_0^2(q, \alpha, \beta)$$

which is the differential transition rate for a photon emitted into the solid angle element $d\Sigma$. The derivative term in brackets is the result of the $|\vec{l}| = \Omega$ integration over a delta function whose argument is itself a function of the photon emission frequency Ω (Ref. 19). We note that (130) is subject to the energy-momentum conservation relations

$$p'_\mu = p_\mu + 2(q - \beta)k_\mu - l_\mu \quad (131)$$

which implies

$$\vec{p}' = \vec{p} + 2(q - \beta)\vec{k} - \vec{l} \quad (132)$$

$$E' = E + 2(q - \beta)\omega - \Omega \quad (133)$$

and because

$$E' = (|\vec{p}'|^2 + m^2)^{1/2} \quad (134)$$

E' itself depends on Ω through (132). Equation (131) is Lorentz invariant; it holds in all inertial reference frames.

The remainder of the calculation will be easiest if we use the "laboratory frame" defined, for historical reasons, as that in which the incoming electron is at rest. This implies that $\vec{p} = 0$ and $p_\mu = (0, im)$. Thus (132) becomes

$$\vec{p}' = 2(q - \beta)\vec{k} - \vec{l} \quad (135)$$

and the outgoing electron energy is, substituting (135) into (134),

$$E' = \left[4(q - \beta)^2\omega^2 + \Omega^2 - 4(q - \beta)\omega\Omega\cos\theta + m^2 \right]^{1/2} \quad (136)$$

where θ is the angle between \vec{k} and \vec{l} . Since we know $\vec{k} = (2\pi/\lambda)\hat{z}$, θ measures the angle of photon emission from the z-axis, as shown in Figure 30.

We can find the frequency Ω of the emitted photon by squaring both sides of (132) to obtain the invariant equation

$$2(q - \beta)p \cdot k - l \cdot p - 2(q - \beta)l \cdot k = 0 \quad (137)$$

where we have used $p^2 - p'^2 = 0$. Computing the scalar products in (137) in the lab frame and solving for Ω we find

$$\Omega = \frac{2(q - \beta)\omega}{1 + 2(q - \beta)\frac{\omega}{m}(1 - \cos\theta)} \quad (138)$$

This frequency is corrected in that it is slightly decreased from the plane wave

approximation, since $\beta \propto A_0^2(1 + 1/(kz_0))$. The frequency is shifted by the factor $(1 + 1/kz_0)$, which is the shift in frequency of the incident laser light as seen by the incoming electron, as discussed in section A.

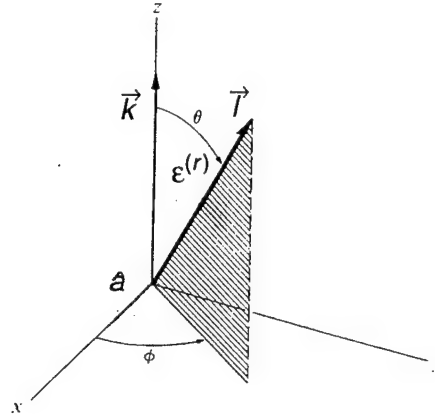


Figure 30. Coordinate system showing kinematics of Compton scattering (after Ref. 15).

To compute α , (115), and β , (116), we compute the scalar products:

$$p \cdot k = -m\omega \quad , \quad (139)$$

$$p' \cdot k = \vec{p}' \cdot \vec{k} - E'\omega = \omega[2(q - \beta)\omega - \Omega \cos\theta] \quad , \quad (140)$$

$$a \cdot p = 0 \quad , \quad (141)$$

and

$$a \cdot p' = \vec{a} \cdot \vec{p}' = -\omega \sin\theta \cos\phi \quad . \quad (142)$$

Substituting these into (115) and (116) we arrive at

$$\alpha = eA_0 \left[1 + \frac{1}{kz_0} \right] \frac{\sin\theta \cos\phi}{\Omega(1 - \cos\theta) - m} \quad (143)$$

where ϕ is the angle between the projection of \vec{T} onto the x-y plane and the x-axis (see

Figure 30) and

$$\beta = \frac{e^2 A_0^2}{8\omega m} \left[1 + \frac{1}{kz_0} \right] \frac{\Omega(1 - \cos\theta)}{m - \Omega(1 - \cos\theta)} \quad (144)$$

and we see the dependence of β on the emitted photon frequency Ω .

We are now in position to calculate the derivative in (130). Using (136), (138), (144) and a lot of algebra we find that

$$\frac{\partial}{\partial \Omega} (\Omega + E' + 2\beta\omega) = \frac{2q\omega m}{E'\Omega} \quad (145)$$

We recognize this term, apart from the harmonic number q , from ordinary Compton scattering (see Ref. 15, page 228).

We can now write (130) in the lab frame as

$$\frac{dW_q}{d\Sigma} = \alpha \frac{\Omega}{4\pi} \left[\frac{\Omega}{q\omega} \right] |U^{(s')}(\vec{p}') \gamma \cdot \epsilon^{(r)} U^{(s)}(\vec{p})|^2 G_0^2(q, \alpha, \beta) \quad (146)$$

where $\alpha \approx 1/137$ is the fine structure constant (Ref. 15). The last thing we need to do is calculate the term $|U \gamma \cdot \epsilon U|^2$. Since the spin of the initial and final electrons is unobserved, we average over the initial spins and sum over the final spins with the result

$$\frac{1}{2} \sum_{s, s'} |U^{(s')}(\vec{p}') \gamma \cdot \epsilon^{(r)} U^{(s)}(\vec{p})|^2 = \frac{E' - m}{2m} \quad (147)$$

where we have used "Casimir's trick" in order to compute the spin sum using the trace method (refer to pages 191-192 in Ref. 15).

Our final result, for the emission rate of a photon of frequency Ω into the solid angle element $d\Sigma$ around θ , including \hbar and c , is

$$\frac{dW_q}{d\Sigma} = \alpha \frac{\Omega}{4\pi} \left[\frac{\Omega}{q\omega} \right] \left[\frac{E' - mc^2}{2mc^2} \right] G_0^2(q, \alpha, \beta) \quad (148)$$

Recall that for the entire spectrum, (148) must be summed over the harmonic number

q . We summarize our other results, including \hbar and c , as well:

$$\Omega = \frac{2(q - \beta)\omega}{1 + 2(q - \beta)\frac{\hbar\omega}{mc^2}(1 - \cos\theta)} \quad (149)$$

$$E' = \left[4(q - \beta)^2\hbar^2\omega^2 + \hbar^2\Omega^2 - 4\hbar^2(q - \beta)\omega\Omega\cos\theta + m^2c^4 \right]^{1/2} \quad (150)$$

$$\eta = eA_0 \left[1 + \frac{1}{kz_0} \right] \frac{\sin\theta\cos\phi}{\hbar\Omega(1 - \cos\theta) - mc^2} \quad (151)$$

$$\beta = \frac{q\frac{e^2A_0^2}{4mc^2} \left[1 + \frac{1}{kz_0} \right] (1 - \cos\theta)}{mc^2 + \frac{e^2A_0^2}{4mc^2} \left[1 + \frac{1}{kz_0} \right] (1 - \cos\theta)} \quad (152)$$

and we have used (138) to write β in terms of the scattering angle and laser frequency ω . Our Gaussian mode correction $(1 + 1/kz_0)$ is evident in each of these equations either explicitly or through β . We see that both the angular distribution (through G_0 in (148)) and frequency (149) can be altered by merely focussing the laser beam.

If we specialize now to backscattering, $\theta = \pi$, we see that $\eta \rightarrow 0$ and the Bessel function sum collapses:

$$G_0(q, \eta=0, \beta) = \sum_{n=-\infty}^{\infty} J_{2(n+q)}(0) J_n(\beta) = (-1)^q J_q(\beta) \quad (153)$$

since only $J_0(0) > 0$ implies $n = -q$ and we have used the identity (Ref. 20)

$$J_{-n}(x) = (-1)^n J_n(x) \quad (154)$$

Therefore we find that the transition rate becomes

$$\frac{dW_q}{d\Sigma} = \alpha \frac{\Omega}{4\pi} \left[\frac{\Omega}{q\omega} \right] \left[\frac{E' - mc^2}{2mc^2} \right] J_q^2(\beta) \quad (155)$$

The argument of the Bessel function becomes

$$\beta = \frac{q \frac{eA_0^2}{2mc^2} \left[1 + 1/kz_0 \right]}{mc^2 + \frac{e^2 A_0^2}{2mc^2} \left[1 + 1/kz_0 \right]} \quad (156)$$

and the emitted wavelength is

$$\Omega = \frac{2(q - \beta)\omega}{1 + 4(q - \beta) \frac{\hbar\omega}{mc^2}} \quad (157)$$

Since $(\hbar\omega/mc^2) \approx 10^{-6}$, we can approximate Ω by the numerator in (157). Writing this in terms of the wavelength we find

$$\Lambda \approx \frac{\lambda}{2(q - \beta)} \approx \frac{\lambda}{2q} (1 + \beta/q) \quad (158)$$

since $\beta \approx 0.04$. We see that the wavelength of the emitted photon is shifted by $(1 + 1/kz_0)$ by the Gaussian mode, as expected.

E. CONCLUSIONS

In 1935 D. M. Volkov derived the Dirac wavefunctions for an electron in an electromagnetic plane wave. We made a correction to those wavefunctions by solving the Dirac equation in the external field of a laser with a realistic, finite Rayleigh length z_0 . We then used those wavefunctions to find the rate and angular distribution of photon emission in this field. We found that both the angular distribution and frequency of the emitted photons can be altered by changing the Rayleigh length, that is, focussing the laser.

Further research should add the finite length of the laser pulse to the calculation. This will give the emission lines a width in frequency corresponding, through the Fourier transform, to the pulse length.

LIST OF REFERENCES

1. Colson, W. B. et. al. in: *Laser Handbook*, Vol. 6, Chapter 1, eds W. B. Colson, C. Pellegrini, and A. Renieri, North-Holland, 1990.
2. Steenbergen, A. van in: *Laser Handbook*, Vol. 6, Chapter 12, eds W. B. Colson, C. Pellegrini, and A. Renieri, North-Holland, 1990.
3. Colson, W. B. in: *Laser Handbook*, Vol. 6, Chapter 5, eds W. B. Colson, C. Pellegrini, and A. Renieri, North-Holland, 1990.
4. Colson, W. B., Ph.D. Thesis, Stanford University, 1977.
5. Jackson, J. D., *Classical Electrodynamics*, 2nd ed., John Wiley & Sons, Inc., 1975.
6. Nayfeh, A. H. and Balachandran, B., *Applied Nonlinear Dynamics*, John Wiley & Sons, Inc., 1995.
7. Siegman, A. E., *LASERS*, University Science Books, Inc., 1986.
8. Smith, T. I. and Marziali, A., Stanford University, private communication, 1994.
9. Neil, G. et. al., "CEBAF UV/IR FEL subsystem testing and validation program," *NIM A* **358** , 159-162 (1995).
10. Colson, W. B. and Elleaume, P., "Electron Dynamics in Free Electron Laser Resonator Modes," *Applied Physics B* **29** , 101-109 (1982).
11. Esarey, E., Ride, S. K., and Sprangle, P., "Nonlinear Thomson scattering of intense laser pulses from beams and plasmas," *Phys. Rev. E* **48** n4, 3003-3021 (1993).
12. Brown, L. S. and Kibble, T. W. B., "Interaction of Intense Laser Beams with Electrons," *Phys. Rev.* **133** n3A, A705-A719 (1964).

13. Nikishov, A. I. and Ritus, V. I., "Quantum Processes in the Field of a Plane Electromagnetic Wave and in a Constant Field I," Sov. Phys. JETP **19** n2, 529-541 (1964).
14. Derlet, P. M., Perlman, H. S., and Troup, G. J., "Stimulated bremsstrahlung in a focused laser field," Phys. Lett. A **209** , 165-172 (1995).
15. Sakurai, J. J., *Advanced Quantum Mechanics*, Addison-Wesley Publishing Company, Inc., 1967.
16. Morse, P. M. and Feshbach, H., *Methods of Theoretical Physics*, chapter 9, McGraw-Hill Book Company, Inc., 1953.
17. Volkov, D. M., "Über eine Klasse von Lösungen der Diracschen Gleichung," Z. Physik **94**, 250-260 (1935).
18. Butkov, E., *Mathematical Physics*, Addison-Wesley Publishing Company, Inc., 1968.
19. Mandl, F. and Shaw, G., *Quantum Field Theory*, John Wiley & Sons, Inc., 1984.
20. Abramowitz, M. and Stegun, I. A., *Handbook of Mathematical Functions*, Dover Publications, Inc., 1972.

INITIAL DISTRIBUTION LIST

- | | |
|---------------------------------------------------------------------------------------------------------------------------|---|
| 1. Defense Technical Information Center
8725 John J. Kingman Road, Ste 0944
Fort Belvoir, VA 22060-6218 | 2 |
| 2. Dudley Knox Library
Naval Postgraduate School
411 Dyer Rd.
Monterey, CA 93943-5101 | 2 |
| 3. Professor William B. Colson, PH/Cw
Department of Physics
Naval Postgraduate School
Monterey, CA 93943-5000 | 3 |
| 4. Professor Robert L. Armstead, PH/Ar
Department of Physics
Naval Postgraduate School
Monterey, CA 93943-5000 | 1 |
| 5. Professor Karlheinz E. Woehler, PH/Wh
Department of Physics
Naval Postgraduate School
Monterey, CA 93943-5000 | 1 |
| 6. Professor James H. Luscombe, PH/Lj
Department of Physics
Naval Postgraduate School
Monterey, CA 93943-5000 | 1 |
| 7. Professor Anthony A. Atchley, PH/Ay
Department of Physics
Naval Postgraduate School
Monterey, CA 93943-5000 | 1 |

- | | |
|-----------------------------------------------------------------------------------------------------------------------------------------------------------------------------|---|
| 8. Professor Ron J. Pieper, EC/Pr
Department of Electrical Engineering
Naval Postgraduate School
Monterey, CA 93943-5000 | 1 |
| 9. Mr. John Albertine
Code 332, Division Director
Directed Energy Division
Space and Naval Warfare Systems Command
2541 Crystal Dr.
Arlington, VA 22245-5200 | 1 |
| 10. Dr. George Neil
Thomas Jefferson National Accelerator Facility
12000 Jefferson Ave.
Newport News, VA 23606 | 1 |
| 11. Masayo Bailey
PO Box 124
Lane, KS 66042 | 1 |